Universidad Autónoma de San Luis Potosí
Facultad de Ingeniería
Centro de Investigación y Estudios de Posgrado

Simulation of Powder Bed Fusion Processes

– o –

Simulación de Procesos de Fusión de Cama de Polvo

T E S I S

Que para obtener el grado de:

Doctorado en Ingeniería Mecánica con Orientación Terminal en Termofluidos

Presenta:
Alberto Torres Cruz

Asesor:
Dr. Dirk Frederik de Lange

San Luis Potosí, S. L. P. Septiembre de 2024

UASLP
Universidad Autónoma de San Luis Potosí

FACULTAD DE INGENIERÍA

15 de agosto de 2024

M.I. ALBERTO TORRES CRUZ
P R E S E N T E.

En atención a su solicitud de Temario, presentada por el **Dr. Dirk Frederik de Lange**, Asesor de la Tesis que desarrollará Usted, con el objeto de obtener el Grado de **Doctor en Ingeniería Mecánica con Orientación Terminal en Termofluidos**, me es grato comunicarle que en la sesión del H. Consejo Técnico Consultivo celebrada el día 15 de agosto del presente, fue aprobado el Temario propuesto:

TEMARIO:

"Simulación de Procesos de Fusión de Cama de Polvo"

1. Introducción
2. Estado del Arte de los Procesos de Fusión de Cama de Polvo
3. Desarrollo del Modelo de Curvas de Nivel de Densidad Múltiple Homogenizado
4. Modelado de Procesos de Fusión de Cama de Polvo utilizando el Modelo de Curvas de Nivel de Densidad Múltiple
5. Aplicación y validación del Modelo de Simulación
6. Conclusiones

Referencias

"MODOS ET CUNCTARUM RERUM MENSURAS AUDEBO"

A T E N T A M E N T E

DR. EMILIO JORGE GONZÁLEZ GALVÁN
DIRECTOR.

UNIVERSIDAD AUTÓNOMA
DE SAN LUIS POTOSÍ
FACULTAD DE INGENIERÍA
DIRECCIÓN

www.uaslp.mx

Copia. Archivo
*etn.

UNIVERSIDAD AUTÓNOMA DE SAN LUIS POTOSÍ
FACULTAD DE INGENIERÍA
Área de Investigación y Estudios de Posgrado

D E C L A R A C I Ó N

El presente trabajo que lleva por título:

Simulation of Powder Bed Fusion Processes

se realizó en el periodo septiembre de 2015 a septiembre de 2024 bajo la dirección del Dr. Dirk Frederik de Lange.

Originalidad

Por este medio aseguro que he realizado el trabajo reportado, y la escritura de este documento de tesis. para fines académicos sin ayuda indebida de terceros y sin utilizar otros medios más que los indicados.

Las referencias e información tomadas directa o indirectamente de otras fuentes se han definido en el texto como tales y se ha dado el debido crédito a las mismas.

El autor exime a la UASLP de las opiniones vertidas en este trabajo escrito y asume la responsabilidad total del mismo.

Este trabajo no ha sido sometido como tesis o trabajo terminal a ninguna otra institución nacional o internacional en forma parcial o total, exceptuando el caso cuando existe un convenio específico de doble titulación celebrado entre ambas instituciones.

Se autoriza a la UASLP para que divulgue este documento para fines académicos.

El autor del trabajo escrito, Alberto Torres Cruz.

Abstract

Additive Manufacturing (AM) is the process in which the object is created by building it one layer at a time and one of the main drawbacks when simulating AM lies in its definition, since many of the current techniques for simulation use a fixed domain to be simulated. Nowadays, there are many alternative methods for modeling moving interfaces; however, the ones that capture the interfaces with a phase function, such as Level Set (LS) methods, have a significant advantage over surface tracking approaches when it comes to controlling topological changes. The regular LS approach and the Conservative Level Set (CLS) method, on the other hand, are only able to differentiate between two distinct stable levels or phases by employing a single level set equation, which is a second order partial differential. Additional LS equations are required for the formulation in situations where there are three or more levels to be managed.

With the model that is provided in this work, which is a variation of the CLS approach, it is possible for a single level set variable to handle three stable levels. The level set variable can be understood to be the average relative density of a certain material that has three stable density levels. The proposed model uses a homogenized material model in which three levels can be distinguished: void, powder and fully dense material. Within this framework the three distinct materials coexist. This model is of particular interest since it can manage the deposition and densification of powder material in additive manufacturing techniques, specifically, Powder Bed Fusion (PBF) process. In comparison to the conventional LS formulation, the proposed model has a significant reduction in the number of degrees of freedom, which in turn reduces the amount of processing resources that are necessary.

In this thesis the proposed LS model is tested under several scenarios using the commercial Finite Element Method software Comsol Multiphysics®. Firstly, the model is developed and validated under common benchmarks such as Zalesak's disc to prove the correct behavior of evolving interfaces when handling two and three levels. Other interface tests consist in demonstrating its densification capacity. Secondly, a thermal model is also developed to work within this framework, which includes a Beer-Lambert heat source model that can deal with moving interfaces. Lastly, the model is tested with some PBF case scenarios found in literature. The proposed model demonstrated to be capable of reproducing experimental

morphology of the melt pool. The model proved to be also a good choice to predict the lack of fusion voids in PBF.

Resumen

La Manufactura Aditiva es el proceso en el que se crea el objeto construyéndolo capa por capa y uno de los principales inconvenientes al momento de simular Manufactura Aditiva reside en su definición, ya que muchas de las técnicas actuales de simulación utilizan un dominio fijo a simular. Hoy en día, existen muchos métodos alternativos para modelar interfaces en movimiento; sin embargo, los que capturan las interfaces con una función de fase, como los métodos de Curvas de Nivel, tienen una ventaja significativa sobre los enfoques de seguimiento de superficies al momento de controlar los cambios topológicos. El enfoque de Curvas de Nivel clásico y el método Curvas de Nivel Conservativo, por otro lado, solo son capaces de diferenciar entre dos niveles o fases estables distintos empleando una única ecuación de Curvas de Nivel, que es una ecuación diferencial de segundo orden. Se requieren ecuaciones de conjunto de niveles adicionales para la formulación en situaciones en las que hay tres o más niveles a gestionar.

Con el modelo que se proporciona en este trabajo, que es una variación del enfoque de Curvas de Nivel Conservativo, es posible que una única variable de conjunto de niveles maneje tres niveles estables. La variable de nivel puede ser entendida como la densidad relativa promedio de un cierto material que tiene tres niveles de densidad estables. El modelo propuesto utiliza un modelo de material homogeneizado en el que se pueden distinguir tres niveles: material vacío, polvo y material completamente denso. Dentro de este marco coexisten los tres materiales distintos. Este modelo es de particular interés ya que puede gestionar la deposición y densificación de material en polvo en técnicas de fabricación aditiva, específicamente, el proceso de fusión de cama de polvo. En comparación con la formulación de Curvas de Nivel convencional, el modelo propuesto tiene una reducción significativa en el número de grados de libertad, lo que a su vez reduce la cantidad de recursos de procesamiento que son necesarios.

En esta tesis, el modelo Curvas de Nivel propuesto se prueba en varios escenarios utilizando el software comercial de Método de Elementos Finitos Comsol Multiphysicis®. En primer lugar, el modelo se desarrolla y valida bajo puntos de referencia comunes como el disco de Zalesak para probar el comportamiento correcto de las interfaces evolutivas al manejar dos y tres niveles. Otras pruebas de interfaz consisten en demostrar su capacidad de densificación. En segundo lugar, también se desarrolla un modelo térmico para trabajar dentro de este marco, que incluye un modelo de fuente de calor Beer-Lambert que puede manejar interfaces móviles. Por último, el modelo se prueba con algunos escenarios

de casos de proceso de fusión de cama de polvo encontrados en la literatura. El modelo propuesto demostró ser capaz de reproducir la morfología experimental del baño fundido. El modelo demostró ser también una buena opción para predecir poros por falta de fusión en proceso de fusión de cama de polvo.

Acknowledgements

To my parents Graciela Porfiria Cruz Martínez, Pedro Torres Ramírez, and to my sisters Teresa Torres Cruz and Verónica Alejandra Torres Cruz for their unconditional support.

To Dr. Dirk Frederik de Lange for his unconditional help, support and guidance during my postgraduate studies.

To Dr. Wim Van Paepegem, for his help and support during my staying at UGent.

To my Friends for their patience and help.

To Consejo Nacional de Humanidades Ciencias y Tecnologías (CONAHCYT) for the scholarship granted for the development of the present work.

To the UASLP for the resources and facilities that allowed me to complete my research.

To UGent for the resources and facilities granted during my stay.

To the members of the evaluation committee of this research project, that helped me along this project with their valuable comments and vote of confidence.

Contents

List of Figures

List of Symbols and Abbreviations

The list below includes a list of the symbols and abbreviations used in the present work. Variables are in italic math font in the text. The author encourages the reader to read the full explanation in the text for better understanding.

Abbreviation (Meaning)

Additive Manufacturing (AM).
Conservative Level Set (CLS).
Electron Beam Melting (EBM).
Homogenized Multi-Density (HMD).
Level Set (LS).
Partial Differential Equations (PDEs).
Phase Field (PF).
Powder Bed Fusion (PBF).
Powder-Consolidated interface (PC).
Selective Laser Melting (SLM).
Void-Consolidated interface (VC).
Void-Powder interface (VP).
Void-Powder-Consolidated interface (VPC).

Symbol	Meaning	Units
Φ	Level Set Field	[-]
$\vec{x}$	Coordinate vector space	[m]
Γ	Generic interface	
t	Time	[s]
Ω	Generic domain	
$\vec{v}$	Velocity	$[\mathrm{m/s}]$
∇	Nabla operator	
$\vec{n}$	Unit Normal vector to the interface	[-]
τ	Pseudo time	[s]
ϕ	Conservative Level Set field	[-]
γ	Reinitialization speed	$[\mathrm{m/s}]$
ε	Conservative Level Set Diffusion Coefficient	[m]
ΔH	Latent heat of fusion function	$[\mathrm{J/kg}]$
h_s	Sensible specific enthalpy	$[\mathrm{J/kg}]$
k	Thermal conductivity	$[\mathrm{W/(m \cdot K)}]$
c_p	Heat capacity at constant pressure	$[\mathrm{J/(kg \cdot K}]$
ρ	Density	$[\mathrm{kg/m^3}]$
$\dot{\mathrm{Q}}$	Volumetric heat source	$[\mathrm{W/m^3}]$
P_{Cir}	Uniform circular heat source	$[\mathrm{W/m^2}]$
η	Power efficiency	[-]

P_{Gauss}	Gaussian circular heat source	$[\mathrm{W/m^2}]$
P	Power intensity	[W]
r_b	Heat source beam radius	[m]
f	Gaussian distribution factor	[-]
$P_{Elliptic}$	Gaussian elliptic heat source	$[\mathrm{W/m^2}]$
r	Radial coordinate	[m]
a	Gaussian elliptic/ellipsoid transversal factor	[m]
b	Gaussian elliptic/ellipsoid longitudinal factor	[m]
S	Optical penetration depth	[m]
I	Power intensity distribution	$[\mathrm{W/m^2}]$
x	x-coordinate	[m]
y	y-coordinate	[m]
z	z-coordinate	[m]
c	Gaussian elliptic/ellipsoid depth factor	[m]
P_{Gk1}	Single ellipsoid heat source distribution	$[\mathrm{W/m^3}]$
P_{Gk2}	Double ellipsoid heat source distribution	$[\mathrm{W/m^3}]$
M	Generic material property	[-]
k_{eff}	Effective conductivity between powder and bulk material	$[\mathrm{W/(m \cdot K)}]$
k_S	Thermal conductivity of the bulk material	$[\mathrm{W/(m \cdot K)}]$
k_P	Thermal conductivity of the powder material	$[\mathrm{W/(m \cdot K)}]$
ρ_{eff}	Effective density between powder and bulk material	$[\mathrm{kg/m^3}]$
ρ_S	Bulk material density	$[\mathrm{kg/m^3}]$
ρ_P	Powder density	$[\mathrm{kg/m^3}]$
$c_{p_{eff}}$	Effective specific heat capacity at constant pressure	$[\mathrm{J/(kg \cdot K)}]$
$c_{P,S}$	Bulk specific heat capacity at constant pressure	$[\mathrm{J/(kg \cdot K)}]$
$c_{P,S}$	Powder specific heat capacity at constant pressure	$[\mathrm{J/(kg \cdot K)}]$
h	Element size	[m]
f_{VC}	Anti-diffusive flux at the void-consolidated interface	[-]
ϕ_P	Level set value at powder	[-]
ϕ_V	Level set value at void	[-]
ϕ_C	Level set value at consolidated	[-]
δ	Generic transition interval	
H_s	Smooth Heaviside function	
f_{VPC}	Anti-diffusive flux at the void-powder or powder-consolidated interface	[-]
β	Switching function between f_{VC} and f_{VPC}	[-]
θ	Generic conservative quantity	
$\vec{J}$	Generic diffusive flux	
g	Generic volumetric source	
V	Generic volume	$[\mathrm{m^3}]$
$\vec{J}_{mass}$	Mass diffusive flux	$[\mathrm{kg/(m^2 \cdot s)}]$
$\dot{s}_{mass}$	Mass source per unit volume	$[\mathrm{kg/(m^3 \cdot s)}]$
ρ_C	Consolidated material density	$[\mathrm{kg/m^3}]$
u	Specific internal energy	[J/kg]

$\dot{s}_{ext,heat}$,	External input energy	$[\mathrm{W/m^3}]$
$\vec{J}_{heat}$	Diffusive heat flux	$[\mathrm{W/m^2}]$
h	Total or apparent specific enthalpy	[J/kg]
$\vec{q}_{cond}$	Heat conduction flux	$[\mathrm{W/m^2}]$
T	Temperature field	[K]
$\vec{q}_{mass}$	Heat flux due to mass diffusion	$[\mathrm{W/m^2}]$
L_m	Magnitude of latent heat of fusion	[J/kg]
C_p	Total or apparent specific heat at constant pressure	$[\mathrm{J/(kg \cdot K)}]$
h_{powder}	Powder specific enthalpy	[J/kg]
c_{layer}	Mass rate generation per unit volume	$[\mathrm{kg/(m^3 \cdot s)}]$
$\vec{q}_{in}$	Input external heat flux	$[\mathrm{W/m^3}]$
$\vec{q}_{out}$	Output external heat flux	$[\mathrm{W/m^3}]$
h_{conv}	Convection coefficient	$[\mathrm{W/(m^2 \cdot K)}]$
h_{rad}	Radiation coefficient	$[\mathrm{W/(m^2 \cdot K)}]$
T_∞	Far field temperature	[K]
T_m	Melting temperature	[K]
T_S	Solidus temperature	[K]
T_L	Liquidus temperature	[K]
g	Latent heat multiplier	[-]

1 Introduction

1.1 Simulation of Additive Manufacturing of Metals

New developments in technology generate an increase in the demand of individualized products highly adaptable to the needs of customers. For this, flexible manufacturing technologies are required, which have been evolving over the years. One of the processes with the greatest boom in the last three decades has been Additive Manufacturing (AM), which colloquially is also known as “3-D printing”, which, consists of a set of techniques that allow the creation of optionally complex shapes and structures that are manufactured without the need for tools or molds. These techniques, opposed to subtractive techniques in which material is removed, AM processes are based on material addition. The various technologies that comprise AM are changing the old paradigms about manufacturing, where large machinery is required for the production of various components. Today it is possible to create, with the use of these techniques, capricious geometries with a single machine that would even be impossible to manufacture with subtractive techniques. In addition to this, the benefit of designing the part without considering the limitations of traditional techniques has changed the old paradigms about product design. The new trend now focused on the production of complex and also functional forms taking lightweight to a new level, where the strength-to-weight ratio is continuously increasing.

Although the use of 3-D printed elements is expanding to various sectors, such as aeronautical [1], biomedical [2] and aerospace [3] [4], it has been found that it is extremely difficult to obtain mechanical properties like those obtained by conventional processes. Therefore, for practical applications, there are still serious limitations regarding the safety and mechanical performance of products made by additive techniques. For this reason, many investigations are being conducted in this regard, where an understanding of the factors involved in the process is sought to guarantee the quality of the products. These investigations can be categorized into two broad categories: Experimental and theoretical/computational. On one hand, experimental methods try to understand the process by trial and error methods for a specific component or process until a desired set of properties is reached. On the other hand, theoretical/computational research is focused on development of mathematical models that are solved analytically or numerically by computers. These models have the capacity to virtually reproduce in a computer some of the physical aspects of the process.

The utilization of modeling and simulation techniques have proven to be highly advantageous in various scientific and engineering disciplines. The appropriate utilization of computer simulations offers significant benefits, notably cost reduction. Numerical simulations are frequently more economically advantageous compared to physical tests, since they diminish the necessity of expensive equipment and supplies that are typically necessary in the trial-and-error procedure. Furthermore, simulations enable the study of phenomena that are inaccessible due to either their lack of direct observability or the challenges involved with experimental measurements. Simulations have the advantage of circumventing potential hazards and physical constraints typically connected with experimental approaches.

Although modeling of additive manufacturing has been studied for a long time, there are several issues that still need to be addressed. The main problem lies on the complexity of the intricated relation of the phenomena involved, that encompasses the fields of heat transfer, fluid mechanics, solid mechanics, and metallurgy. Previous successful models in welding have helped in the development of AM models, however the number of tracks in welding typically ranges from the order of 10 to 10^2, whereas the order of tracks to fully build a part in AM is several orders of magnitude bigger than that. That makes that the time required to solve the models increases considerably, preventing in many cases the use of such detailed models. Another important problem when modeling AM is the continuous evolution of the domain, which changes continuously as the part is built layer by layer during the whole process, starting from the mere substrate to the finished part. Although there are several techniques that can be implemented when modeling evolving domains, they have some issues that still need to be addressed. This encourages the industry and academy to develop efficient models capable to virtually reproduce and predict some of the main characteristic in additive manufacturing.

Computational time has been a significant factor that prevents the utilization of many models in the industry, as the intricate nature of numerous systems and processes can lead to very computationally expensive models [1] [2], [3]. This constraint restricts its applicability in numerous contexts. Hence, the capability of a model to replicate a system is insufficient by itself; rather, the model must also allow to be resolved within a reasonable amount of time. A simulation model that is efficient in terms of solution time enables researchers to effectively investigate a diverse array of scenarios within a reasonable amount of time.

The concept of computational efficiency is crucial in numerical simulations, since it directly impacts the speed of the solution, affecting the practicality and viability of its implementation. Computational

efficiency depends on multiple factors, that encompasses the intricacy of the problem [5] [6], the computational capabilities of the computer [7], the effectiveness of the methods employed, and the volume of data needed during the solution as well as in the postprocessing [2] [7] [8]. In recent times, advancements in processor capacity, memory capacity, and algorithm optimization have facilitated a decrease in computational time across a number of applications. Nevertheless, it is worth noting that there exists a wide range of models that need significant computational effort, particularly when dealing with multi-physics problems [1].

In this work the scope is limited to the Powder Bed Fusion (PBF) process, in which the product is built on a powder bed that is formed by adding layer by layer of powder, and in which each layer is fused selectively by an energy beam.

1.2 Research Objective

The objective of this research is:

to provide a time efficient model to better understand the thermal history in powder bed fusion processes.

Subtasks of this research are:

- Development of a model capable to describe evolving interfaces.
- Development of a thermal model that includes the relative density level set model to keep track of the temperature field in an additive manufacturing process.

1.3 Relevance

One of the complexities encountered in numerical simulation of additive manufacturing processes is the change of shape while building the part. Although there are several methods to solve free surface problems only a few can represent topological changes in a natural way. The primary contribution of this current work lies in the adaptation of one of the variants of the original LS method proposed by Olsson and Kreiss [9]. This adaptation is suitable when having three density phases, since the proposed model is more computationally efficient in the sense that it reduces the number of degrees of freedom requiring less memory. In addition to that, this model allows the analysis of thermal processes in changing domains, which allows the analysis of a variety of systems getting a better understanding of the physics. Therefore,

this model can be used to improve the quality of the products based on the underlying physics. It is even expected to be used for product optimization in an additive manufacturing process.

The research presented in this thesis has led to a publication that corresponds to the work developed in Chapter 3. The article titled '*Efficient single variable Level Set method for capturing moving interfaces in powder densification processes*', was published in the journal '*Computer Methods and Applied Mechanics and Engineering*' (doi: 10.1016/j.cma.2024.117086).

1.4 Thesis Outline

This thesis is divided into five chapters. After the current introduction in Chapter 1, a literature study about powder bed processes is presented in Chapter 2. An introduction about modeling powder bed fusion techniques is introduced is also introduced in Chapter 2. In Chapter 3 a novel method for capturing the evolution of three different levels/phases using one partial differential equation is developed. In Chapter 4 a heat transfer model is derived, which is compatible with the proposed model to capture the evolution of free surfaces. In Chapter 5 some case studies are presented to validate the model proposed in the development of the current thesis.

2 State of the Art of Powder Bed Fusion Processes

2.1 Powder Bed Processes

Powder Bed Fusion (PBF) is a term that encompasses Selective Laser Melting (SLM) and Electron Beam Melting (EBM). These techniques include the use of a layer of granular material as a base and utilizing lasers or electron beams to fuse the powder together.

The powder bed processes provide benefits such as the capability to manufacture intricate, tailored, and operational components. Nevertheless, these processes could have constraints regarding the rate at which they can manufacture products, the quality of the surface finish, and the specific needs for post-processing. The selection of an appropriate powder bed process depends upon several aspects, including the desired material, intended application, and available budget.

This study is centered around two specific additive manufacturing techniques: Selective Laser Melting (SLM) and Electron Beam Melting (EBM). The primary distinction between SLM and EBM lies in their respective heat sources. SLM employs a laser beam as its heat source, whereas EBM utilizes an electron beam. Another distinguishing feature is the environment of gas in which the process is executed. While Selective Laser Melting (SLM) is conducted in a standard atmospheric environment of air or argon, Electron Beam Melting (EBM) is carried out in vacuum. Although they have distinct characteristics, all techniques share a common requirement: the presence of a fine layer of powder that is selectively melted by a high-intensity energy beam. Once a layer has been fully scanned in the predetermined pattern, the mobile platform descends, and a roller is used to evenly distribute another layer of powder for melting. This procedure is iterated layer by layer until the final portion is fully formed. See Figure 1.

The following briefly explains the powder-bed printing process:

1. Using a leveling blade/roller, a fresh coating of powder of about 30 to 60 μm thick is applied to the constructing platform.
2. The area of powder that is part of the object's current cross section is melted by a heat source. A predetermined scanning path is followed by the high intensity beam.
3. To make room for a new layer, the constructing platform is lowered.

These steps 1-3 are repeated until the part is finished.

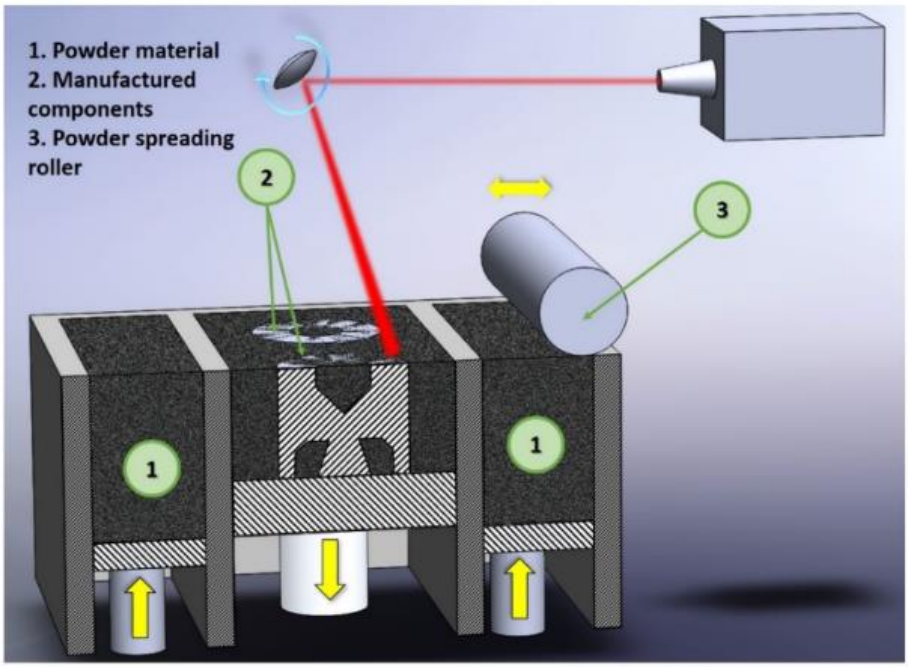

Figure 1. Powder bed fusion sketch [1].

Nowadays, the scientific and technological sectors are very interested in additive manufacturing because of its substantial influence across several industries and although both sectors have been making many components, there are many issues that still need to be addressed. For this reason, it is crucial to acknowledge that AM processes are inherently complex, especially when the main goal is that produced components satisfy high mechanical quality requirements. Several studies on the matter have found over 130 factors that have an impact on both the manufacturing process and the final quality of the manufactured component [1], [10] . Some of the main defects are:

- Porosity and lack of fusion.
- Surface quality.
- Delamination and cracking.
- High internal stress levels and large distortions.

A brief explanation about these defects is given in the following paragraphs.

2.1.1 Porosity and Lack of Fusion

Porosity and lack of fusion are common defects in AM that have a detrimental impact on mechanical properties. Although porosity can happen because of lack of fusion (leading to the incomplete

densification of the powder density), porosity can also appear because of a high-power density. On one hand, when working at high-power density, the melt pool develops into a keyhole mode (see Figure 2) that can lead to instabilities in the flow, resulting in the formation of voids inside the solidified region. The keyhole phenomena is an essential aspect of the high-energy processing mode, which results in the production of an open cavity formed within the molten pool by the vapor pressure. The formation of this cavity, known as the "keyhole", is the result of the strong localized heating, which causes the material to vaporize at a rapid rate.

In both SLM and EBM, the keyhole effect has the potential to have a major impact on the quality of the parts that are created. In case of a stable keyhole, the keyhole mode can be advantageous due to the higher penetration depth that can be reached at high velocities, which guarantees an adequate adherence by fusion with the previous layer. However, unstable keyhole behavior can have a negative impact on the mechanical qualities of the finished product as a result of defects such as the introduction of porosities in the fusion tracks. The keyhole dynamics are affected by a variety of elements, including the laser power, the scanning speed, and the characteristics of the material [11]. The magnitude of keyhole porosity may differ based on the flow parameters and dimensions of the keyhole [10]. While increasing the laser intensity can decrease the size of the pores, it is unable to totally eradicate them. Kasperovich and Hausmann [2] found that even with optimum selective laser melting (SLM) configurations, there is still a porosity level of roughly 0.08%. Additionally, the presence of gas pores might also arise from the shielding gas or alloy vapors within the molten pool. On the other hand, if the flow is produced with a low power density, insufficiency in the penetration of the molten pool from a higher layer into either the substrate or the previously deposited layer can result in absence of fusion producing a low-quality bonding. According to Hojjatzadeh et al., [12], there are six pore formation mechanisms:

1. Pore transfer for feedstock powder.
2. Keyhole.
3. Surface fluctuation due to droplet impact.
4. Shallow cavity collapse.
5. Pore induced by cracks.
6. Vaporization of volatile substances around the melting boundary.

According to Vaglio et al. [10], the keyhole is the most frequent and then the most relevant in porosity, and the most important in material properties. Some experimental results where the porosity by the

keyhole effect can be appreciated in the work of Soylemez [13], some of these results are shown in Figure 2.

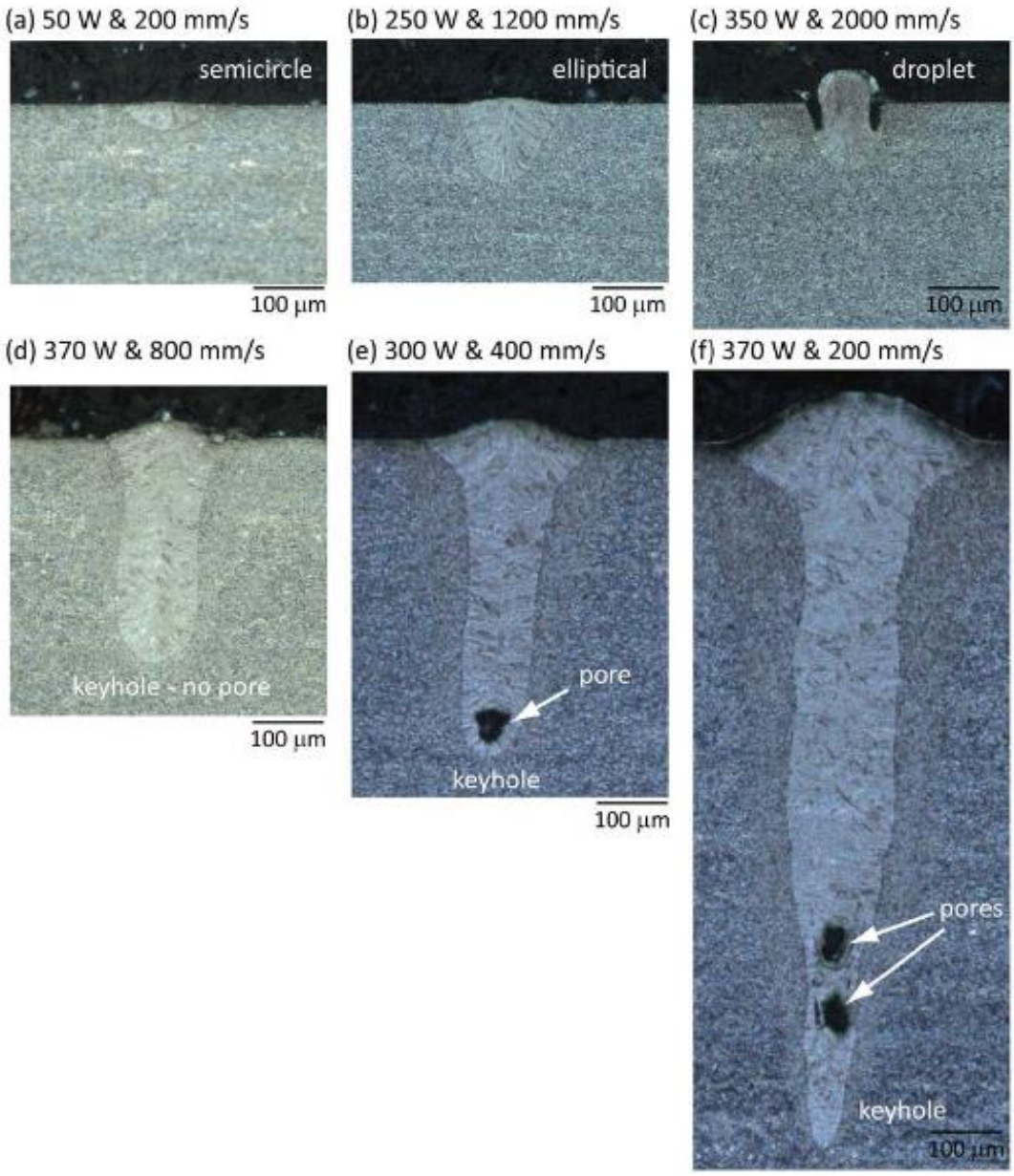

Figure 2. SLM cross-section specimens in which the energy density varies, (a) circular profile (Conduction mode) , (b) elliptical profile (Conduction mode), (c) droplet, (d) keyhole, no pore (keyhole mode), (e) keyhole with pore (keyhole mode), and , (f) keyhole with pores (keyhole mode) [13].

2.1.2 Surface Quality

The surface roughness in components manufactured via additive manufacturing is influenced by several interconnected input factors, which in turn lead to multiple visible or measurable output conditions that

might eventually impact the performance of the workpiece. The input parameters are the material feedstock, component design, process selection, process parameters, and post processing [3].

An optimal surface smoothness can be achieved by maintaining a reasonable quantity of heat input. Increasing the temperature under high energy conditions enhances the wettability of the melt. Nevertheless, augmenting the laser power increases the probability of the molten substance interacting with the remaining oxygen leading to oxidation that can change the surface tension gradient in the molten pool. At those size levels surface tension gradient plays an important role over melt pool fluid dynamics that can develop into instabilities producing discontinuous tracks or non-uniform tracks. Due to surface tension, the liquid material solidifies in a spherical-like shape, known as balling effect. Excessive balling decreases the effectiveness and quality of the powder layer deposition. In Figure 3 shows the balling defect that develops into two defects variants: (a) discontinuous track, and (b) non-uniform track. Furthermore, the uneven surface may produce voids and particulates, leading to the creation of pores [5]. These combined effects contribute to the production of components with a wide range of surface defects. Surface quality can be attributed to three main factors: the formation of spherical shapes due to high surface tension, insufficient wetting of molten metal, and the attachment of partially melted particles to component surfaces during solidification.

The balling phenomena in PBF processes has three adverse effects [6] [7]:

1. Surface irregularity.
2. Development of holes between the balls.
3. The obstruction caused by the collision of solid spheres with the blade used for depositing powder.

Consequently, balling leads to an uneven deposition of layers, inadequate connectivity between layers following fusion, and ultimately, low and inconsistent component density and quality. Internal porosity in produced components is a significant defect in PBF since it impacts fatigue performance and facilitates fracture formation and propagation in the workpiece.

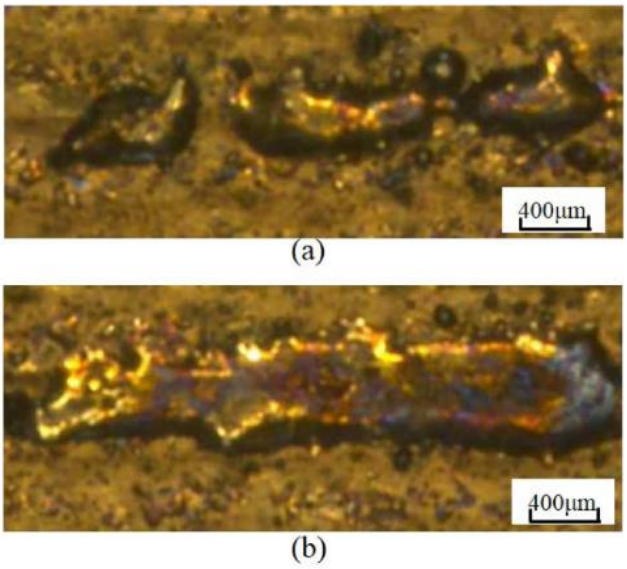

Figure 3. Balling effect in a (a) discontinuous track, and (b) non uniform track [8].

2.1.3 Microstructure

The microstructures generated by additive manufacturing (AM) are intricate and frequently exhibit spatial variations within a part. The intricate thermal histories linked to additive manufacturing (AM) techniques considerably impact the microstructure. This is because each individual point within a component created by AM may have a distinct thermal history, which might vary greatly from the surroundings, such as those at the edges. Moreover, the wide range of additive manufacturing procedures leads to significant differences in thermal histories, which in turn result in distinct microstructures [7]. The changes in the microstructure of alloys that take place throughout the solidification and cooling process have a crucial impact on the final mechanical properties of metal components in powder bed techniques. The rapid nonequilibrium solidification and significant temperature gradients induced by during the process lead to a heterogeneous microstructure.

The coarsest level of microstructure is typically the grain size and morphology, having temperature history and thermal gradients a great importance in the development of such structures. The grain morphology and crystallographic orientation of a component are determined by the process of melting and subsequent solidification of the molten pool. The geometric characteristics of the melt pool play a crucial role in determining the shape of the grains that are formed in the fusion zone and the rate at which solidification occurs in that area. Although keyhole mode is commonly preferred in welding, since it involves the beam

deeply penetrating the metal substrate while minimizing heat input to the workpiece, the conduction mode or the transition mode is preferred in powder bed processes. This is because of the high potential of producing unstable melt flow by the presence of a keyhole generating undesired porosity in the parts. The formation of the grain structure during solidification has a significant impact on its resistance to solidification cracking and mechanical characteristics.

At a finer level, the microstructural phases undergo significant undercooling in the material, not only influencing the formation of texture and grain structure but also affecting the microstructural phases, their sizes, distributions, and chemical compositions.

The fluctuations in temperature, both in space and time produce solid state phase transformations, dissolution and reprecipitation of phases [7], which is a finer level of microstructure also affected by heat. These transformations are also produced because of the rapid heating and cooling, in which there is a proclivity to exhibit metastable phases. Nevertheless, the metastable phases that are created in a single layer may undergo partial or total decomposition into stable phases as a result of the thermal cycling effect caused by the melting and fusion of the succeeding layer or the preheating of the powder.

Vaporization of alloying elements of many crucial engineering alloys during additive manufacturing can take place because of the high temperatures of the molten pool. Due to the varying volatility of elements in all different alloys, selective vaporization can take place, leading to changes in the overall composition of the alloy [3], [14]. Variations in composition can have an impact on the formation of solid structures, resistance to corrosion, and mechanical qualities, which can provide a significant challenge in the production of a variety of components. The factors that have the greatest impact on the vaporization of alloying materials in additive manufacturing are the ones that control the shape of the molten pool and the distribution of temperature such as: power, scanning speed, and beam diameter [14]. While it is possible to certify the chemical composition of the input material, the powder bed processes promote a substantial modification of the composition. This modification can involve the addition of interstitial components that are present in the atmosphere as well as the loss of constituent elements through vaporization. When processing is done in the presence of air, it is common to find larger concentrations of interstitial elements (such as oxygen, nitrogen, and hydrogen) compared to the original composition of the material being processed. The presence of these interstitial components can greatly influence the final mechanical characteristics and microstructures. For instance, in titanium-based alloys with a significant capacity to

dissolve oxygen, the absorption of oxygen during the additive manufacturing (AM) process, can result in both enhanced yield strength and reduced ductility [15].

2.1.4 Stresses, Cracks and Deformations

According to Lindgren [16], during the additive manufacturing process, the solidifying melt pool tends to contract because of liquid to solid transformation and thermal contraction. Nevertheless, the temperatures of the previously formed layers are lower than the temperatures of the layer being deposited. Consequently, the depositing layer experiences more contraction compared to the lower layer, which in effect restricts the contraction of the solidifying layer, leading to tensile tension in the newly solidified layer. As a result, cracking may occur at the grain boundaries if the tensile stress level surpasses the strength of the solidifying metal.

Another cracking type is the cracking that occurs inside the mushy zone. During the cooling process, the mushy zone experiences a tensile tension caused by the solidification shrinkage and thermal contraction of the deposited material. In order to compensate the solidification shrinkage, the nearly solidified zones will result in the suction of the remaining liquid in the hotter mushy zones, which can lead to a depletion of the liquid phase between the solidified grains, leaving in fact the grains disconnected, effectively presenting as a crack. Due to the phenomena, this cracking is referred to as “hot cracking” or “liquid cracking”. Alloys that have a significant difference between their liquidus and solidus temperatures, such as nickel base superalloys, alloys with a large molten pool like Ti-6Al-4V, and aluminum alloys with a high coefficient of thermal expansion, are the most prone to liquation cracking. In additive manufacturing (AM) components, cracking can occur in two ways: it can extend over several layers, as shown in Figure 4(a), or it can be limited to a length equal to the thickness of a single layer, as shown in Figure 4(b).

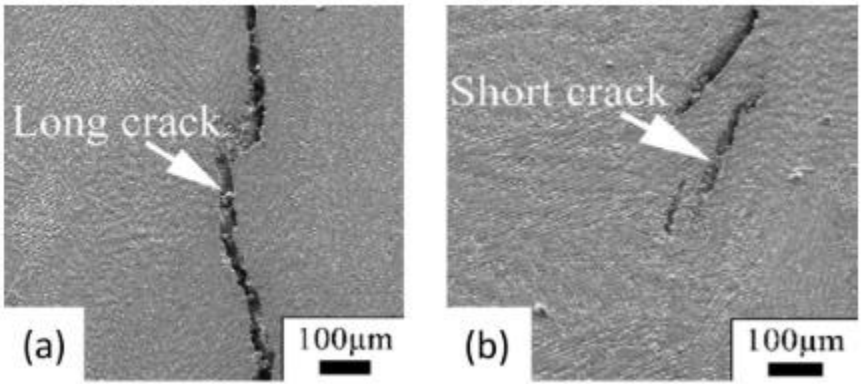

Figure 4. Cracking, (a) long crack, and (b) short crack, from Zhao et al. [17].

Residual stresses are well recognized as a significant factor in the development of fractures and distortion of the component. These stresses can cause the detachment of built-up layers from the underlying material and result in cracks in the final product, and it is very important to say that many of the aforementioned defects that cannot be neither partially nor completely removed. The high residual stresses and deformations might result in fatal repercussions, leading to a loss of geometrical precision and structural damage. Consequently, items produced using SLM and EBM techniques may necessitate the use of supporting structures to prevent bending or distortion during the production processes. The remaining stress can be eliminated or reduced by an appropriate heat treatment procedure.

2.2 Modeling of Powder Bed Fusion Processes

PBF encompasses intricate processes that involve mechanisms such as heat absorption, significant temperature gradients, localized melting and solidification of particles, phase change, and complex fluid flow. In addition, physical effects in PBF also affect components on various length scales and timescales, including residual stresses, beam spot size, laser beam penetration depths, among others. Timescales can vary greatly depending on the specific processes involved. They can range from longer periods of time, such as hours, for global heat treatment during manufacturing, to shorter durations like minutes for single-layer building, and even smaller timescales such as milliseconds for the brief interaction between the beam and the material [18]. Recognizing these small scales is crucial for understanding process behavior and component quality. Modeling approaches and numerical simulations on multiple scales and timescales are ideal tools for gaining insights about the underlying physics. This knowledge can be used to predict system's behavior that can be pushed even forward to use it as a tool for product optimization purposes

Based on the overview provided above about many issues impacting the PBF processes, it is evident that there is a need to optimize the process in order to minimize the defects in the manufactured parts. To reduce the expenses associated with experimental trial and error approaches, it can be beneficial to construct accurate numerical models of PBF processes. One strategy is to utilize data-driven models based on statistical principles [19] or artificial intelligence algorithms to describe the process. These models are highly beneficial for controlling processes with limited knowledge, but they do not provide a comprehensive understanding of the interactions between diverse phenomena occurring in the process [6]. In addition, these methods require considerable data that usually are obtained from experimental work or

tests. In addition, these models and methods con only predict the process under previously tested conditions and the predictive quality outside the tested parameter window is highly uncertain. Therefore, this literature review focuses on models that are derived based on fundamental concepts. In physics-based models, the fundamental equations of the problem, which involve the conservation of mass, momentum, and energy, are simplified and combined with the constitutive equation of the material. These mathematical models are typically expressed as Partial Differential Equations (PDEs).

2.2.1 The complexity of modeling PBF

Striving for efficient manufacturing, modeling and simulation play a vital role in gaining a comprehensive understanding PBF processes and optimizing them for maximum effectiveness. However, there are several significant challenges when it comes to modeling PBF. So far, due to the large time and space scales is not possible to create full physics models that encompasses every detail during the process [1], [6], [19], [20], [21], [22], [23], [24]. That is why a multi-scale approach is preferred. The typical scales are shown in Figure 5, where 4 scales are considered. Micro-scale explores metallurgical aspects such as the evolution of grains, texture, segregation, solid-state phase transformations. Particle-scale explore powder distribution, particle packing density, interaction of powder with the heat source. Mesoscale mainly analyses the heat transfer in the dynamics of the fluid flow from melting to solidification, limiting to the near vicinity of the melt pool. Macroscale aims to predict the thermal-mechanical interactions including thermal stresses, distortion and residual stresses. Depending on the characteristics to be analyzed a numerical technique needs to be chosen. The scale that is aimed in the current thesis belongs to something in between the meso-scale and macro-scale focusing on thermal aspects. At this scale, the material addition needs to be simulated and modeled with a high level of accuracy. Simultaneously, the model exhibits unavoidable non-linearities due to various parameters being influenced by temperature. These parameters might include material properties, radiation losses and heat input.

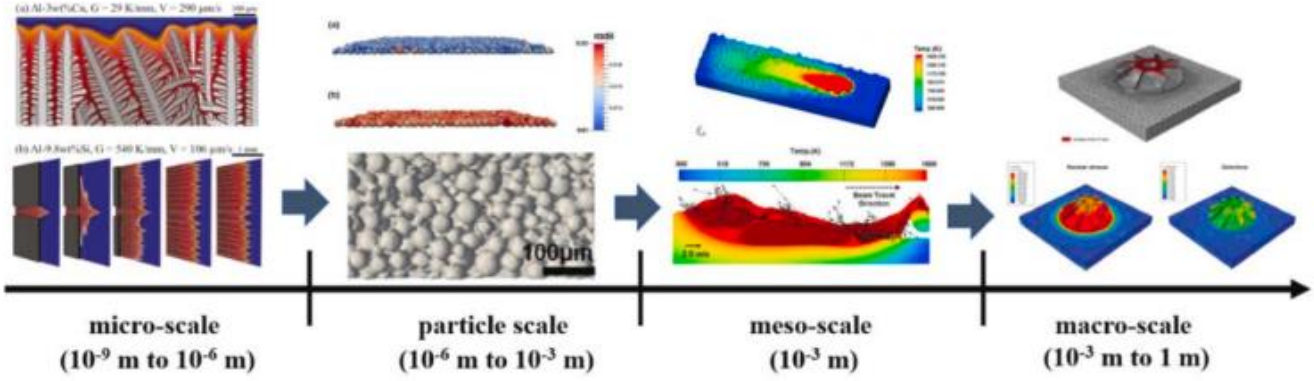

Figure 5. Multi-scales in modeling additive manufacturing [4].

Therefore, the difficulties associated with a thermal macro-scale model of Selective Laser Melting (SLM) and Electron Beam Melting (EBM) can be outlined as follows:

- The difficulty of modeling the addition of material and the subsequent shape change of the material domain.
- The conversion from beam energy into thermal energy is through a complex non-linear mechanism
- The fusion and solidification phase transitions has a strong non-linear effect on the heat transfer equations.
- The melt pool requires the integration of the coupled heat transport and fluid dynamics into a multi physics thermo-fluid simulation
- Precise temperature dependent data on the material properties are usually lacking and hard to obtain over the full temperature range from ambient conditions up to the melting point and well beyond, and even more so, considering non-equilibrium conditions.

2.2.2 Computing Capacity and Temporal Aspects

Even when different theoretical models and numerical approaches have been designed for specific scales in space and time, the simulations might take a considerable amount of time. This is because the non-linearities and complex phenomena still remain [25], [26], [27], [28]. That is why simulation time is still one of the most important barriers that prevents a full adoption of these predictive models. As a result, new modeling techniques have been developed in order to create models that give solutions in an acceptable amount of time. To do that is imperative to look at the computational methods. Broadly speaking, two discretization types can be regarded: spatial discretization and temporal discretization. The spatial discretization is reduced to a set of equations that could be coupled (implicit) or uncoupled

(explicit). The temporal discretization leads to a set of timesteps in which the set of equations, obtained from the spatial discretization, are solved. Hence, to reduce the computational time, either the number of equations that are solved at every time step are reduced or the time step size is increased, both would be the ideal. Increasing the timestep is strongly related to the time discretization which can be either explicit or implicit. Although explicit methods are faster to solve for each time step, they have a stability criterion that limits the time step size, which can result in an excessive number of time steps required to simulate over a specific time interval. On the other hand, the implicit methods are unconditionally stable, but they have a much higher computational cost for each time step. The other option for reducing computational time regards the space discretization. Here, the strategy consists in using less elements by using efficient meshes. This involves using elements only where needed. For moving heat sources or evolving surfaces that mesh also needs to evolve either by moving the original mesh [29], [30], remeshing [31] or activating and deactivating elements. These methods have the advantage of using fewer elements in every timestep; however, they might need extra equations or extra manual processing. Another approach is the reduced order modeling that goes beyond in the reduction of equations by reducing the space domain [32], [33].

Another important aspect is the computational hardware capacity, which is mainly related to the processor and volatile memory. Although technology is ever increasing there is still no available computer to solve one complete case that encompasses all the time-space scales as well as all the physics involved [32]. However, great advances in numerical methods are allowing distributed computing which consist in incrementing the computational capacity by distributing tasks between different computers while keeping communication among them. This is usually made by algebraic or domain decomposition or by coupling multi-scale models [34], [35].

2.2.3 Reduced Order Modelling

Order reduction modeling and simulation, commonly referred to as "order reduction" or "model reduction," is a valuable technique employed in various disciplines including engineering, data science, and scientific research. Its purpose is to somehow reduce complexity in mathematical models while still ensuring accurate simulation outcomes. This technique is particularly useful when dealing with systems that have a high computational cost or require detailed and extensive mathematical models, such is the case of PBF.

Here are some important aspects to consider when it comes to order reduction modeling and simulation [32]:

- Simplifying the model: Simplify mathematical models or complex systems while preserving the required accuracy for analysis or simulation. This is achieved by removing unnecessary details from the original model.
- Reduced Dimensionality: One of the primary uses of order reduction involves decreasing the dimensionality of systems of equations or mathematical models. This can lead to a substantial decrease in the time needed to perform calculations as well as the required number of computational resources.
- Validation and Calibration: Ensuring the accuracy and appropriateness of order reduction models is crucial for their successful implementation in specific applications. This may involve making comparisons with the original model and making adjustments to the parameters of the reduced model.

Order reduction is a valuable technique for reducing computational resources and dimensionality in complex mathematical models, enabling faster simulations and analyses. It requires a balance between precision and efficiency, to avoid a significant accuracy loss. Order reduction is crucial in real-time systems simulation, process optimization, and decision making, as it helps make decisions based on models.

2.2.4 Multiscale Modeling Coupling

One interesting technique in this physics-based models is coupling multi-scale models [18], [34], [36]. Coupled multiscale modeling is a computational modeling technique that involves the real-time interaction of models at multiple spatial or temporal scales to accurately represent intricate systems. The goal of multiscale modeling is to encompass a wide range of phenomena that prevail at different levels in a system [32].

Here are some important aspects to consider when it comes to multiscale modeling:

- Scales: Multiscale modeling encompasses the development of models at various length scales, ranging from microscopic to macroscopic, depending on the specific system or process under investigation.

- Interaction between Scales: In a multiscale model, there is a dynamic interplay between the different scales. Take note that properties or behaviors at the microscopic level can have a significant impact on behavior at the macroscopic level, and the reverse is also true.

Multiscale modeling is a valuable tool for studying PBF, in order to incorporate effects such as materials properties, material interaction, physical phenomena, heat transfer, among others. It helps tackle the inherent complexity of these systems making it more tractable without the need of oversimplification. However, it often requires significant computational power and a large amount of data, and the integration and calibration process can be complex.

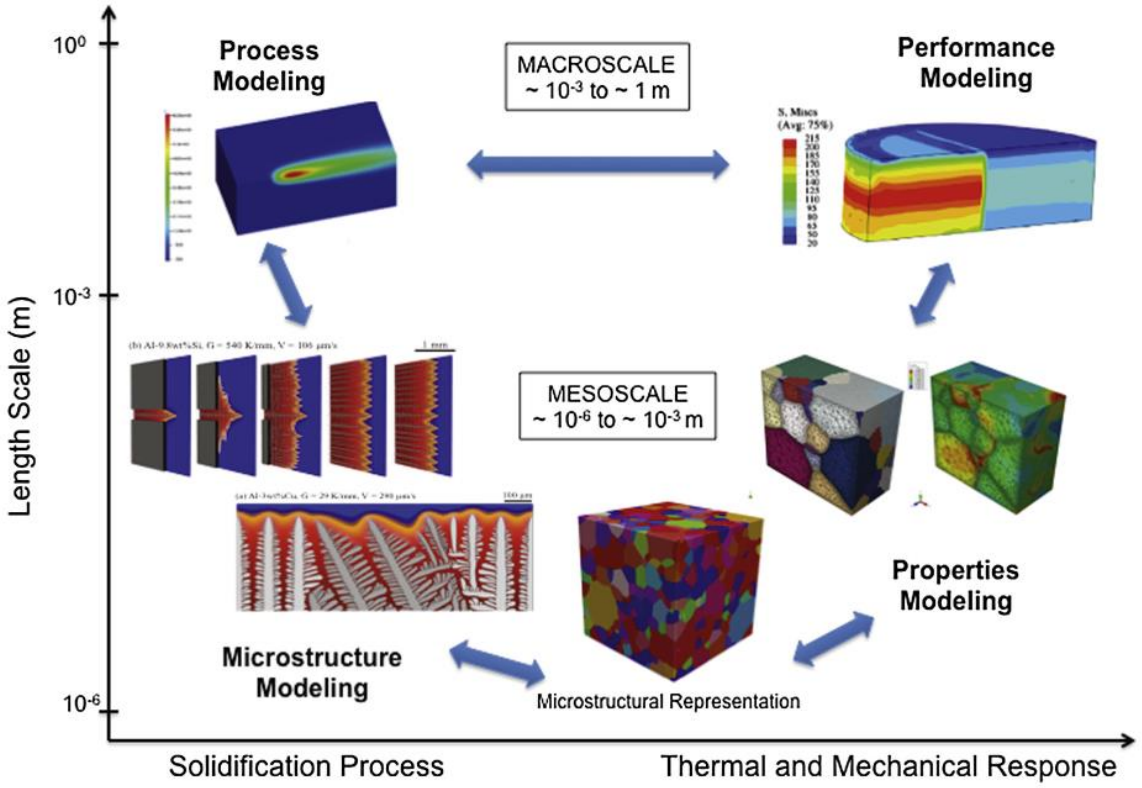

Figure 6. Integrated process-structure-properties-performance modeling and simulation approach and associated length scales [37].

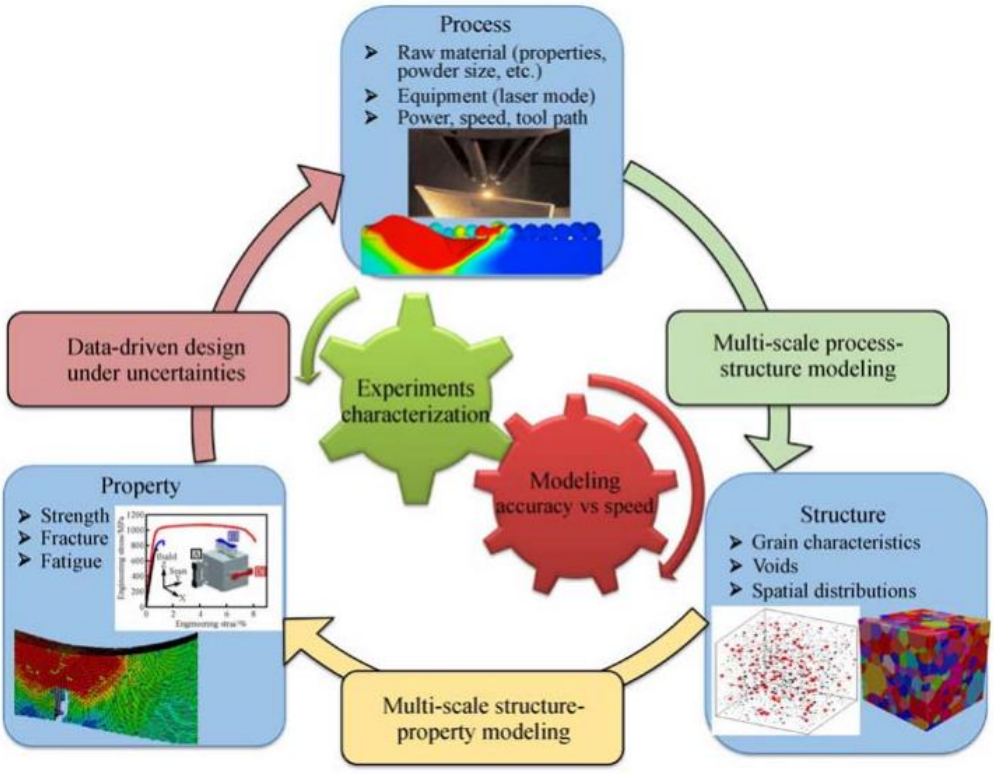

Figure 7. Data driven multi-scale and multi-physics [36].

2.3 Modeling of Evolving Interfaces

Many physical phenomena in fluid dynamics are affected by the presence of moving interfaces. One of the main challenges involves accurately identifying this interface which is not known a priori and needs to be calculated as part of the solution. When dealing with moving interface problems, it is important to consider the interplay between momentum, heat, and mass transport, as well as the impact of interface formation, evolution, and dynamics. These factors play a crucial role in shaping the behavior of the system. Furthermore, the intricate nature of these phenomena while keeping the track of the interface, adds another layer of complexity to the problem.

Nowadays, many methodologies to monitor interfaces of different shapes are available, each with its own merits. There are two main types of techniques that can be used: volume tracking (Eulerian methods) and surface tracking (Lagrangian methods) [38]. On one hand the Lagrangian methods involve a grid attached to the interface's geometry, resulting in its continuous adaptation to it. On the other hand, the Eulerian methods employ a formulation with a fixed grid. Instead of explicitly tracking the interface between the

phases, the interface is captured in an approximate manner as the actual interface is located within the sub-discretization spaces (volumes) between the fixed grid locations, which means that the actual discrete interface converts into a smoothened transition. With these fundamental distinctions in methodology between the two classes of approaches, we can now make subsequent comparisons.

Another important difference between the two methods lies in the application of boundary conditions. While the boundary conditions can be accurately applied over the interface in the Lagrangian methods, the boundary conditions need to be adjusted and reformulated in the Eulerian methods to integrate them into the governing transport equations. Each method has its advantages, for example, when using Lagrangian methods, it is necessary to account for motion terms and adjust the grid as it adapts to the interface. Whenever the interface starts to deform, the grid needs to be regenerated, which might require solving an extra partial differential equation. Eulerian methods have an advantage in this regard because they use a fixed grid, eliminating the need for regenerating the grid. However, achieving improved resolution in specific regions can be quite challenging because they use a diffuse approximation of the interface and, at the same time an extra partial differential equation is needed to track the interface position, for instance, using a phase function. This issue in the Eulerian approach becomes an advantage over the Lagrangian methods, because so far Lagrangian methods have struggled with handling topological changes due to the breakdown of the structured grid arrangement and the need for unstructured grid methods to redistribute field information near the interface. On the other hand, Eulerian methods handle merging and fragmentation in a natural way [39].

2.3.1 Level Set Methods

Among the various techniques for modeling interfaces, Level Set (LS) methods stand out for its ability to accurately represent topological changes. This approach is a suitable option for modeling PBF processes, which is the primary focus of this project. The Level Set method relies on representing interfaces in an implicit manner that defines the interface as the iso-contour of a certain function, which we can refer to as Φ, and typically the zero contour is defined as the interface ($\Phi(\vec{x}) = 0$). The traditional Level Set (LS) method proposed by Osher and Sethian [40], was originally developed to track the motion of an interface front. In this method the interface, $\Gamma(t)$, is defined as: $\Gamma(t) = \{\vec{x} \mid \Phi(\vec{x}, t) = 0\}$. Usually, the values inside the domain of interest, Ω, get $\Phi > 0$, and the values outside get a $\Phi < 0$. A common function to set the initial condition is the signed distance function to the interface.

In this method, the interface movement is determined by the convection equation, and it is solved for the Level Set function, Φ. Here, $\vec{v}$ is the velocity field:

$$\frac{\partial \Phi}{\partial t} + \vec{v} \cdot \nabla \Phi = 0 \tag{1}$$

This velocity field can be governed by curvature, normal or any advection velocity. The normal vector $\vec{n}$ is defined as:

$$\vec{n} = \frac{\nabla \Phi}{\|\nabla \Phi\|} \tag{2}$$

One of the benefits of this model is that $\|\nabla \Phi\| \approx 1$. However, as the front evolves, the level set function may no longer be the signed distance function and its gradient's length will no longer be unity. This is due to the advection, which tends to create irregularities in the solution. Thus, a reinitialization step is typically implemented. This step involves a stage where calculation is stopped, and the level set is restored as the distance function with respect to the new interface location. A widely used approach is the method suggested by Sussman et al. [41], which applies a reinitialization step that uses the unit gradient as a condition to restore the signed distance function, see equation (3).

$$\frac{\partial \Phi}{\partial \tau} = \text{sgn}(\Phi)(1 - \|\nabla \Phi\|) \tag{3}$$

The reinitialization process includes a pseudo-time, τ, which is employed to solve the Φ-field until the unity gradient is recovered. While this method has shown success in previous studies [39], [41], it does have a drawback in terms of conservation. The advection step in (1) and the reinitialization step in (3) are not conservative. In order to address this issue, Olsson and Kreiss [9], [42] devised a conservative LS known as Conservative Level Set (CLS) method that, instead of solving for the signed distance function to the interface, solves for a smeared phase function $\phi(\vec{x}, t)$ that ranges from zero to one. For this definition, the interface is located at $\phi = 0.5$. So, the CLS model can be set as:

$$\frac{\partial \phi}{\partial t} + \nabla \cdot (\vec{v}\phi) = 0 \tag{4}$$

Like the traditional LS, the phase function variable, ϕ, will not retain its original shape due to the advection field, $\vec{v}$. Therefore, a re-initialization step is also necessary but in CLS method a conservative reinitialization step is employed instead:

$$\frac{\partial \phi}{\partial \tau} = \gamma \nabla \cdot (\varepsilon \nabla \phi - 4\phi(1-\phi)\vec{n}) \tag{5}$$

The equation (5) on the right-hand side combines a diffusive flux term, $\varepsilon \nabla \phi$, with an anti-diffusive flux term, $4\phi(1-\phi)\vec{n}$ (this term is also referred as a compressive flux term). Basically, this method adds extra diffusion to correctly manage the convective term avoiding irregularities during the solution step. However, this isotropic diffusion would smear off the transition zone in an excessive way. Here is where the anti-diffusive term comes into play by adding an opposite flux in the transition zone that keeps a balance between diffusion and anti-diffusion maintaining the size of the transition zone. It is worth mentioning that a factor 4 is included for ease of comparison, so that ε is approximately the size of the transition interface thickness. The coefficient γ governs the speed at which the interface is restored through computation. The calculation of the normal $\vec{n}$ can be obtained similarly as in the original formulation by equation (2), but in this case the phase function is used instead. However, despite the advantages of the CLS formulation (4) to (5) over its predecessor (1) and (3), there are some issues that still need to be considered. One of its main drawbacks is the imprecise calculation of the normal. In the CLS framework, the length of the ϕ-gradient is no longer unity. Instead, its value varies across the interface and, most importantly, its value decreases to zero outside of the interface zone. Precise calculations of the normal are crucial, as inaccuracies in these calculations can result in fluxes that may disrupt the interface and create instabilities.

It is known that the normal computation in regions where the phase function approaches zero or one the gradient length becomes extremely small. In such cases, the normal can lead to spurious behavior. Several authors have tried to enhance the quality of the normal with good results. Shukla et al., [43] presented a model that enhances the normal by the addition of an auxiliary function which is based on the phase function. This auxiliary function is designed to have the same normal but is smoother than the original. Shervani and Vasilyev [44] proposed a novel approach to enhance the normal quality. They introduced a new definition that includes an additional exponential term to prevent division by zero, resulting in good results. Additional advancements incorporate the advantages of LS and CLS, as demonstrated in the research conducted by Desjardins [45], Zhao et al., [46], and Chiodi and Desjardins [47]. In this study,

the authors successfully determine a conserved variable by solving for the phase function, but normal is calculated using a reconstruction of the signed distance function. In the study of Nave et al., [48] a modified version of the level set approach that incorporates gradient information is introduced. They also utilized cubic Hermite interpolation elements, which offer a straightforward and precise estimation of the normal and curvature.

All the aforementioned works implemented the advection equation along with the re-initialization step in two steps. This two-step solution is convenient for explicit methods, in particular when an efficient narrow band method is applied in which the re-initialization is applied only near the interface. Alternatively, several authors combined both equations into one single convection-diffusion equation, e.g. Ville et al., [49], Guermond et al., [50], Quezada de Luna et al., [51].

Although this literature study is mainly focused on the LS methods, a special mention is made about the Phase Field methods. These methods resemble a lot the LS methods in the sense that both use a phase function or phase field to identify each phase. One of the differences relies on the fact that the Phase Field equation is a 4^{th} order partial differential equation, whereas the LS equation is a 2^{nd} order partial differential equation. An interesting comparison, between Phase Field and Level Set, was made in Sun and Beckermann [52]. In that work the similarities among Phase Field and the Conservative Level Set from Olsson and Kreiss [42] are analyzed. It is important to notice that these Phase Field methods are commonly solved without a re-initialization step. In the works of Chiu and Lin [53], Akhlaghi and Hamouda [54], Hua et al., [55], Wacławczyk [56], and Darabi et al., [35] some implementation of Phase Field applied to PBF can be found.

2.3.2 Multi Level Set

As it was mentioned before, standard Level Set methods can only manage one interface type, it is to say, only two stable levels or phases can be handled with one Level Set equation. When working with more than two phases, additional LS equations are needed. Some early studies about this topic were performed by Merriman et al., [57]. In this work the authors explore the management of multiple levels within the LS framework. They propose an extension to the LS method that allows for handling more than two phases. In this approximation, each phase is represented by a distinct LS variable and each variable Φ_i evolves independently while periodically are allowed to interact among them based on rules defined by the authors. A significant advancement was made by Zhao et al. [58] who proposed a method that assigns

one LS variable to each region. The improvement relies on the capacity to manage complex curvature problems, as well as an improvement in the coupling which in this proposal is done with the help of Lagrange multipliers. Ruuth [59] presented a novel enhancement to Merriman's work, resulting in the elimination of both overlapping and vacuums. Hallberg [60] presents an implementation of Merrimans's work in a recrystallization model that yields favorable outcomes across multiple levels. Mao et al. [61] extend Zhao's formulation in a landslide problem where three phases are considered.

All the reported models add m or $m-1$ level set equations to manage m stable levels. Typically, this is inevitable in case tracking of each level is required while ensuring conservation of each phase.

2.4 Heat Transfer Modeling in PBF

During the heating phase in a PBF process, the powder alloy is rapidly heated, melted, and solidified. In a PBF process this heating is driven by a directed energy source like a laser or an electron beam. Due to this added energy, various regions of the build undergo many cycles of heating and cooling, which impact their local temperature history, and material properties. The heating cycles that vary in space lead to the formation of microstructures and characteristics that differ depending on the location, resulting in a non-uniform distribution. Due to the nature of the process, it is only feasible to get experimental temperature data on easily accessible surfaces of the structure, rather than in its interior regions. Transient three-dimensional (3D) temperature simulations are necessary for comprehending the crucial factors that impact the metallurgical quality of components, including spatially varying cooling rates, solidification parameters, microstructures, and residual stresses and distortion. Although PBF resembles a lot to welding, since both share a moving heat source and the creation of a molten pool, they also exhibit differences due to the distinct ways in which the heat source interacts with a powder bed. Moreover, there are significant disparities in both the scanning speeds and heat source powers. Furthermore, the surface tension phenomena play an even more important role in the PBF process than in welding due to the size of the melt pool.

Understanding additive manufacturing (AM) requires knowledge of several key features, including the interaction between the feedstock material and the heat source, the gradual accumulation of layers, the occurrence of multiple thermal cycles at specific locations as new layers are added, fluid flow, among others.

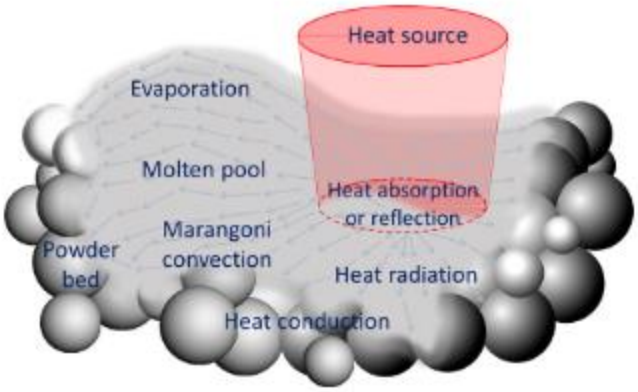

Figure 8. Heat transfer and melt pool dynamics during PBF [3].

One of the most important effects in the thermal field is the fluid flow in the melt pool as well as the interaction of the heat source with the powder bed. It is well known that the convective flow in the melt pool increases the mixing of liquid metal from various places and intensifies the heat transfer inside the molten pool, as seen in Figure 8. The circulation pattern significantly impacts the temperature distribution, heating and cooling rates, solidification pattern, as well as the microstructure and properties of the build [28], [62]. Hence, achieving precise estimations of 3D temperature distributions needs to consider the effect of fluid flow in the calculations. In equation (6) a general equation is shown that already includes most of the common effects [3], [29], [63], [64] , such as convection governed by the velocity field $\vec{v}$ and latent heat of fusion ΔH. Here, the specific enthalpy, h, is the variable to be solved for. Here k, c_p, and ρ, are the conductivity, specific heat at constant pressure and density respectively. This model is usually accompanied by a mass and momentum conservation.

$$\rho \frac{\partial h_s}{\partial t} + \nabla \cdot (\rho h_s \vec{v}) = \nabla \cdot \left(\frac{k}{c_p} \nabla h_s \right) - \rho \frac{\partial \Delta H}{\partial t} - \rho \nabla \cdot (\vec{v} \Delta H) \tag{6}$$

As can be seen, simulating heat transfer in the melt pool involves the computation of velocity fields, which is a challenging and computationally demanding process. The computing requirements for simulating the 3D transient temperature field with fluid flow are very high due to the intricate physical processes. Models often rely on simplifications to make the computations more manageable. For instance, Morville et al. [65] conducted two-dimensional idealized calculations. The advantage of performing calculations in two dimensions is to reduce computing time. Another often employed simplification is to completely exclude the fluid flow from the heat transfer, despite the fact that this is often the primary mode of heat

transmission inside the liquid pool. In these cases, it is common that the heat sources are adapted in such a way that the penetration of heat by fluid flow is compensated by introducing a volumetric heat source.

That is why most computations at macro scale use simplifications to ensure a solution in a reasonable amount of time. The surfaces of the deposited layers are commonly regarded as flat [29], [30]. This assumption has minimal impact on the temperature distribution and cooling rates in most scenarios. The thermal effects resulting from the vaporization of alloying elements are often neglected since sometimes that energy is very small compared to the energy input from the heat source. A reduced model that does not solve for the velocity field can be written as in equation (7), see [1], [6], [25], [66]. In this thermal model is solved for temperature T. The heat input $\dot{\mathrm{Q}}$ is a source term that carries the thermal effect of the fluid flow in the melt pool. Typically, this heat source tries to mimic the shape of the melt pool. A common shape is the double ellipsoidal shape, whose dimensions are adapted according to experimental results. Here the C_p is sometimes defined as the apparent specific heat to account for the latent heat effect. It is important to say that this model does not need neither the mass nor the momentum conservation. This reduction becomes very important when performing 3-D simulations.

$$\rho C_p \frac{\partial T}{\partial t} - \nabla \cdot (k \nabla \mathrm{T}) = \dot{\mathrm{Q}} \tag{7}$$

2.4.1 Heat Source

Although the laser beam and electron beam have an almost perfect Gaussian spatial distribution in a cross section [25], the interaction with surfaces and the net effect of energy over the materials can be different. When considering heat source, one important distinction can be made considering whether the heat source is implemented over a surface or volumetric.

In the first and less complex scenario, is when a circular and constant distribution is considered over a surface:

$$q_{Cir} = \frac{\eta P}{\pi r_b^2} \tag{8}$$

Here P is the total power of the heat source, r_b is the radius of the heat source, η accounts for the effective power added to the material it is sometimes considered as a constant value around 0.5, although other values are also reported.

The most realistic 2-D heat source is to use the actual distribution, which is the Gaussian distribution, as given by equation (9). Where f is the distribution factor [3], P is the total power of the heat source, r_b is the radius of the heat source and r is the radial coordinate.

$$q_{Gauss} = \frac{\eta f P}{\pi r_b^2} \exp\left(-\frac{f r^2}{r_b^2}\right) \tag{9}$$

However, applying this heat source model does not always provide correspondence with the experimental results, that is why some adjustments are frequently needed in order to better approach experimental results. The first variation that can be mentioned is the elliptic shape, where typically the longer axis is along the moving direction. That model is shown in (10), in which the $x - y$ plane is the horizontal plane. This model is already including some of the experimental results embedded in the heat source avoiding the need of including a whole physics that would lead to a more expensive model. Most of these effects emerge from powder-heat source interactions as well as the fluid flow.

$$q_{Elliptic} = \frac{\eta f P}{\pi a b} \exp\left(-f\left(\frac{x^2}{a^2} + \frac{y^2}{b^2}\right)\right) \tag{10}$$

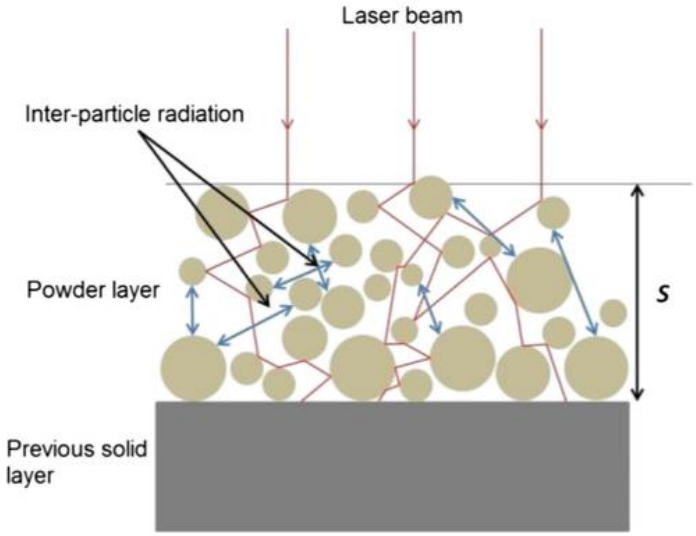

Figure 9. Sketch for the rays' reflection [58].

One hand, the powder-heat source interaction effect is because of the nature of granular material which leaves cavities that allow the energy to pass at lower levels as it is depicted in Figure 9. Additionally, the reflection of energy over the powder particles allows the energy to travel even longer distances. So, it is a

clear difference between optical properties in granular material and bulk material. This effect also modifies the net absorption of power which is around ranging from 10% to 90% according to Papazoglou et al. [25]. The overall effect is a deeper heat energy penetration and a higher absorptivity while the layer consists of powder. A deeper penetration in the raw material totally justifies the use a volumetric heat source, and in many cases is needed to get accurate results. On the other hand, the fluid flow effect significantly influences the melt pool, as it rapidly transports heat in all directions. However, due to the process characteristics, the heat mainly moves backwards and downwards, depending on the heat intensity and time interaction. This rapid heat movement means that models without fluid mechanics interaction cannot replicate the experimental results if the heat source is not tailored to align with the experimental evidence.

Probably the simplest volumetric case could be the cylindrical model with a uniform energy distribution, that can be described as follows:

$$Q_{Cir} = \frac{\eta P}{\pi r_b^2 S} \tag{11}$$

This is an extension to the circular distribution, but now is applied uniformly over a specific volume, defined as a cylinder with height S representing the optical penetration depth, which mainly depends on factors such as the powder size and powder density.

One of the best options to get a volumetric heat source in continuous absorbing media is through the Beer-Lambert absorption law:

$$\frac{dI}{dz} = -\frac{I(x,y)}{S} \tag{12}$$

Where $I(x,y)$ is the power intensity distribution over the xy-plane, z is the coordinate along the energy intensity decreases. The solution of the differential equation (13) produces a distribution along the vertical axis as is shown in Figure 10. The solution describes an exponential decay of the power intensity, being z the spatial coordinate along the beam axis, and therefore usually is equivalent to the perpendicular distance from the surface. The concentration coefficient f might vary from case to case being typically considered $f = 2$ for laser beam [25], while $f = 3$ for electron beam [67]. It is worth to mention that S in the exponential models does not represent a specific penetration depth, instead a criterium must be set,

because of the exponential decay. In this and the following models the criterion is set to exp(-1). In other words, the penetration depth is set when the energy decay reaches around the 63% of the total intensity. The spatial distribution over the other two axes perpendicular to the beam axis remains Gaussian.

$$Q_{BL} = \frac{\eta f P}{\pi r_b^2} \exp\left(-\frac{f r^2}{r_b^2}\right) \exp\left(-\frac{|z|}{S}\right) \tag{13}$$

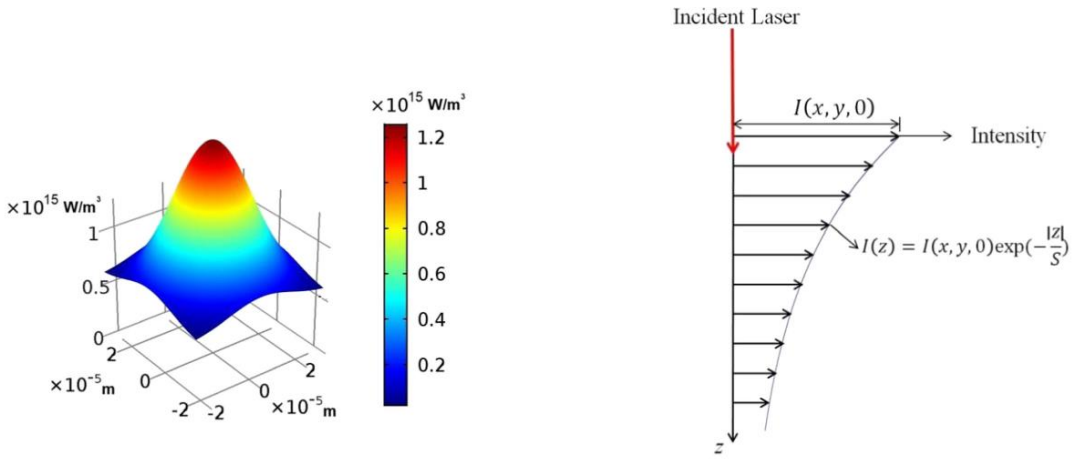

(a) (b)

Figure 10. Beer-Lambert intensity distribution (a) intensity distribution perpendicular to the beam axis, (b) intensity decay in an opaque media [68].

Although Beer-Lambert distribution is one of the most realistic heat sources, sometimes the results still do not match with experiments, especially when fluid flow is not simulated. To compensate the fluid flow effect, many researchers have adopted the Goldak distribution, which is typically an ellipsoidal distribution. This type of heat source tries to increase the range of the intensity distribution far beyond the optical penetration as an effective replacement of the effect of the convection flux that transports the heat faster from the surface to the melt pool and its surroundings, leading to a larger penetration. It is possible to distinguish between the single and a double ellipsoidal heat source, the first of which is defined as:

$$Q_{Gk1} = \frac{\eta f^{\frac{5}{2}} P}{\pi^{\frac{3}{2}} abc} \exp\left(-f\left(\frac{x^2}{a^2} + \frac{y^2}{b^2} + \frac{z^2}{c^2}\right)\right) \tag{14}$$

The Goldak double ellipsoid [69] function takes into account the experimentally observed asymmetrical melt pool shape by using two ellipsoids, where the rear ellipsoid in the melt pool has a larger axis in the

direction of the movement of the beam in comparison with the front ellipsoid which is shorter due to the movement of the heat source. The functions are described as follows:

$$Q_{Gk2} = \begin{cases} \dfrac{\eta f^{\frac{5}{2}} P}{\pi^{\frac{3}{2}} a_r bc} \exp\left(-f\left(\dfrac{x^2}{a_r^2} + \dfrac{y^2}{b^2} + \dfrac{z^2}{c^2}\right)\right) & ; \quad x < 0 \\ \dfrac{\eta f^{\frac{5}{2}} P}{\pi^{\frac{3}{2}} a_f bc} \exp\left(-f\left(\dfrac{x^2}{a_f^2} + \dfrac{y^2}{b^2} + \dfrac{z^2}{c^2}\right)\right) & ; \quad x > 0 \end{cases} \tag{15}$$

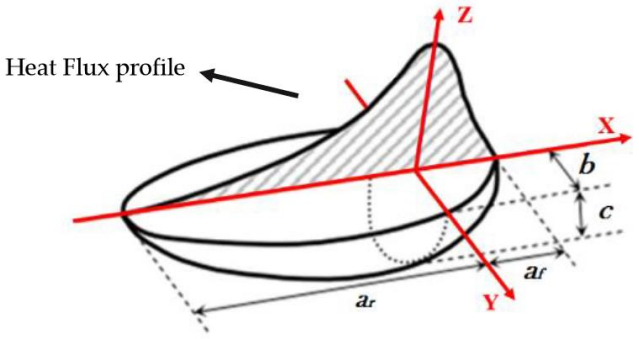

Figure 11. Double ellipsoid (Goldak) heat source, from [70].

2.4.2 Thermal Material Properties

One of the most important components in modeling are the material properties. These can completely change the system's behavior. This literature study is focused on continuum models that uses homogenization techniques to characterize the powder bed. In that sense it is possible to distinguish three distinct materials: bulk, powder, and surrounding gas. Each of these materials needs the material properties for a transient thermal analysis, such as: density, conductivity, specific heat capacity, and latent heat. Because of the high temperatures in the PBF process, material properties are also needed as function of temperature to get more accurate results.

Although not known for all the available materials, it is possible to find temperature dependent material properties for some commercial alloys. In the work of Debroy et al., [3] the material properties for SS316 and Ti-6Al-4V are shown as function of temperature according to a third order fitting polynomial defined as:

$$M(T) = A + BT + CT^2 + DT^3 \tag{16}$$

Table 1 Material properties of stainless steel SS316 and Titanium Ti6Al4V, from [30].

Alloy	**Liquidus temperature**	**Solidus temperature**	**Density**	**Thermal conductivity**	**Specific heat**
SS316	1733	1693	7800	$A = 11.82$ $B = 0.0106$ $C = 0$ $D = 0$	$A = 330.9$ $B = 0.563$ $C = -4.015 \times 10^{-4}$ $D = 9.465 \times 10^{-8}$
Ti6Al4V	1928	1878	4000	$A = 1.57$ $B = 1.6 \times 10^{-2}$ $C = -10^{-6}$ $D = 0$	$A = 492.4$ $B = 0.025$ $C = -4.18 \times 10^{-6}$ $D = 0$

The material properties for each particle of granular materials are considered the same as those of the bulk materials, however the effective properties of these powder particles, when embedded in an atmosphere of gas or vacuum, changes dramatically to the point that it is better to consider powder as a new homogenized material. Among the four material properties mentioned above the thermal conductivity is probably the most debatable property and the most complex to mathematically approach to the sufficient degree of approximation. This is mainly because of the low contact between particles that considerably reduces the conductivity. This conductivity increases when temperature increases because of sinterization that increases the surface contact, see Figure 12. This process occurs at temperatures below the melting point.

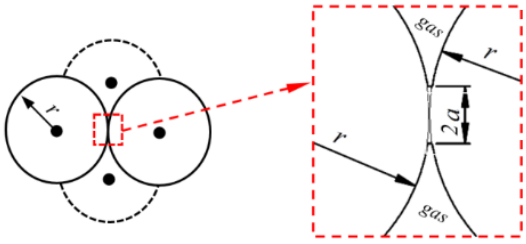

Figure 12 Sketch for the spherical powder particles contact [71].

The effective thermal conductivity of powders encompasses four primary thermal transport phenomena observed in the powder bed: the thermal conductivity of contact between particles, $k_{contact}$; thermal radiation, k_R; gas thermal conductivity, k_g; and the thermal conductivity of an individual particle of, k_S. In the work of Wakao and Kagei [72] some models are derived based on these factors. In the work of Sih and Barlow [73], a model that includes these effects is also developed but extra effects are already included In the work of Moraes and Czekanski [71] some theoretical packing techniques are calculated as temperature varies using the model of Wakao and Kagei. The series of data consider three particle sizes for each packing configuration and an inert gas atmosphere. It is possible to verify that the thermal conductivity slowly varies below the melting point.

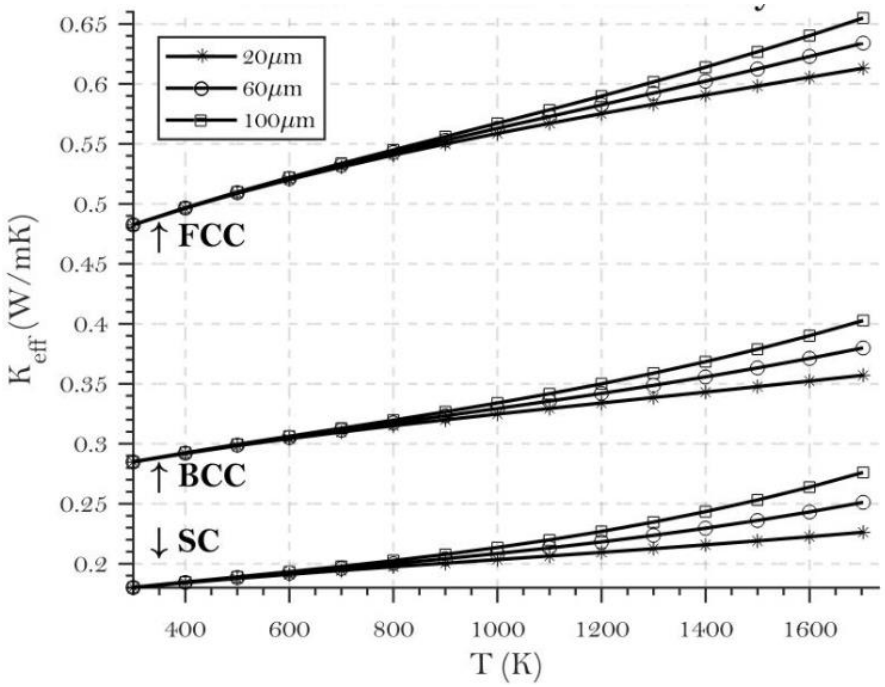

Figure 13. Effective thermal conductivity for different packing arrays: Simple cubic (SC), Body-centered cubic (BCC), face-centered cubic (FCC), with powder particles of 20,60, and 100 μm *diameter, from [71].*

Although the density in the bulk material is sometimes calculated as a property that depends on temperature, in most of the cases this is ignored, and is just considered as constant along the process. The homogenized density of the powder material, also known as the apparent density, depends on the degree of compaction or the packing density, which in its turn depends on the particle size distribution. The packing density typically is around 0.6 but could be lower or higher.

The effective heat capacity of the homogenized model is typically approached with a linear relation between the heat capacity of the bulk material and gas.

The way these material properties are added to the model is typically by continuous functions, to do that a phase function is typically added. The common linear relation is shown in Equation (17), where the phase function determines the powder location as well as bulk material location. So, the material properties are continuously defined by (18) to (20) for conductivity, density and specific heat respectively.

$$M(\phi) = M\phi + (1-\phi)M \tag{17}$$

$$k_{eff} = k_S\phi + (1-\phi)k_P \tag{18}$$

$$\rho_{eff} = \rho_S\phi + (1-\phi)\rho_P \tag{19}$$

$$\rho_{eff}c_{p_{eff}} = \rho_S c_{P,S}\phi + \rho_P(1-\phi)c_{P,P} \tag{20}$$

Another important graph is developed by Gusarov and Smurov [74] in which a ratio of effective powder conductivity is compared to the gas conductivity versus the volumetric fraction f^s showing that this ratio is ~ 10.

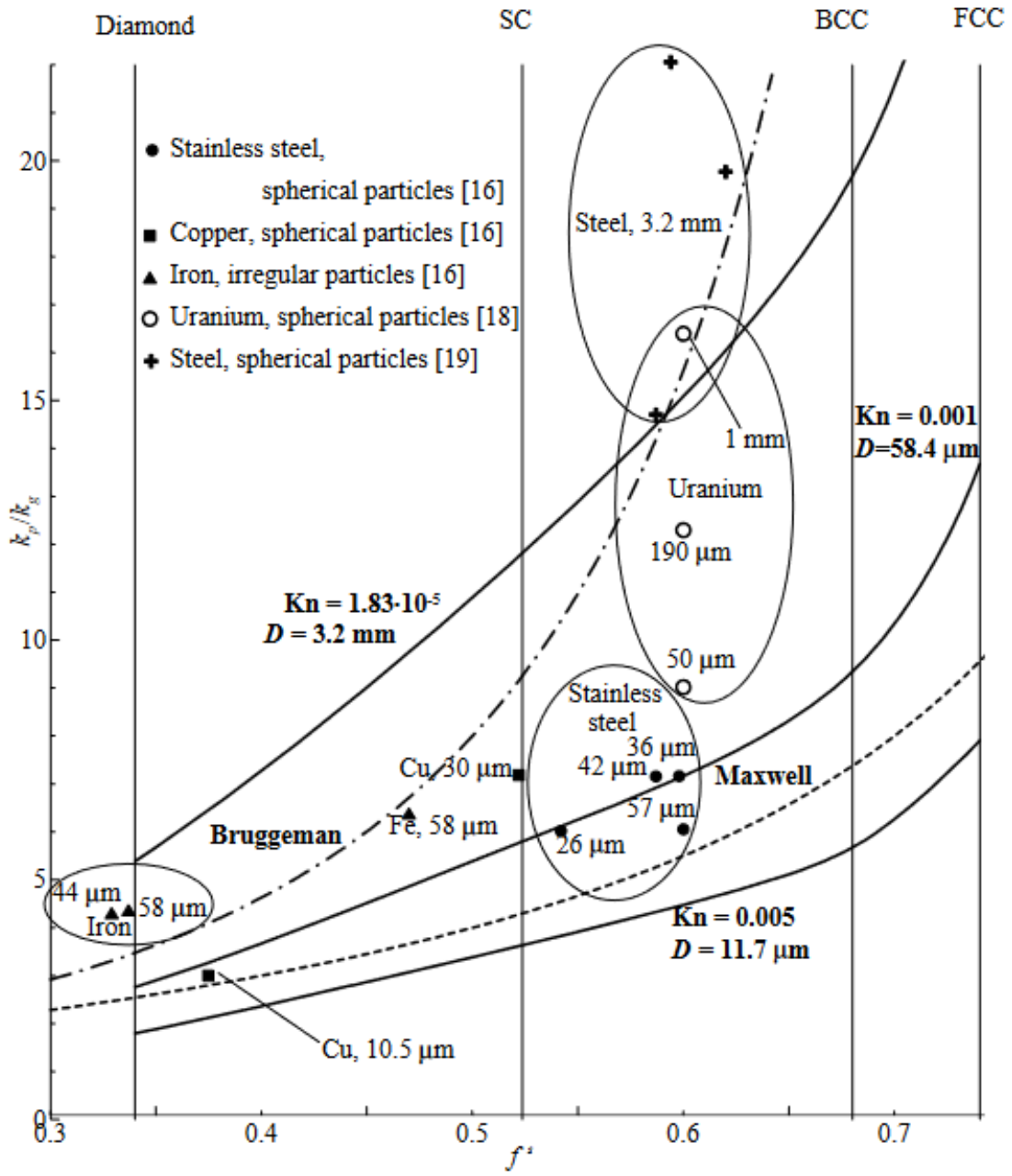

Figure 14. Ratio between effective conductivity k_p, and gas conductivity k_g as function of the solid phase fraction f^s, from [74].

3 Development of the Homogenized Multi-Density Level Set Model

This chapter is devoted to developing the core of the first subtask in the goals, which is the development of a relative density level set model that can represent and keep track of the evolving interfaces under the conservative level set paradigm. The development of this Homogenized Multi-Density (HMD) within the Level Set framework, is the foundation of this thesis. An article on this matter was published in the journal *Computer Methods in Applied Mechanics and Engineering* titled '*Efficient single variable Level Set method for capturing moving interfaces in powder densification processes'* [75].

In Chapter 4, the HMD model is extended and linked to the conservation equation of mass that is then coupled to the energy equation to model PBF processes.

3.1 Introduction

Computational time is an important issue in numerical simulations, as it influences the speed of the solution and the adoption and feasibility of its application. Factors such as the complexity of the problem, the processing power of the computer, the efficiency of the algorithms, and the amount of data that must be processed can significantly affect computational time.

The Level Set (LS) method, originally proposed by Osher and Sethian, is one of the simulation techniques to model evolving interfaces. This article focuses on developing a computationally efficient model that can handle interface problems with three interface types, exploiting an opportunity window found in the Conservative Level Set (CLS) model proposed by Olsson and Kreiss, by defining a single level set variable that is capable of capturing three stable levels. The level set variable may be seen as the mean relative density of a certain substance with three stable density levels, see Figure 15. The provided model is appropriate for representing the process of depositing and compacting powder material. It can accurately capture the three distinct materials/levels associated as void, powder, and fully dense material that coexist within the domain of interest during this process. This model is particularly useful for PBF processes such as SLM or EBM, where the evolving interfaces describing the forming product shape are of great interest. This model can also be applied to other processes where a limited set of discrete density levels have

significance. The primary benefit of the suggested model is the significant decrease in the number of degrees of freedom, resulting in reduced computer resource requirements.

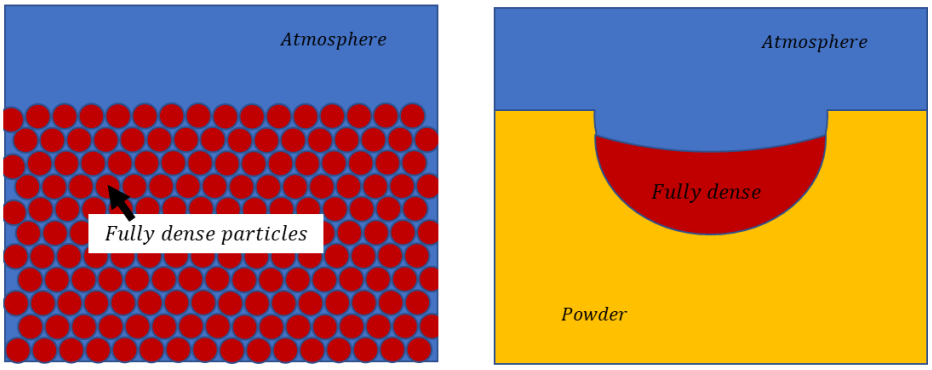

Figure 15. (a) 2-D sketch of the powder bed, (b) 2-D sketch of the three expected materials under the proposed homogenized model.

In this work, a homogenized multi-density model is developed as a variation of the well-known CLS model, suitable when working with powder bed processes such as SLM or EBM and other processes where a limited set of discrete density levels have significance. A modified formulation of the CLS method is proposed that allows for three stable levels to coexist.

In the first section of this chapter an analysis about the instabilities in the traditional CLS model are shown. In Section 3.2 the instability problem shown in 3.3 is used to derive the homogenized multi-density mode. In Section 3.4 some case scenarios are presented and discussed.

3.2 Instabilities in the Conservative Level Set Model

The traditional LS method describes the geometry boundary or interface by introducing a continuous variable, defining the interface position implicitly as the iso-surface at a specific value of the LS variable. The attractive property of the LS approach is that the surfaces can merge and segregate, thus changing the topology of the geometry without major complications. The introduction of CLS by Olsson [9] [42] modified the formulation to naturally include mass conservation, passing from a variable measuring the distance to the interface to an S-shaped smoothed continuous function that usually goes from 0 to 1. Both LS and CLS confer a clear binary character over the tracked variable, as their original objective is to represent a discrete interface between two distinct materials or levels, which are referred to as “stable levels. The proposed model enabled the possibility of tracking the three expected materials/levels in the PBF process if powder phase is treated as a uniform phase with effective properties. In this scenario, only

the material that is deposited is monitored for conservation. However, it is categorized into three distinct densities: consolidated material (fully dense material), powder, and void or air.

To verify the binary behavior of the CLS method, the diffusion and anti-diffusion terms in the Olsson model (see Eq. (5)) are explained as starting point to introduce the proposed model. The anti-diffusive flux term will be referred as f_{VC}, since it identifies the Void-Consolidated interface (VC) between the void ($\phi_V = 0$) and the consolidated ($\phi_C = 1$). The scaling factor of 4 is added for clearer understanding.

$$f_{VC} = 4(\phi - \phi_V)(\phi_C - \phi) = 4\phi(1 - \phi) \tag{21}$$

In Figure 16 the anti-diffusion term shown in (21) is plotted and it is possible to observe that the stable values of the system, zero and one, coincide with the zeros of the function. The combination of this anti-diffusive term and the diffusive term in (5) produces a stable S-shaped transition for ϕ between the two stable levels, 0 and 1, such that the diffusive and anti-diffusive terms precisely cancel when the typical S-shape is obtained. The analytical steady state solution of (5), also known as the sigmoidal function, is given by:

$$\phi(x) = \frac{1}{2}\left(1 + \tanh\left(\frac{2x}{\varepsilon}\right)\right) \tag{22}$$

The equilibrium of diffusion and anti-diffusion converges to the phase function, $\phi(x)$, the transition zone is determined by ε. The value of ε is sought to be around the mesh discretization. Therefore, its value is typically a function of the element size h. The relation between the interface thickness Δx and ε can roughly be approximated from (21) considering x as the normal distance to the interface position, such that $\nabla\phi \approx \Delta\phi/\Delta x \approx 4\phi_s(1 - \phi_s)/\varepsilon$, thus for an interface from zero to one ($\Delta\phi = 1$) and taking the maximum gradient, occurring at $\phi_s = 0.5$, the size of the transition can be underestimated as $\Delta x \approx \varepsilon$. The optimum interface thickness depends on element type, and in this work, the transition zone Δx is considered to be between 2 to 4 times the element size h, then $\varepsilon/h = 2$ to 4. In Figure 17 the transition zone is plotted on a non-dimensional axis x/h for some values of ε/h.

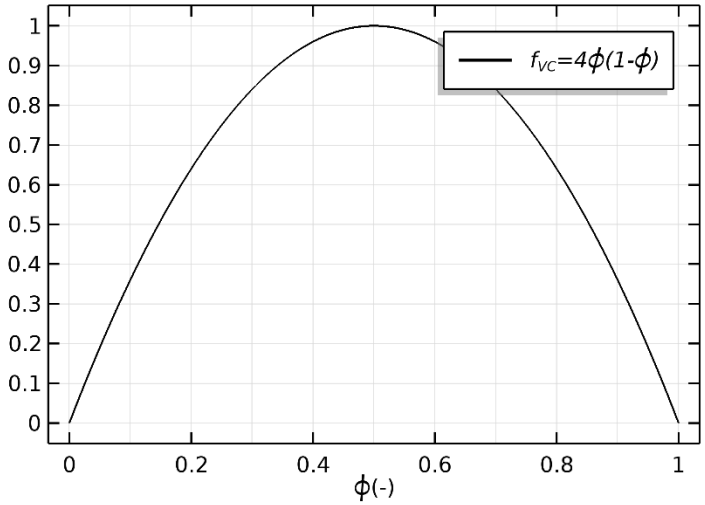

Figure 16. Anti-diffusive flux magnitude, $f_{VC}(\phi) = 4\phi(1-\phi)$; $0 \leq \phi \leq 1$.

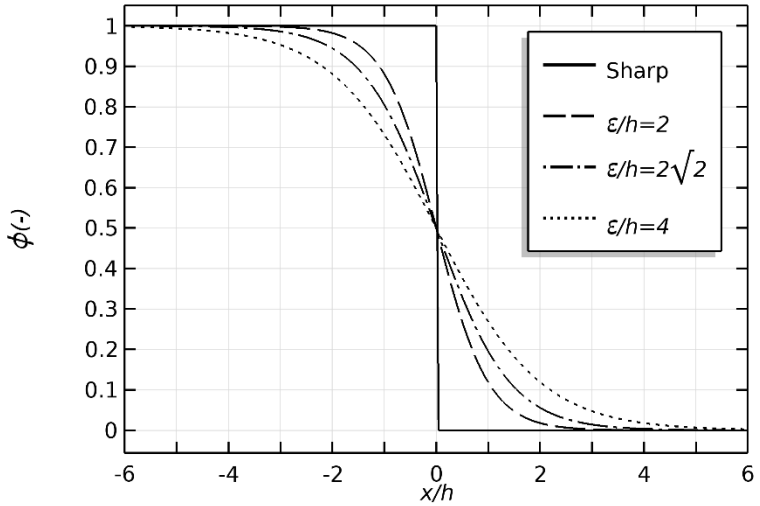

Figure 17. S-profile for different ε/h ratios, showing that the transition zone from 0.1 to 0.9 occurs around of 2h to 4h.

The instability that can be observed in the CLS takes place when the initial condition of the phase function, $\phi(x, t = 0)$, does not match one of the stable levels either zero or one. To illustrate this effect in the Olsson and Kreiss [9] model, a test case is implemented in a finite element model using Comsol Multiphysics®. The model calculates the evolution of phase function variable $\phi(\vec{x}, t)$ when the following initial conditions are set: $\phi(\vec{x}, t = 0) = 0.5$ inside a circle, $\phi(\vec{x}, t = 0) = 0$ outside the circle. A smoothed transition is set at the circular interface.

In Figure 18(a) the initial condition is shown and from Figure 18(b) to (d) the consecutive development and growth of instabilities are demonstrated. The reader can verify that the initial interface tends to be around the order of the element size, while growing by coalescence between individual peaks (Figure 18b). These instabilities emerge because the anti-diffusive flux in the plateau of $\phi = 0.5$, which produces

a ‘force’ that moves the initial value of towards one of the two “stable levels”, zero or one. This illustrates the general behavior that any initial condition with an intermediate stable level ($0 < \phi < 1$) will pulled to any of those two extrema leading to instabilities.

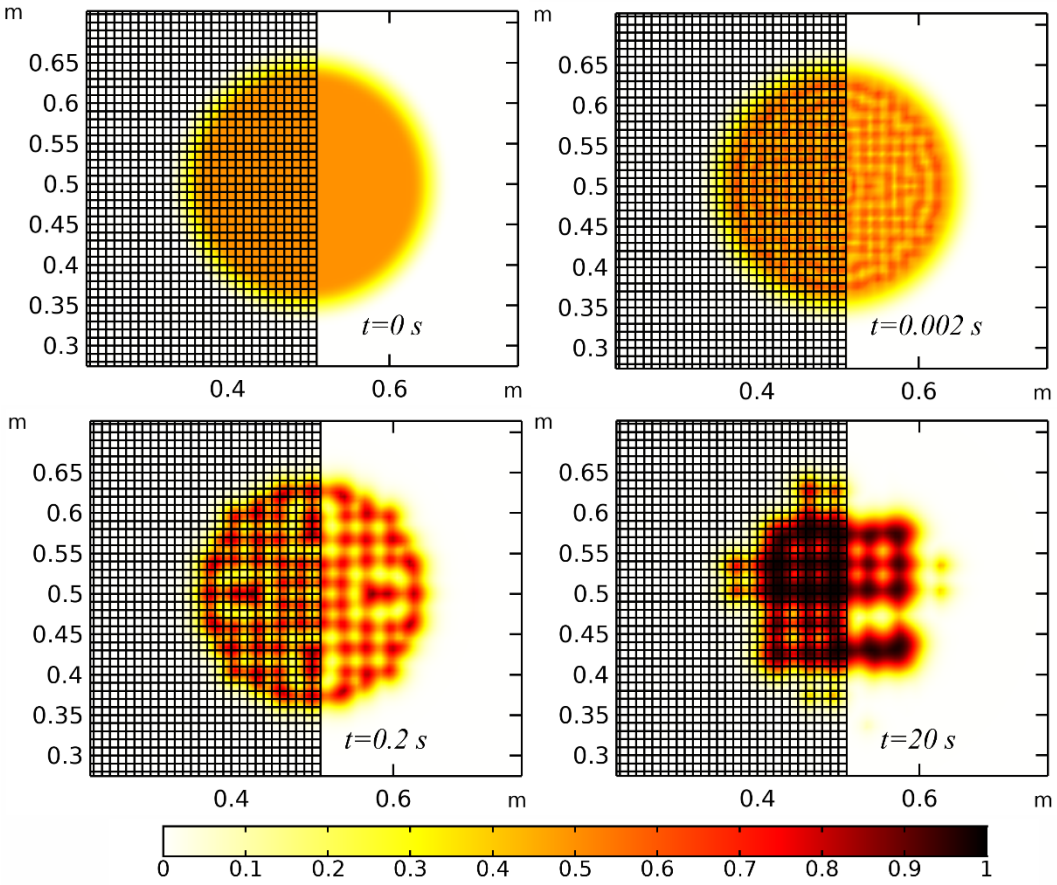

Figure 18. System instability showing the progressive development of peaks and valleys at different times when solving (5) for the intermediate value of $\phi(\vec{x}, t = 0)$=0.5. The value of γ in this study is 1.

In the stationary state of Equation (5) the diffusive flux and the anti-diffusive flux are equal: $\varepsilon\nabla\phi = f_{VC}\vec{n} = 4\phi(1-\phi)\vec{n}$. This result is shown in Figure 19, where the level set function ϕ is plotted as well as its diffusive flux term $\varepsilon\|\nabla\phi\|$. This idea is extended to propose a modified anti-diffusive term in (21) to be compatible with the three stable levels: void, powder, and consolidated.

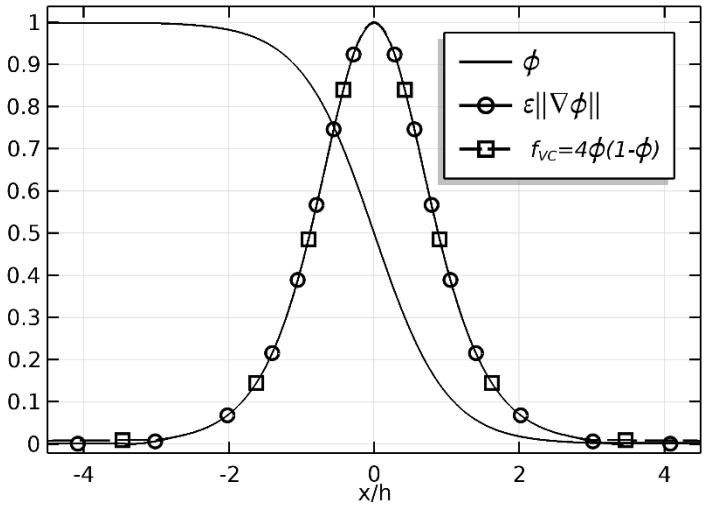

Figure 19. Level Set function ϕ, its gradient $\|\varepsilon\nabla\phi\|$ and the anti-diffusion flux term $f_{VC} = 4\phi(1-\phi)$.

3.3 Multi-Density Level Set Model

As discussed in the previous chapter, the anti-diffusion term is responsible for "pulling/pushing" the levels to one of the two stable levels, not allowing the intermediate level to remain present in a stable manner in the solution (except for the transition zone). In the present chapter, the anti-diffusive flux term is adapted to deal with three stable materials or levels: the consolidated or fully dense material ($\phi = \phi_C = 1$), void ($\phi = \phi_V = 0$), and powder ($\phi = \phi_P$) where ϕ_P could take any intermediate value between 0 and 1.

3.3.1 Development of the New Anti-Diffusion Flux Term

The proposed method extends the anti-diffusive flux term to manage the two additional smoothed interfaces: the Void-Powder interface (VP) and the Powder-Consolidated interface (PC), each defined in its zone by a similar equation of the form $(\phi - \phi_1)(\phi_2 - \phi)$ with ϕ_1 and ϕ_2 the limit values of the respective interface. Since both interfaces exist exclusively in different intervals of ϕ, both are sufficiently discernable to be incorporated into one single function f_{VPC}, that applies to the Void-Powder-Consolidated interface (VPC), as given by:

$$f_{VPC}(\phi) = \begin{cases} \dfrac{4}{\phi_P - \phi_V}(\phi - \phi_V)(\phi_P - \phi) & \phi \le \phi_P \\ \dfrac{4}{\phi_C - \phi_P}(\phi - \phi_P)(\phi_C - \phi) & \phi_P \le \phi \end{cases} \tag{23}$$

For a numerical implementation it is preferred to define a continuous derivable function, thus the function is redefined using a smoothed Heaviside function $H_s(x, \delta)$, which in this work is defined as a fifth-grade

polynomial in the interval $\langle -\delta, \delta \rangle$. The range of this function varies smoothly from 0 to 1 with continuous first and second order derivatives:

$$H_s(x,\delta) = \begin{cases} 0 & x \le -\delta \\ 0.5 + 0.9375\frac{x}{\delta} - 0.625\left(\frac{x}{\delta}\right)^3 + 0.1875\left(\frac{x}{\delta}\right)^5 & |x| < \delta \\ 1 & x \ge \delta \end{cases} \tag{24}$$

Implementing the smoothed Heaviside function, the new anti-diffusive term $f_{VPC}(\phi)$ can then be redefined as:

$$f_{VPC}(\phi) = \frac{4(\phi - \phi_P)(\phi_V + (\phi_C - \phi_V)\, H_s(\phi - \phi_P, \delta) - \phi)}{\phi_P - \phi_V + (\phi_V + \phi_C - 2\phi_P)\, H_s(\phi - \phi_P, \delta)}\ ; \qquad -\infty \le \phi \le \infty \tag{25}$$

It can be verified that for small values of δ equation (25) converges to equation (23). While function $f_{VC}(\phi)$ shows one single hump-like shape (see Figure 16), function $f_{VPC}(\phi)$ combines two hump-like shapes corresponding to two S-shaped interface transitions; one at each of the interface types. In order to obtain a similar interface thickness for each of the interface types, the two humps are scaled with the jump over the interval. The two anti-diffusion functions $f_{VC}(\phi)$ and $f_{VPC}(\phi)$ are shown in Figure 20.

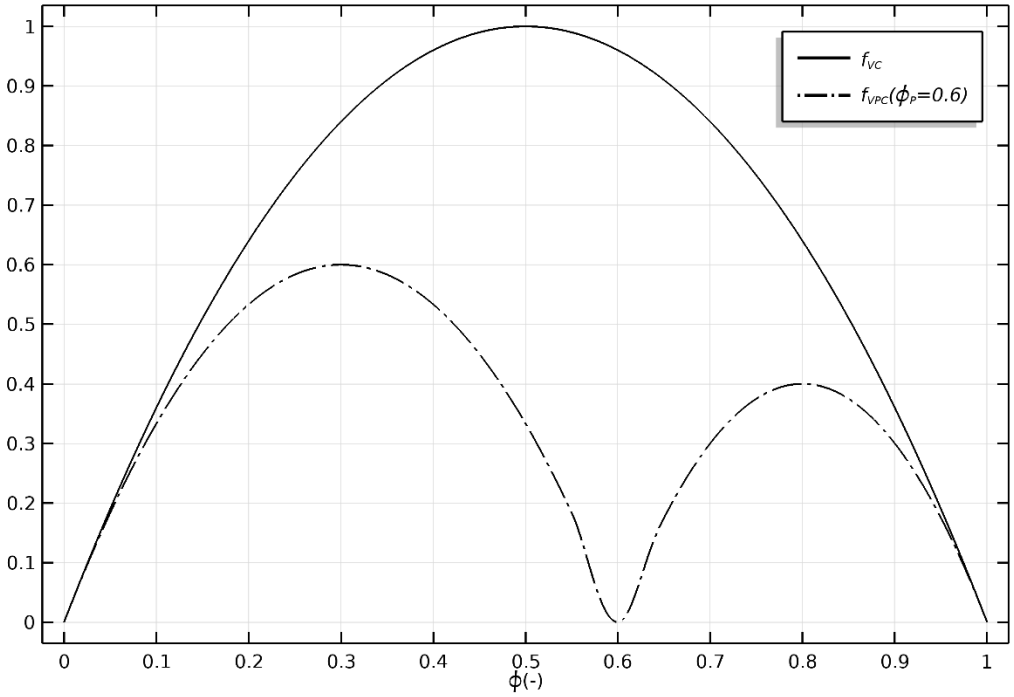

Figure 20. Anti-diffusion terms in function of ϕ showing one and two humps respectively for ϕ_P =0.6.

Rewriting Equation (5) with the proposed anti-diffusion term, the modified CLS formulation is defined as:

$$\frac{\partial \phi}{\partial t} + \nabla \cdot (\vec{v}\phi) = \gamma \nabla \cdot (\varepsilon \nabla \phi - \beta f_{VC}\vec{n} - (1-\beta) f_{VPC}\vec{n}) \tag{26}$$

where the reinitialization phase is integrated with the convective transport equation, allowing for simultaneous solution of the convection flux and reinitialization flux. This is achieved by utilizing a γ that ensures a balanced rate between the reinitialization flux terms and the convective flux. The reinitialization term on the right-hand side combines the two anti-diffusion terms using the function β, which is a switching function (Heaviside function) that determines which of the anti-diffusion terms, f_{VC} or f_{VPC}, is applied. The switching function β should be determined based on the identification of the interface type. A suitable definition of an expression is a crucial component of the proposed methodology, and the specific definition may vary depending on the particular situation. In the proposed model the switching function β relies on comparing the diffusive flow at the interface $\varepsilon\|\nabla\phi\|$ with the ideal gradient functions, it is to say $f_{VC}\ (\phi)$ and $f_{VPC}\ (\phi)$. So, the switching function depends on the local values of phase function ϕ and its gradient.

3.3.2 Development of the Switching Function β

The accurate description of the switching function β is a crucial aspect of the method, since it is important to correctly determine the kind of interface. Depending on the identified interface type, the switching function β should be assigned as $\beta = 0$ when a powder interface is detected, whether it is VP or PC interface. Conversely, β should be assigned as $\beta = 1$ when a VC is detected. This assignment ensures that the anti-diffusion term is applied correctly in equation (14). As previously stated, the interface's transition shape converges in the steady state to the applied anti-diffusion term. Consequently, any incorrect identification of the interface has the potential to amplify itself. This is because it will push/pull the transition towards the incorrect shape. While the switching function β is fundamentally a binary function, a gradual transition is employed to facilitate the usage of gradient-based solver approaches.

In order to better understand the switching function β a case scenario is performed in a triple point arrangement. The triple point test case is executed by incorporating three stable levels that converge at a central triple point, ensuring the inclusion of all interface types in the model. Equation (14) is applied for the test, following the instructions provided in the previous paragraph. However, alternative definitions of

β can also be used. The model domain is a triangular shape with sides of dimensionless length $\sqrt{3}$, forming an equilateral triangle. The initialization process involves dividing the domain into three equal portions, each separated by 120° angles around the center. In this configuration, each interface is positioned perpendicular to one of the triangle's edges and has a length of 0.5 units. Lines intersecting each interface line were added to the geometry at distances of 0.025 and 0.25 from the triple point. This was done to observe the transition curves of ϕ and β in the immediate neighborhood and the distant area relative to the triple point. Zero-flux conditions are applied to all exterior borders. A first case with non-structured mesh composed of second order triangular elements is employed with a maximum size of $h = 0.014$ and a ratio of $\varepsilon/h = 2\sqrt{2}$. A second case with non-structured mesh composed of first order triangular elements with a maximum size of $h = 0.007$ and a ratio of $\varepsilon / h = 4\sqrt{2}$. The problem is resolved with a dimensionless time period of 1 and a $\gamma = 0.25$. Additionally, to the element order, two distinct initial conditions are examined: one where the first interface transitions of ϕ are abrupt or "sharp", and a second scenario where the initial condition is sufficiently smoothed to resemble the analytical smoothed solution described in Equation (22). Figure 21(a) displays a detailed view of the region at the triple point, illustrating the "smooth" beginning condition.

In order to establish a definition for the switching function, its effect is first examined and illustrated using some basic definitions for the switching function. This will be done by considering two different scenarios, where it is possible to assess the potential risk of erroneously identifying the interface type as the wrong type and the subsequent evolution of this error. Following the presentation of these two test scenarios, a final definition will be proposed and tested.

3.3.2.1 Triple Point Scenario $\boldsymbol{\beta = 0}$

In the first scenario, the situation is assessed in which VC is not correctly identified. Then, the value of $\beta = 0$ is allocated throughout the whole domain, including at the VC interface, where the value is erroneous. This situation is possible when a VC transition becomes too smooth, causing the tiny gradient to resemble closer to the f_{VPC} value than the f_{VC} value. Consequently, in the vicinity of $\phi = \phi_P$, no anti-diffusion will be applied. As a result, the diffusion term will lead to the development of an ever-increasing plateau, with $\phi = \phi_P$, resulting in the formation of a dual S-shaped interface transition. This transition effectively divides the initial VC transition, which ranges from zero to one, into two S-shaped interfaces that pass through the stabilized, intermediate powder phase value. Essentially, this implies that instead of

having a straight transition from the void to the consolidated phase at the VC contact, an interlayer of powder is formed between two powder interfaces. Figure 21(b) displays the interfaces that occur at a time interval of 1 second, starting from the initial condition shown in Figure 6(a), when $\beta = 0$ is assigned over the whole domain. The separation of the VC into a VP and PC is clearly visible. Figure 21(c) displays the LS variable ϕ along a cut line that is perpendicular to the VC. The figure clearly illustrates both the initial S-shape and the final double "S" forms.

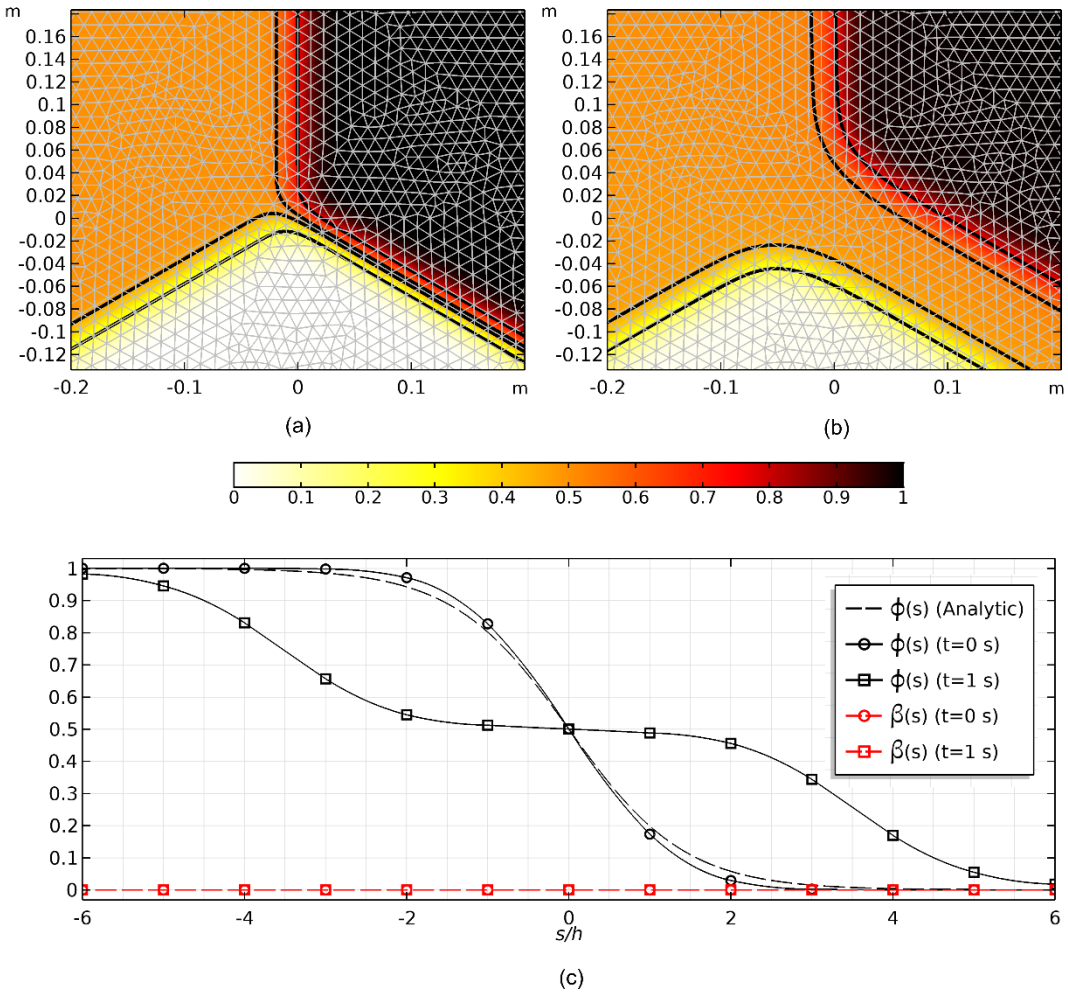

Figure 21. LS variable $\phi(x, y)$ near the triple point, (a) initial condition (smooth), (b) at the end of the transient study (t=1 s) for scenario 1 with β=0, and (c) the initial and final curves of ϕ and β over a cross-cut through the VC. The iso-contours of level sets 0.25, 0.45, 0.55 and 0.75 are shown as black lines in (a) and (b).

3.3.2.2 Triple Point Scenario $\boldsymbol{\beta = 1}$

The second example aims to investigate the consequences of mistakenly identifying a powder interface (either VP or PC) as a VC. This situation can be possible when setting a "sharp" initial condition, so the gradient of the interface is too steep causing its magnitude to approach the f_{VC} value rather than the f_{VPC}

value. As a result, the powder interface is wrongly identified as $\beta = 1$. To illustrate this situation, a value of $\beta = 1$ is assigned in nearly all the domain, except for the powder zone, where $\beta = 1$ would result in instability. Thus, $\beta = 1$ except where both criteria $0.4 < \phi < 0.6$ and $\varepsilon\|\nabla\phi\| < 0.6$ are met, in which case $\beta = 0$ is set in order to allow that the intermediate level remains stable.

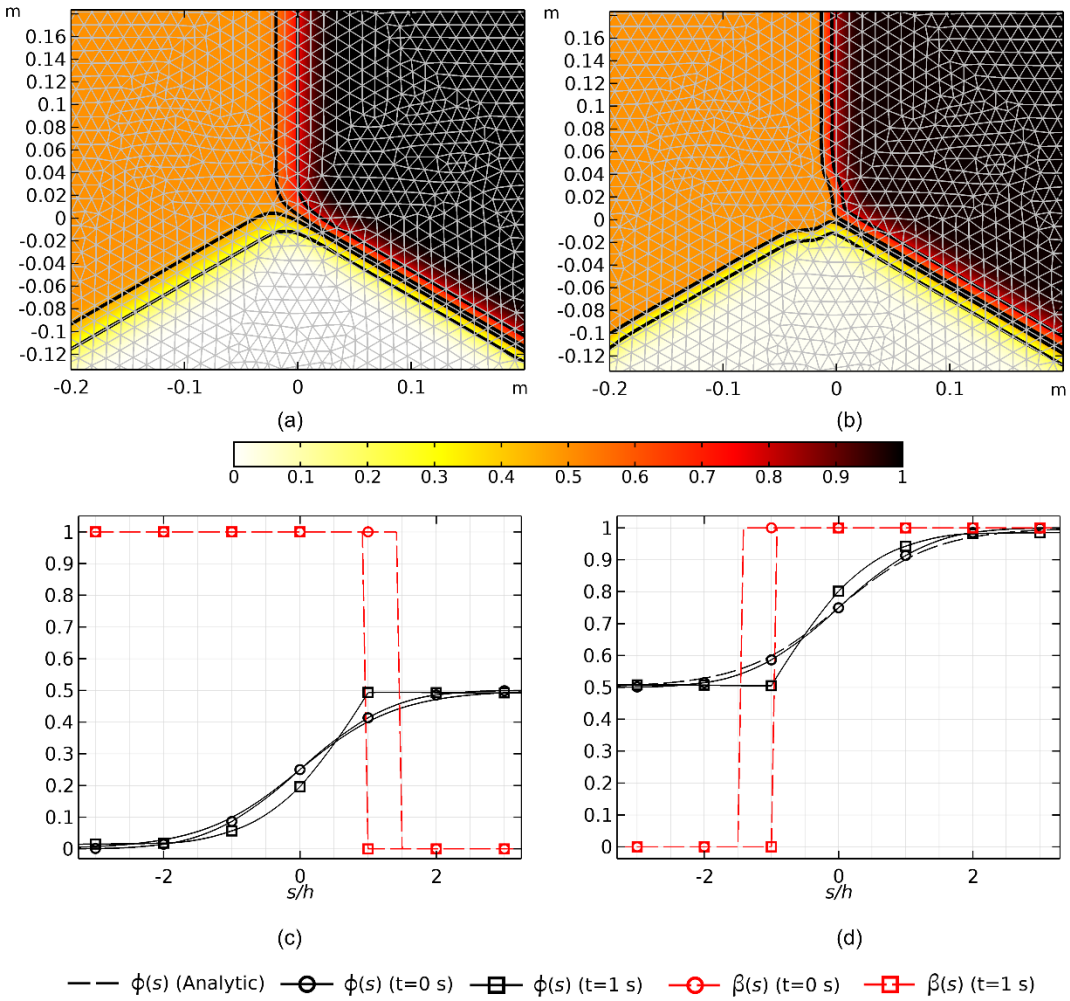

Figure 22. Results for the second scenario, showing (a) the Level Set function $\phi(x, y)$ near the triple point at the start and (b) at the end (t=1 s) of the transient study, (c) the initial and final curves of ϕ and β over a cross-cut through the VP, and (d) the initial and final curves of ϕ and β over a cross-cut through the PC interface. The iso-contours of level sets 0.25, 0.45, 0.55 and 0.75 are shown as black lines in (a) and (b).

The progression after 1 second is shown in Figure 22, which may be contrasted with the initial condition depicted in Figure 22(a). The initial and final S-transitions, as well as the β-values, are graphed along cross cut-lines that pass through the VP (Figure 22(c)) and the PC (Figure 22(d)). Both results demonstrate that the original regular S-shape is displaced and made steeper in the region where $\beta = 1$, followed by a decrease in the slope once the powder zone is reached and $\beta = 0$. At first glance, the appearance of this asymmetrical distortion in the S-shape may look acceptable, but it actually decreases the thickness of the

transition zone. Regrettably, the utilization of parabolic approximation functions in second order components leads to significant second order derivatives and the potential for an overshoot effect. These situations can lead to unwanted numerical instabilities and a decrease in convergence rate in the numerical solver. Furthermore, it should be noted that the asymmetrical transition causes a slight displacement of the interface towards the powder zone, when the halfway level set value is used as a reference for determining the interface location.

3.3.2.3 Proposed switching function $\boldsymbol{\beta}$

From the two previous instances, it is evident that it is more advantageous to use a VC type interface and assign $\beta = 1$ when uncertain. As previously stated, the determination and characterization of the switching function β may be regarded as the most crucial element of the process, and its definition may vary depending on each model. If there is existing knowledge about the expected interface type at a certain location, it might be beneficial to utilize this information to predefine the switching function β based on location. However, for the specific context of this study, the identification process relies on comparing the diffusive flow at the interface $\varepsilon\|\nabla\phi\|$ with the desired gradients $f_{VC}(\phi)$ and $f_{VPC}(\phi)$. This comparison helps define the switching function β as:

$$\beta(\phi, \|\nabla\phi\|) = \begin{cases} H_s\left(\varepsilon\|\nabla\phi\| - \left(\left(0.45 + \text{abs}(\phi_P - 0.5)\right) f_{VC}(\phi) + 0.48\, f_{VPC}(\phi)\right), \delta_\beta\right) & \text{for } 0.1 \le \phi \le 0.9 \\ 1 & \text{elsewhere} \end{cases} \quad (27)$$

H_s is smoothed Heaviside function, defined previously in equation (24) with $\delta_\beta = 0.5(f_{VC}(\phi) - f_{VPC}(\phi))$ as the transition zone. It was discovered that when ϕ_P takes certain values that make a non-symmetrical double hump function, f_{VPC} requires a little increase in the coefficient for f_{VC}. This means that the coefficient is now dependent on the specific value assigned to ϕ_P. Another important characteristic is when $\phi < 0.1 \cup \phi > 0.9$, the functions f_{VC} and f_{VPC} exhibit a high degree of similarity, resulting in a noisy definition of β. In such cases, it is recommended to set $\beta = 1$.

Given the self-amplification effect noted earlier and the reliance on the local gradient for identifying the interface type, it is crucial to supply an appropriate initial condition. Using an erroneous transition or gradient will cause the switching function β to have an inaccurate value right from the start. This means that the interface will develop into an incorrect interface. In order to provide an appropriate starting point,

it is suggested to first apply a diffusive step before proceeding with the actual solution stage. The diffusive step will effectively smear out the initial condition to correctly match the desired interface thickness. This is considered a suitable starting condition since it closely approximates the analytical sigmoidal solution of the CLS as given by Equation (22). However, a precise smoothed initial condition might not be strictly necessary, as it exemplifies the second scenario (see Section 3.2.2.2), wherein the distinct interfaces, including the powder interfaces, will result in the recognition as VC, while still yielding satisfactory outcomes.

To evaluate both scenarios, the identical triple point test case was solved by employing β as defined in Equation (27). Two distinct initial conditions were utilized: one with abrupt interfaces, where the LS variable ϕ is altered incrementally, and another with gradual transitions achieved through a diffusive preliminary step. This ensures that the initial S-profile and gradients closely resemble the corresponding analytical transitions.

3.3.2.4 Triple point quadratic elements test

Figure 23(a) and (b) depict the initial and final state of the field variable $\phi(x, y)$ for the sharp initial condition, whereas Figure 23(c) and (d) illustrate the initial and final solution for the smooth initial condition. Under the assumption of a smooth initial condition, the contours in the vicinity of the triple point exhibit small distortions, while the triple point stays stable during the measured time period. The stability of the triple point is a crucial aspect in the process, as it is challenging to determine the interface type due to the varying qualities of different interfaces that converge at the triple point. A small distortion can be appreciated, something expected since the local values of ϕ and its gradient completely define the value of β producing distinct anti-diffusion fluxes, then leading to different neighboring interfaces. However, as the distance from the triple point increases, the system demonstrates good behavior by keeping the interfaces steady.

The results for the sharp initial condition show the formation peaks in the powder adjacent to the interface. This indicates that in this particular example, the approach was unable to rectify the erroneous initial condition, and the self-amplifying effect caused the interface to develop into an incorrect interface.

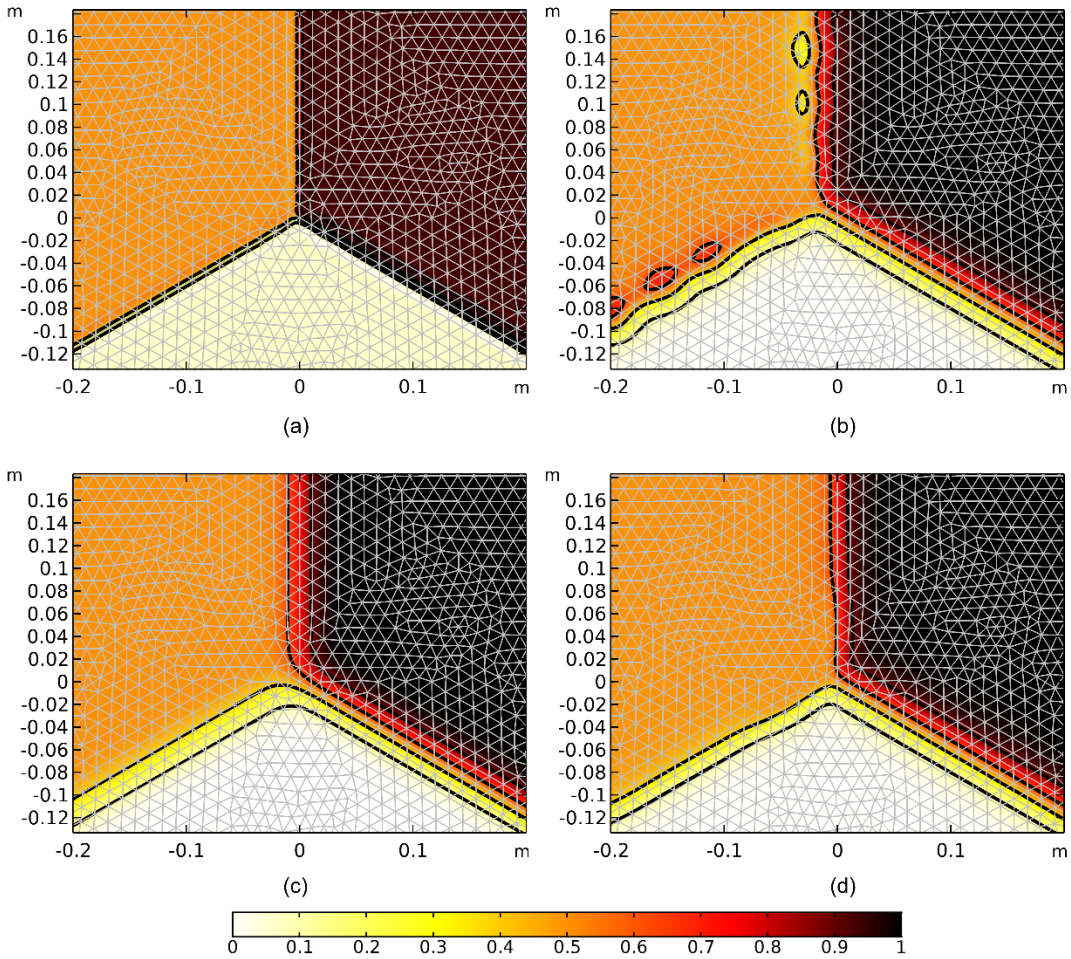

Figure 23. Level Set function $\phi(x,y)$ near the triple point, using quadratic elements: (a) the sharp initial condition, and (b) at the end (t=1 s) for sharp initial condition, (c) the smooth initial condition, and (d) at the end (t=1 s) for smooth initial condition. All cases with γ=0.25. The iso-contours of level sets 0.25, 0.45, 0.55 and 0.75 are shown as black lines.

Figure 24 (a) and (b) display the initial and final states of the switching function β for the sharp initial conditions. Figure 24 (c) and (d) demonstrate the same for the smooth initial conditions. displays the smooth initial condition. In Figure 24 (c), it is evident that the switching function β identifies the triple point as a VC ($\beta = 1$), as well as the complete VC. Additionally, the majority of the powder interfaces on the powder side are accurately identified as powder interfaces ($\beta = 0$). Figure 24(d) shows that β moved somewhat closer to the powder zone. This shift becomes more important when the triple point is approached, resulting in a larger portion of the powder interfaces being classified as VC. Consequently, there is a small movement of the boundary between the void and powder, as well as the boundary between the powder and the consolidated material. However, once this initial movement occurs, the boundaries stay steady. Conversely, in the case of the sharp initial condition, all interfaces are immediately classified as VC and assigned a value of $\beta = 1$. Figure 24(b) shows that, the PC is still recognized as a VC. This identification has caused the formation of peaks exhibited in Figure 24 (b). It is evident that the sharp

initial transition and the self-amplifying impact are the primary factors contributing to the inaccurate progression of the interface. It is important to note that decreasing the preference for $\beta = 1$ raises the likelihood of deformation of the triple point. This can result in the split of the VC contact into two powder interfaces, with a powder layer in between, as demonstrated in scenario 1.

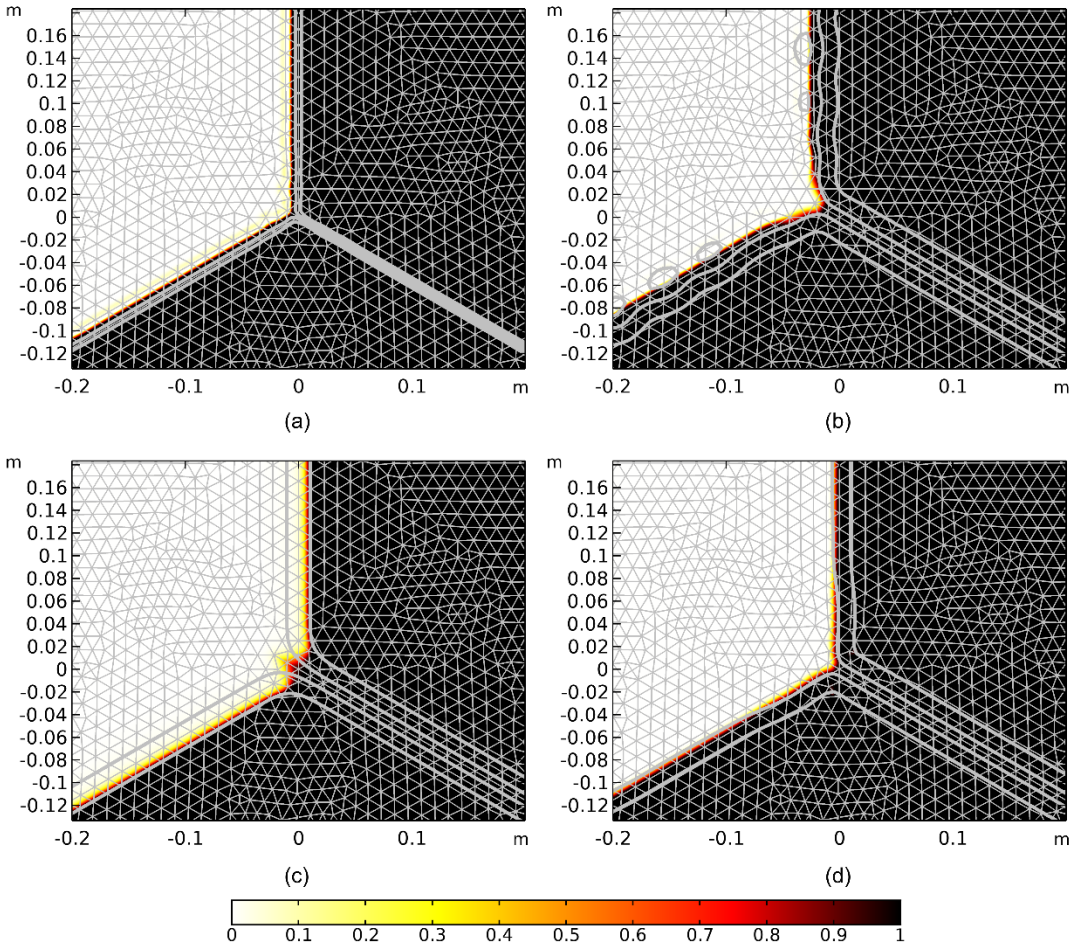

Figure 24. Switching function β near the triple point for quadratic elements, (a) at the start and (b) at the end of the transient study (t=1 s) for sharp initial conditions, and (c) at the start and (d) at the end (t=1 s) for smooth initial conditions. The iso-contours of level sets 0.25, 0.45, 0.55 and 0.75 are shown as gray lines.

Figure 25(a) and (b) display the ϕ and β curves along a cross-cut line that is perpendicular to the PC, near the triple point. The figures also include the analytical sigmoidal solution of ϕ for both the sharp and smooth initial condition situations. Figure 25(c) and (d) provide identical graphs with cross-cut lines positioned at a greater distance from the triple point, which will be referred to as the far field. The leftmost pictures (a) and (c), depict the analytic initial condition of the LS variable ϕ, which is then transformed into quadratic approximation functions. For the sharp initial condition, the overshoot phenomenon is present, which arises due to the quadratic approximation's inability to accurately capture sudden changes.

It is important to mention that the markers on the curves correspond to the vertices of the elements. The quadratic element does not have any markings on its inner nodes. The postprocessing approach carefully subsamples the curves linking the markers, allowing for the appreciation of the applied quadratic approximation functions. The initial condition exhibits a smoothness that closely resembles the theoretical transition curve, which is shown by a dashed line without markers. The β curves exhibit significant fluctuations that cannot be accurately captured by the approximation functions. However, the β curve is derived from the (subsampled) evaluation of β, which is a highly non-linear function of ϕ and its gradient, both of which display substantial changes.

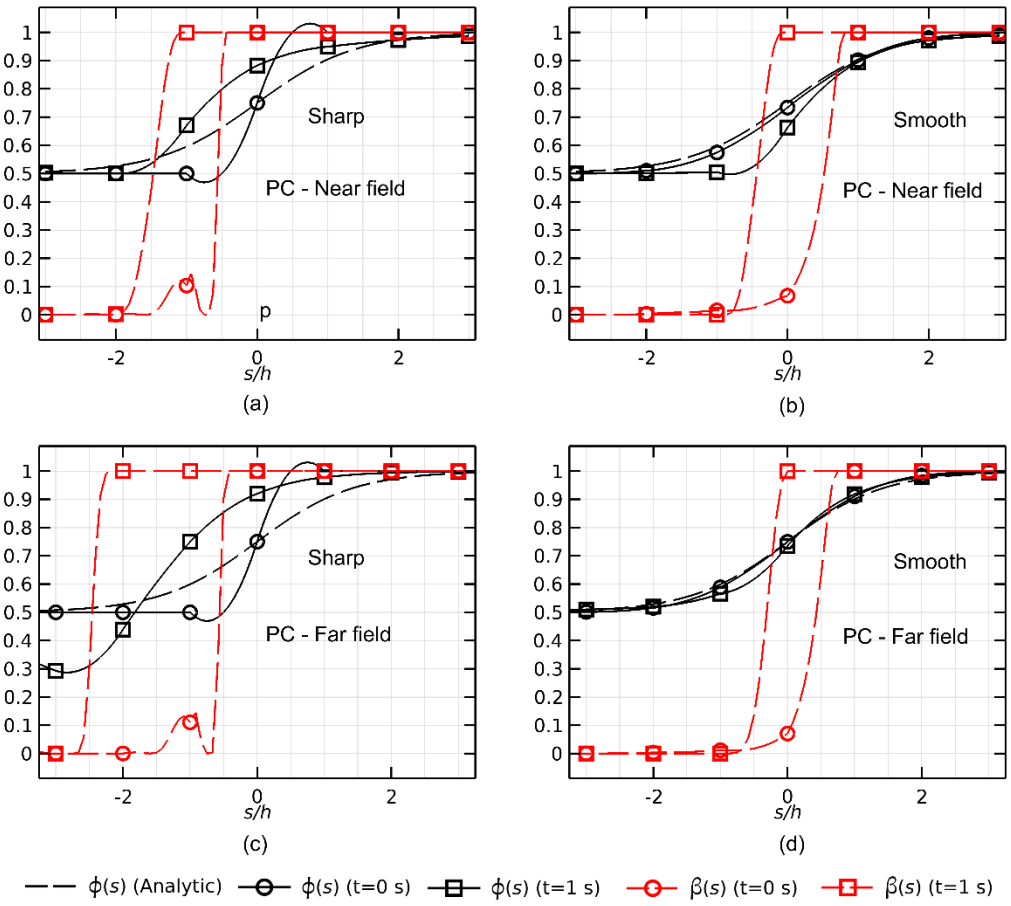

Figure 25. Comparison of the analytical smoothed transition and the initial and final states of the transient study for quadratic elements, (a) & (c) for the sharp and (b) & (d) the smooth initial condition cases, with (a) & (b) are taken near the triple point and (c) & (d) are taken in the far field.

In this transient study of $t = 1$ s, it is evident that in the immediate vicinity for both the sharp and smooth scenarios, the transition is noticeably asymmetrical. This is characterized by an excessively steep gradient on the right side and a sudden decrease in the gradient on the left side upon reaching the powder level.

The outcome is comparable to what was found in the second case, and it is evident that the switching function $\beta = 1$ is present throughout the majority of the interface. When observing the findings in the far region, it is evident that the sharp and smooth initial conditions exhibit distinct transitions. In the smooth case, the transition is more symmetrical and smoother, resembling the analytical transition. However, in the sharp situation, Figure 25(c) displays an asymmetrical transition with a significant overshoot, which may be attributed to the peaks observed in Figure 23(b).

3.3.2.5 Triple Point Linear Elements Test

To assess the method's independence from discretization and numerical methods, the same tests were conducted using linear elements with an equal number of nodes, that means that there are twice as much elements as in the quadratic case. To maintain the same transition thickness as in the quadratic case, the ratio ε / h is twice as large. Upon comparing Figure 23 and Figure 26, it is evident that the results are nearly identical, with the exception of subfigures (b) which demonstrate that linear components do not produce overshoot peaks. The plots of the β function for linear elements exhibit a high degree of similarity to those depicted in Figure 24. Figure 27 demonstrates that the curves of ϕ and β exhibit a similar trend as seen in Figure 25. However, it is important to note that the elemental approximation functions are now linear. Therefore, the linear model effectively prevents the creation of peaks in the sharp initial condition.

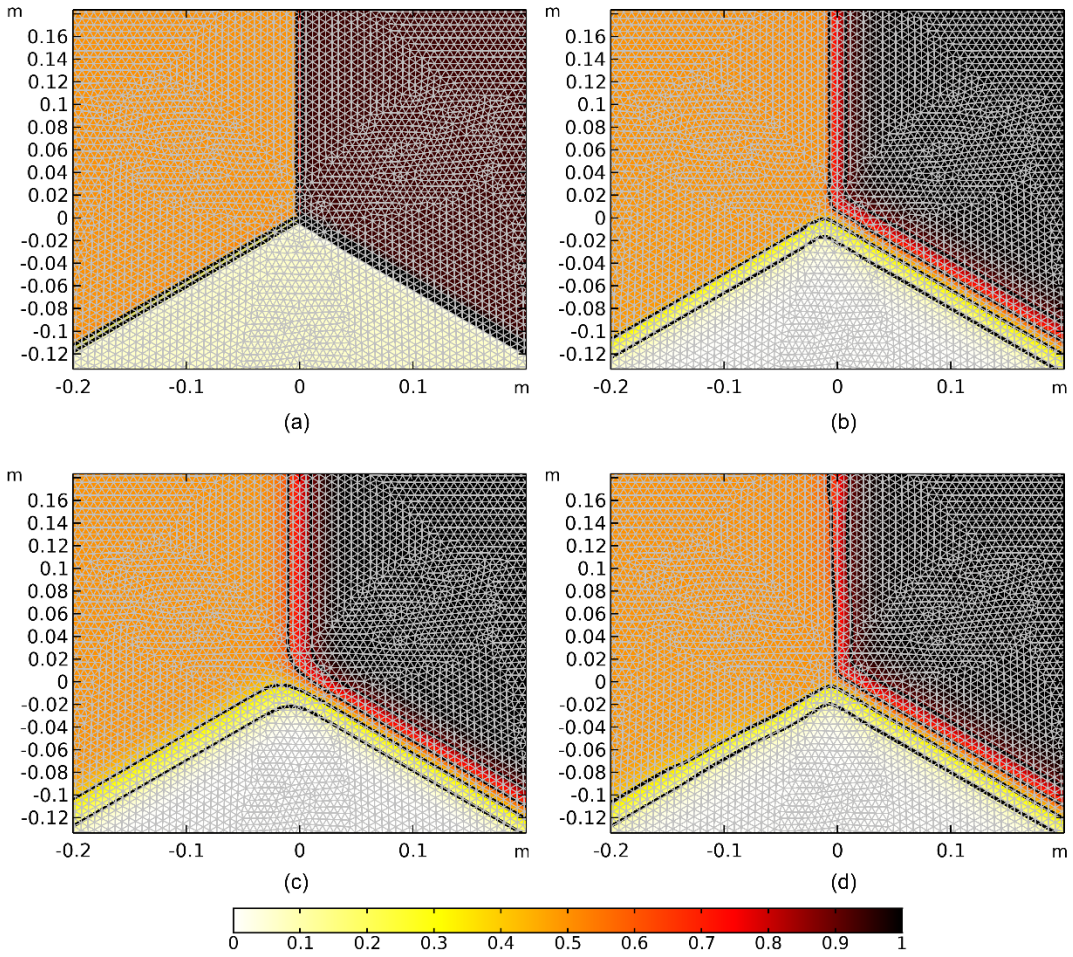

Figure 26. Level Set function $\phi(x, y)$ near the triple point, using linear elements: (a) the sharp initial condition, and (b) at the end (t=1 s) for sharp initial condition, (c) the smooth initial condition, and (d) at the end (t=1 s) for smooth initial condition. All cases with $\gamma = 0.25$. The iso-contours of level sets 0.25, 0.45, 0.55 and 0.75 are shown as black lines.

The final transition curves of ϕ depicted in Figure 27(a), (b), and (c) exhibit a consistent and distinct shape characterized by an asymmetrical form. In the case of a smooth initial condition, the transition stays smoother in the far field, since a greater portion of the transitions may still be classified as a powder interface.

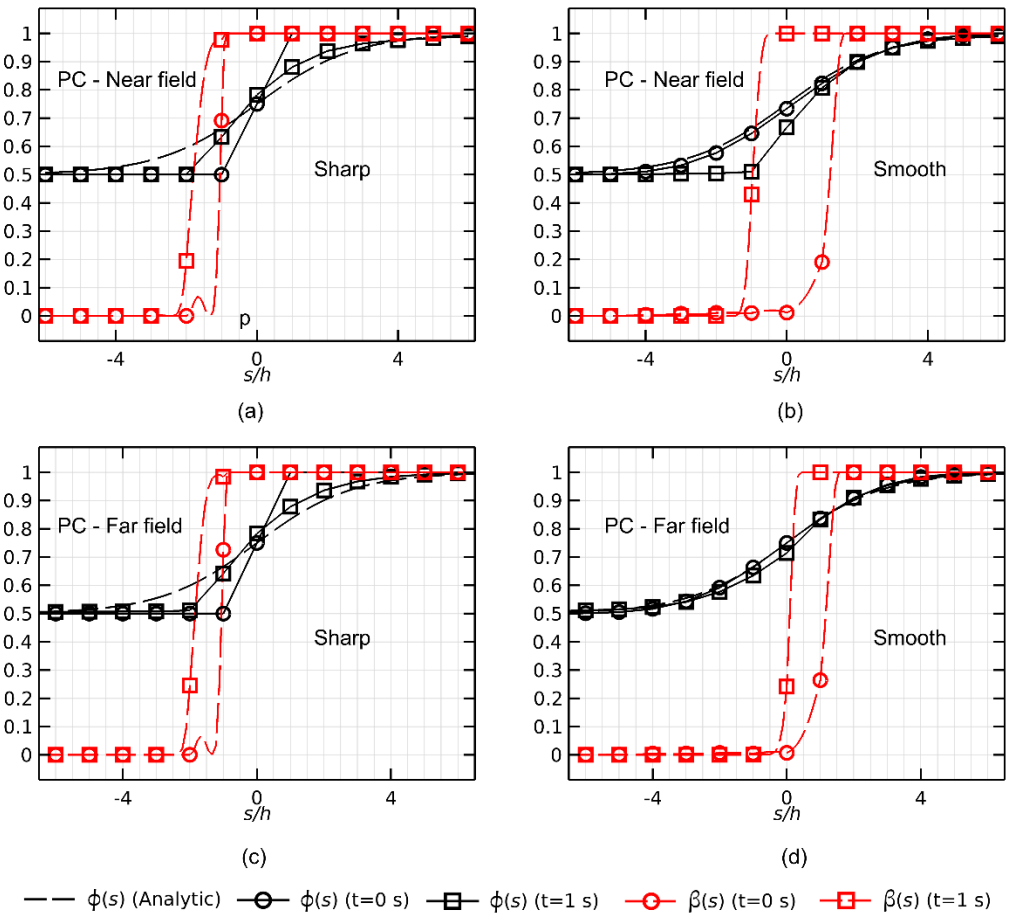

Figure 27. Comparison of the analytical smoothed transition and the initial and final states of the transient study for linear elements, (a) & (c) for the sharp and (b) & (d) the smooth initial condition cases, with (a) & (b) are taken near the triple point and (c) & (d) are taken in the far field.

3.3.2.6 Discussion About the Triple Point Case

The triple point analysis indicates that the final transition curve shapes are almost identical for both the sharp and smooth initial conditions. In both cases, the near field rapidly transforms into an asymmetrical transition, while the far field tends to transform into a smoother symmetrical transition. However, this process is not successful for quadratic elements if the starting condition is sharp. This suggests that, in contrast to what was expected, the self-amplifying effect actually raises the risk of incorrectly identifying the interface, resulting in undesired deformations and peaks. However, the method does offer some flexibility that allows the transitions to develop into an acceptable, though asymmetrical, transition. Hence, it is recommendable to correctly smoothens the transitions in the initial condition. However, the approach has demonstrated a robust response in many tests, even when the initial condition is sharp, especially for the linear components.

3.4 Normal definition

Along this thesis the adopted definition of the normal vector aims to prevent division by zero or by small magnitudes. A cut-off criterion is used to achieve this, effectively annihilating the normal vector's magnitude when the gradient falls below the cut-off threshold. Through testing, it was determined that a gradient of 1% of the maximum expected value yields the desired performance. Considering that the flux gradient $\varepsilon\|\nabla\phi\|_{max}$ is approximately equal to one, the definition used in this study is:

$$\vec{n} = \frac{\varepsilon\nabla\phi}{\max(\varepsilon\|\nabla\phi\|, 0.01\ )} \tag{28}$$

3.5 Case Studies

The proposed HMD model that encompasses equations (25) to (27), is implemented and evaluated in several case studies to assess the capacity of the model. It is worth to mention that this series of case scenarios only include the HDM by itself and no other physics is added.

Table 2 List of cases

Case	**Level set values (stable)**	**Characteristic to be evaluated**
Zalesak disc 2 levels/materials	$\phi_V = 0$ $\phi_P = 0.5$ $\phi_C = 1$	Pure advection of two levels/materials with. Rotation plus translation. Shape must be preserved.
Zalesak disc 3 levels/materials	$\phi_V = 0$ $\phi_C = 1$ $\phi_P = \{0.25,0.5,0.75\}$	Pure advection of two levels/materials with. Rotation plus translation with three levels/materials. Shape must be preserved.

Falling drop	$\phi_V = 0$ $\phi_P = 0.5$ $\phi_C = 1$	Advection and densification of an intermediate level/material
Densification of the intermediate level/material	$\phi_V = 0$ $\phi_P = 0.5$ $\phi_C = 1$	Advection, creation, and densification of an intermediate level/material

The first case replicates the Zalesak [76] test, where a slotted disk undergoes both rotation and translation to evaluate the effectiveness of HMD in pure advection. The initial condition in this only includes two stable levels. The second case study is an extension of the Zalesak test, where a disk with two distinct levels/materials is rotated in a third level/material. The third case study demonstrates a scenario in which a powder volume becomes denser as it falls and impacts a surface that is already fully dense. This visual representation illustrates the process of compacting and the interplay between the three levels. The fourth case study shows the process of local compaction of powder that would typically take place in a selective powder bed process. The four case studies were designed to assess the capacity of the HMD model and will be discussed in the subsequent sections. Table 2 shows a summary of cases to be simulated and Table 3 contains generic data that is applicable to all test situations.

Table 3 Common data for all four cases studies

Domain	$\Omega = \{(x, y) \mid 0 \leq x \leq 1;\ 0 \leq y \leq 1\}$	
Element type	Rectangular	
Element order	Linear	Quadratic
Mesh size	200×200 elements	100×100 elements

Diffusion coefficient	$\varepsilon = 4\sqrt{2}\,h = 0.0283$	$\varepsilon = 2\sqrt{2}\,h = 0.0283$
Reinitialization factor	$\gamma = 0.0625$ (case I and II) $\gamma = 0.25$ (case III and IV)	

The computations were carried out using a computer equipped with a 12th generation Intel® CoreTM i9-12900 processor operating at 2.4 GHz. The number of time steps and the amount of time spent by the CPU are presented in Table 4. There was an automated determination of time steps; nevertheless, the time step was maximum at 0.0005 for examples I and II.

Table 4 CPU usage and time steps for the different case studies and element types

		# Time steps	***Total CPU time***
Cases I and II	100 × 100 quadratic elements	2202	382
	200 × 200 lineal elements	2202	427
Case III	100 × 100 quadratic elements	463	307
	200 × 200 lineal elements	474	395
Case IV	100 × 100 quadratic elements	472	338
	200 × 200 lineal elements	634	570
	100 × 100 lineal elements	690	141

3.5.1 Case: Zalesak Disc 2 Levels

In order to test the HMD model in pure convection, a slotted disc of radius 0.15, a slot width of 0.05 and slot depth of 0.25 is tested in translation and solid body rotation. The disc completes a full revolution around a point which is the domain center (0.50,0.50) using a velocity field defined by $v_x = -2\pi(y - 0.5)$ and $v_y = 2\pi(x - 0.5)$. The disc starts and finishes with its center position in (0.50,0.75).

Figure 28(a) and (b) show the ϕ-field at the start and at the end of the analysis in which the object makes a full revolution about the center point at $(0.5,0.5)$ respectively. In Figure 29, the initial and final shapes of the disc are shown by plotting the $\phi = 0.5$ isocontours in a single plot, which demonstrates that the shape after one revolution is kept correctly, except for some rounding off at the corners, something expected in the LS method. The test case was also solved for other combinations of stable values ϕ_V, ϕ_P or ϕ_C to verify that the proposed method behaves equivalent to the original method proposed by Olsson and Kreiss [47] for any combination of stable values as initial condition. It is to say, the model converges to the Olsson and Kreiss model when only two levels are modeled.

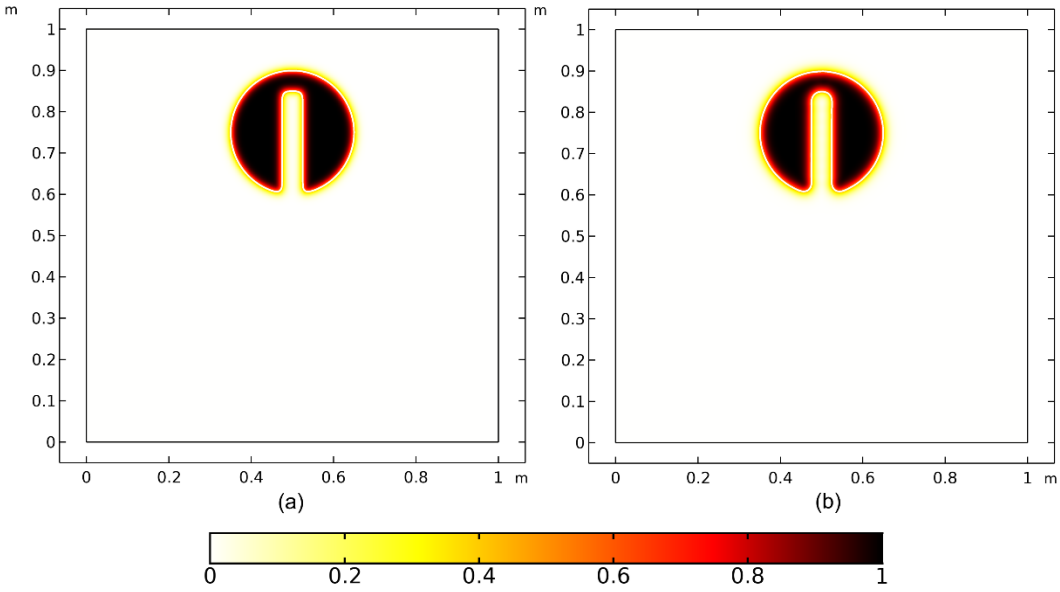

Figure 28. ϕ-field for Zalesak disc test for one disc. a) Initial condition, b) Final state.

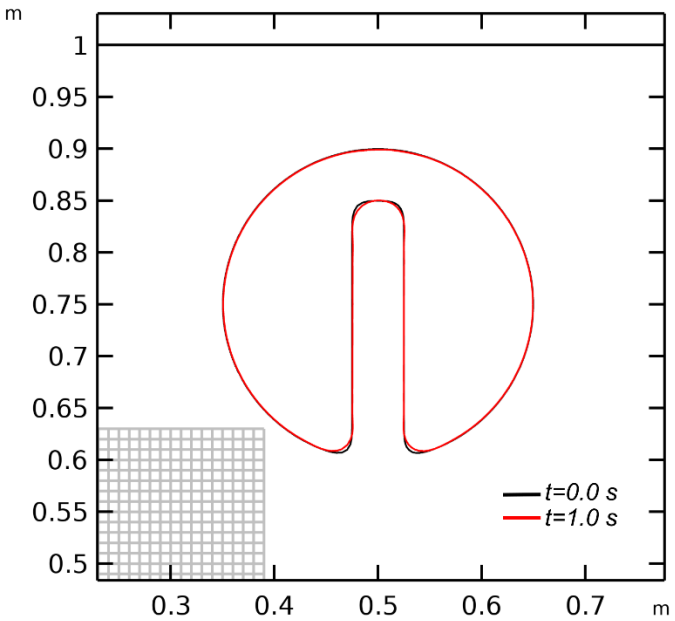

Figure 29. Initial and final contour curves ϕ=0.5 for Zalesak disc test for one disc and two levels showing some rounding off at the edges.

3.5.2 Case: Zalesak Disc 3 Levels

To test the interaction and coexistence of the three levels, a variation of the original Zalesak test is carried out. The variation consists in adding one extra level to the disc, half of the disc is one level/material while the other half is another level/material. In this multi-level Zalesak disc model, the performance is tested for the advent of instabilities or inconsistencies in the interface. So, a bi-material slotted disc with the same dimensions and rotation velocity of previous case study are used. Specifically, the upper half of the disc is set at an initial value of $\phi = 1$, and the lower half is set at $\phi = 0.5$. In Figure 30(a) and Figure 30(b) are shown the initial and final states after the disc rotates one revolution. Like previous case study, the shape is preserved with no more alterations but the expected rounding off. In Figure 31 the switching function β is graphed, demonstrating the correct identification of the powder zone with its two interfaces VP and PC ($\beta = 0$) versus the VC zone and VC ($\beta = 1$).

In Figure 32(a) and (b), the initial and final iso-contours are shown. The iso-contours of $\phi = 0.25$ and $\phi = 0.75$ represent the VP and the PC, respectively. The sections where a VC is located, the position should be given by the $\phi = 0.5$ isocontour. The contours demonstrate the shape and position of the disc showing that the disc movement was correct with a reduced rounding off in its corners. It is important to notice that the observed expansion of the disc's radius and contraction of the slot's width in the upper half of the disc is due to the representation of the $\phi = 0.25$ contour. In reality, the disc interface in the upper half would be determined by the $\phi = 0.5$ contour, which lies between the two isocontours displayed. In

conclusion, this model exhibits four triple points that were previously mentioned. These points are identifiable as the locations where the isocontours converge or diverge. Although the curves exhibit disruptions at these locations, as anticipated from previous findings, these disruptions are confined to the immediate neighborhood of the triple points.

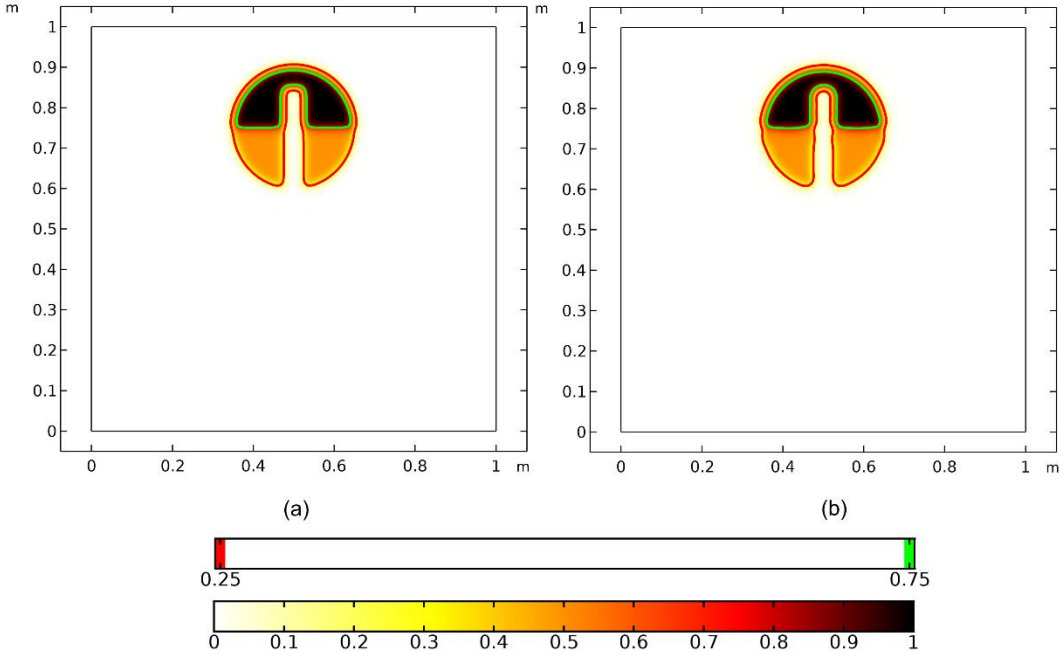

Figure 30. Zalesak disc case study for one disc and three levels. 100×100 mesh; a) ϕ-field at the start; b) ϕ-field at the end of simulation.

To showcase the capability of the proposed model in dealing with various intermediate level set values, the three-level-Zalesak disc test is replicated for other levels of ϕ_P. So, the interface contour in each case can be calculated averaging stable values. In Figure 32 it is displayed the ϕ-field for three different powder values: ϕ_P=0.25, ϕ_P=0.5, and ϕ_P=0.75. The figure also includes the interfaces along with their corresponding contours. Figure 33 depicts a comparison of the starting and final states after having completed one revolution. The comparison is conducted by examining the interface contours of each state. It is possible to observe some differences between the two states, particularly in the vicinity of the triple points, as previously described.

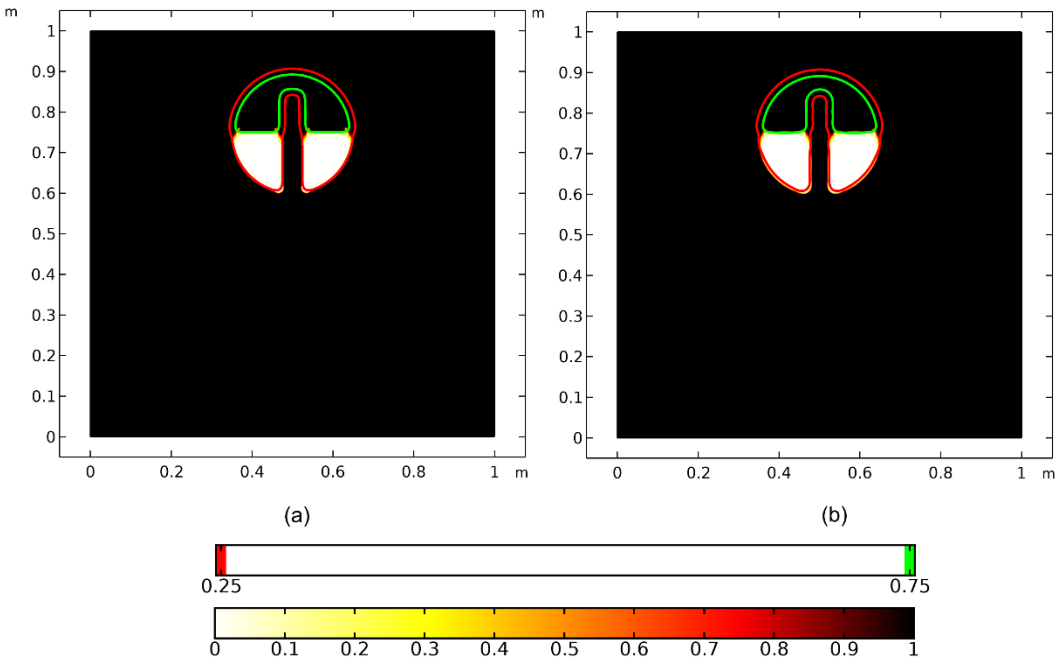

Figure 31. Zalesak disc case study for one disc and three levels, 100×100 mesh; a) β-field at the initial condition; b) β-field at the end of the simulation.

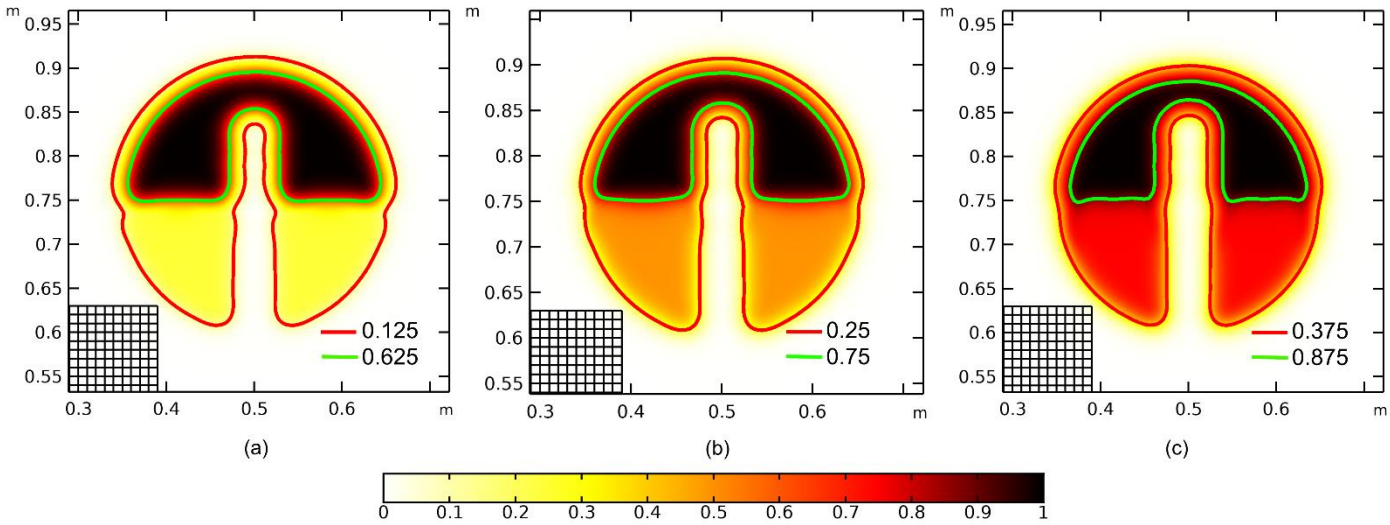

Figure 32. ϕ-field for three phases Zalesak disc test after one revolution, 100×100 mesh; a) $\phi_P = 0.25$, contours indicate ϕ=0.125 and ϕ=0.625; b) ϕ_P=0.5, contours indicate ϕ=0.25 and ϕ=0.75; c) ϕ_P=0.75, contours indicate ϕ=0.375 and ϕ=0.875.

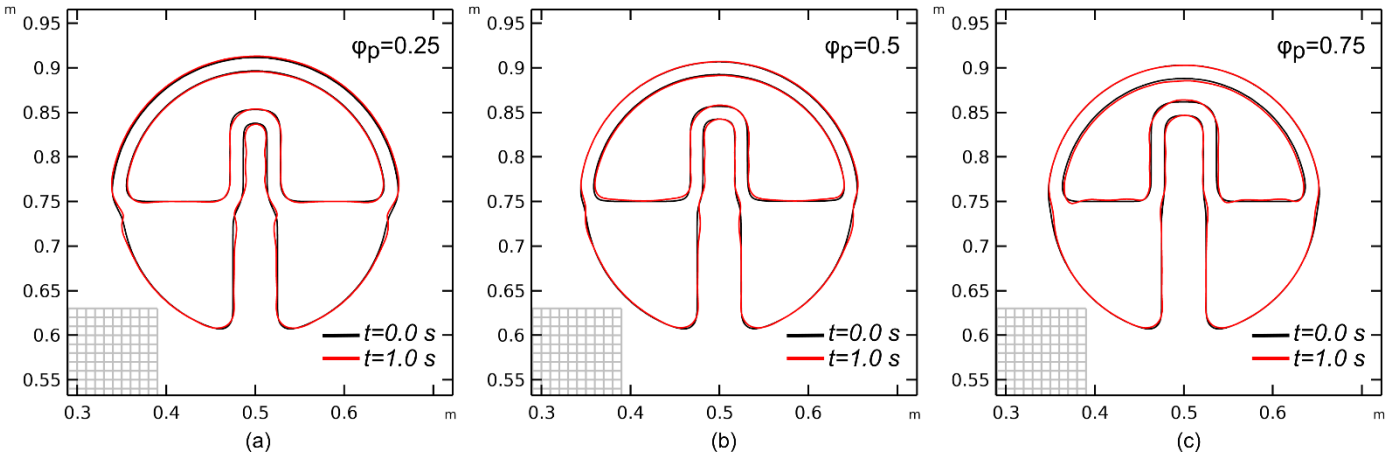

Figure 33. Comparison for the initial and final state of the ϕ-field for three phases Zalesak disc test after one revolution, on a 100×100 mesh. (a) ϕ_P=0.25, contours indicate ϕ=0.125 and ϕ=0.625. (b) ϕ_P=0.5, contours indicate ϕ=0.25 and ϕ=0.75. (c) ϕ_P=0.75, contours indicate ϕ=0.375 and ϕ=0.875.

To evaluate the performance of the meshing the three levels Zalesak test is repeated for the same three powder values: ϕ_P=0.25, ϕ_P=0.5 and ϕ_P=0.25, but now twice the number of elements, it is to say 200×200 elements mesh. The results are shown in Figure 34, where a considerable improvement can be appreciated, especially in the corners where the rounding effect is less apparent.

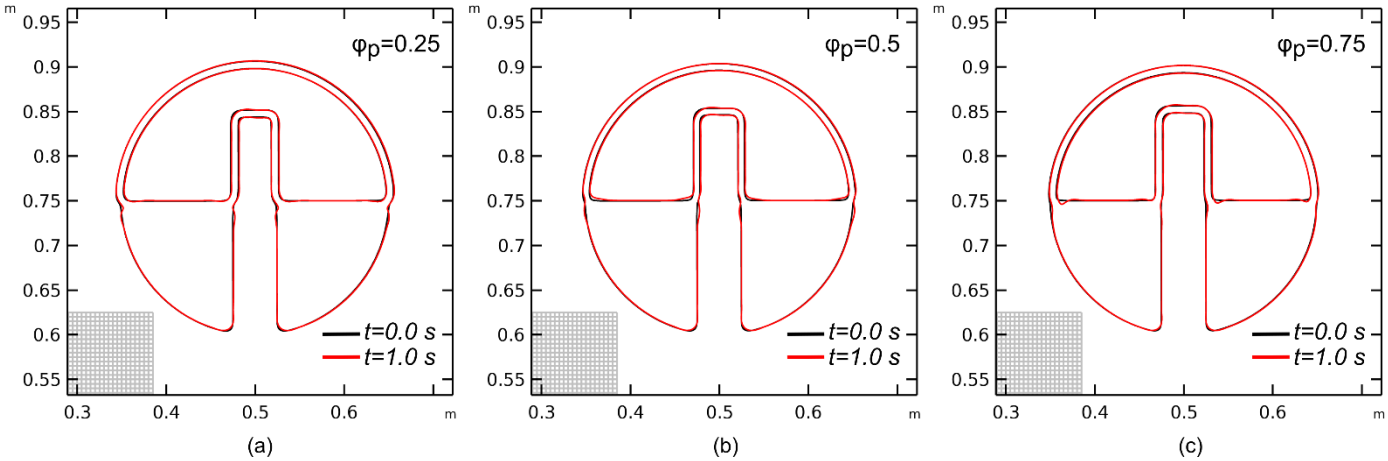

Figure 34. Comparison for the initial and final state of the ϕ-field for three phases Zalesak disc test after one revolution, 200×200 mesh; a) ϕ_P=0.25, contours indicate ϕ=0.125 and ϕ=0.625; b) ϕ_P=0.5, contours indicate ϕ=0.25 and ϕ=0.75; c) ϕ_P=0.75, contours indicate ϕ=0.375 and ϕ=0.875.

3.5.3 Falling Drop

So far, only the stability and accurate translation of the interface were assessed in the two prior experiments. This was done using a convective transport term that relies on a constant divergence-free velocity field generated by solid body rotation. A third experiment is conducted to demonstrate the densification of the powder phase into a solid phase. In this experiment, a circular disc with a radius of 0.15 and a powder density of ϕ_P=0.5 collides and merges with a solid wall with a density of ϕ=1 located

in the lower half of the area. A vertical downward velocity field is used to move the circular object towards the solidified wall, with the goal of causing the item to merge with the wall and become denser. The situation is purely theoretical and does not relate to a physical process. However, it does have an analytical solution, since we may see it as a vertical projection of the distributed function onto a horizontal surface. Applying a purely vertical projection will cause the circle to condense into a dome form that is either semi-circular (ϕ_P=0.5) or semi-elliptical (for all other values of ϕ_P). This dome shape will be deposited on top of the original flat surface.

In this model, the velocity field is no longer static but is determined based on the current level set solution. As a result, it will be transient and no longer satisfy the condition of being divergence free. Indeed, the existence of divergence is typically the primary factor responsible for the intended densification effect. The velocity is specified such that a uniform "drop velocity" only exists in the top half of the region. However, in order to prevent the density from increasing to levels greater than $\phi > 1$, which is not physically acceptable, the convective velocity is disabled as the ϕ-level approaches unity, as indicated by

$$\vec{v}(\phi) = \begin{bmatrix} 0 \\ -\big(1 - 1.04 H_s(\phi - 0.935, 0.1)\big) \end{bmatrix} \tag{29}$$

H_s is defined according to equation (24). Figure 35 illustrates the collision of the circular item with the solid surface, resulting in its densification into a semi-circular dome form. However, there is some smoothing at the areas where the flat surface transitions into the semi-circle, which should ideally maintain sharp, square-edged corners according to theory. The phenomenon appearing like surface tension causing the smoothing of sharp edges was also noticed in previous case studies, although it seems to be considerably more pronounced in this particular instance. It is contended that the extra rounding is a result of the horizontal flux component at various stages of the process, which is created by the reinitialization flux term that combines the diffusive and anti-diffusive components.

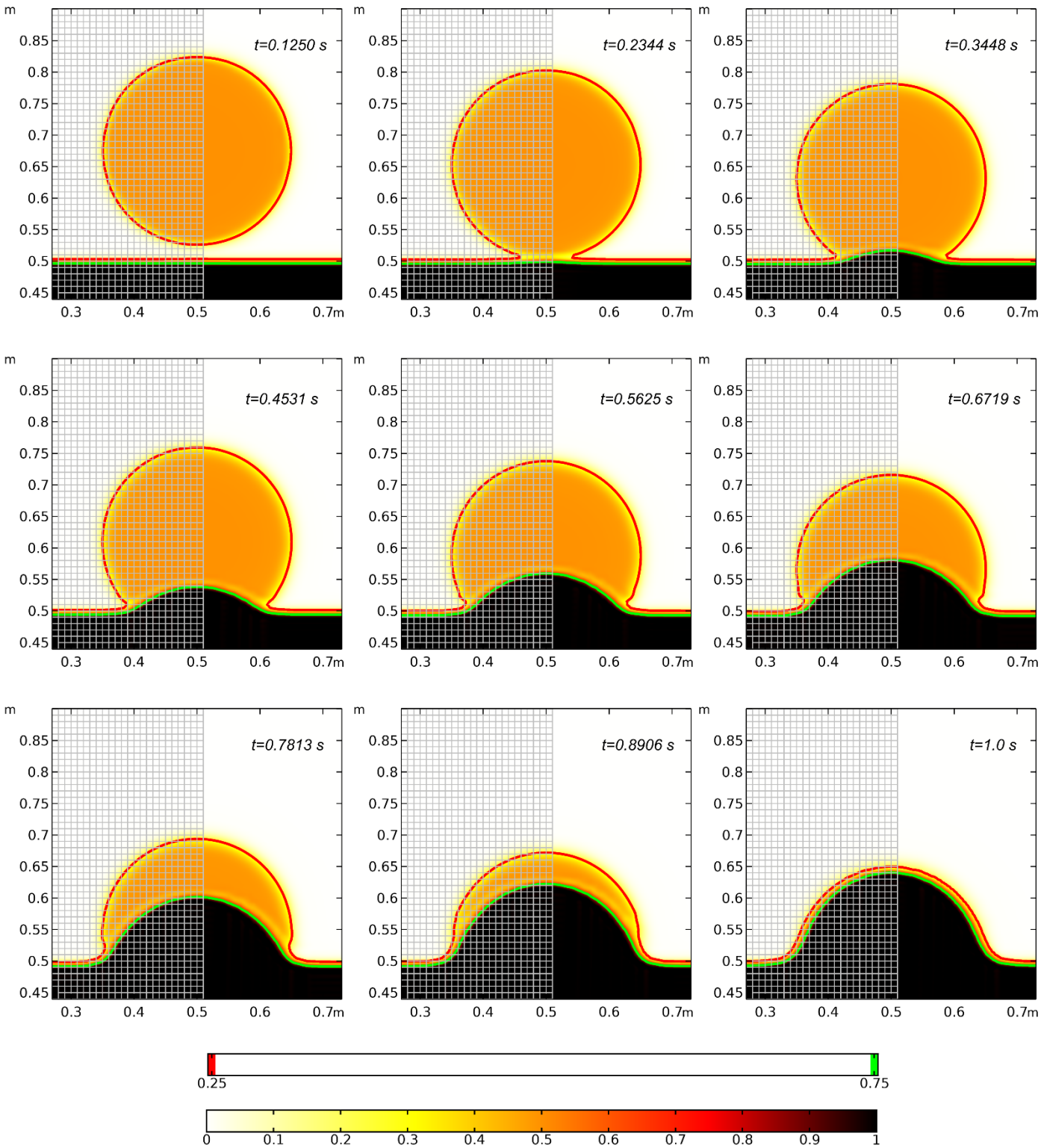

Figure 35. Densification of an intermediate phase, falling drop case.

3.5.4 Powder Bed Densification

The fourth case study explains the densification of a powder layer and might be regarded a test case for a powder bed fusion process. It also describes the technology's potential applications. A velocity field that is comparable to the one of the Falling Drop is applied to a powder/substrate base. The difference in the velocity lies in that this powder bed densification case is multiplied by an artificial term in order to induce a localized densification that occurs downwards from the top of the powder bed. This results in an expression that is dependent on both location and time, and it is defined as follows:

$$\vec{v}(\phi,\vec{x},t) = \begin{bmatrix} 0 \\ -\left(1 - 1.04H_s(\phi - 0.935,0.1)\right) \end{bmatrix} \cdot H_s\left(0.15 - \sqrt{(x-0.5)^2 + (y+t-0.8)^2}, 2\varepsilon\right) \quad (30)$$

The additional factor represents the thermal and fusion effects of the real process, the effects of which are here represented as a circular zone with a 0.15 spot radius that translates from above downwards to below the solid surface.

The initial condition has three layers, which depict a layer of powder on top of a solidified plate. In the next stages, the velocity field applied as specified in equation (30) will result in a localized increase in density inside the layer of powder. The case was successfully resolved for all element types and mesh quality. A comparison of the results obtained from different meshes is presented in Figure 36, which demonstrates that the results are very consistent across all meshes. Notably, Figure 36 (c) achieves the same outcome with just one-third of the CPU time required (refer to Table 3).

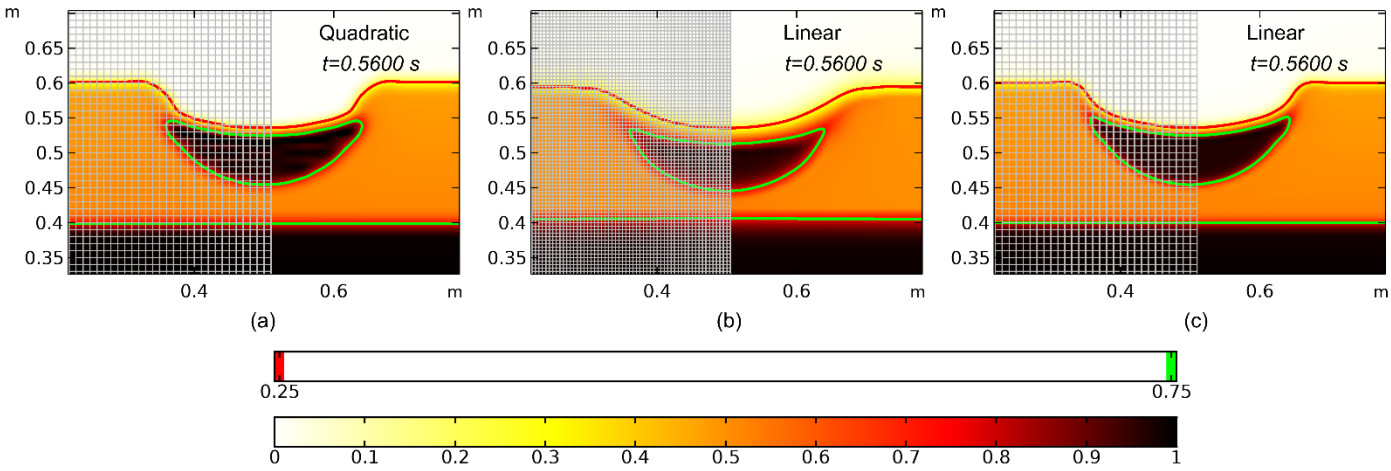

Figure 36. Densification of an intermediate level, case IV, at t=0.56 s*, for different mesh and element type (a) quadratic 100×100, (b) lineal 200×200 (c) lineal 100×100., The mesh is shown in the left part of the image.*

Figure 37 displays a comprehensive time history of the densification process for the coarse linear element mesh. Here, one can observe the formation of a compacted layer between the gas around it and the layer of powder. Following the initial formation, the compaction of the powder layer intensifies due to the gradual movement of the velocity field until all the powder is utilized, resulting in the creation of a solid and compressed layer track. By doing a brief examination, we can confirm that the thickness of the newly formed solid layer matches the anticipated thickness, considering that the density of the powder layer is half of the density after consolidation. Except for the thickness at the extremes, where the 'surface tension effect' causes the corners to become rounded, this statement is accurate.

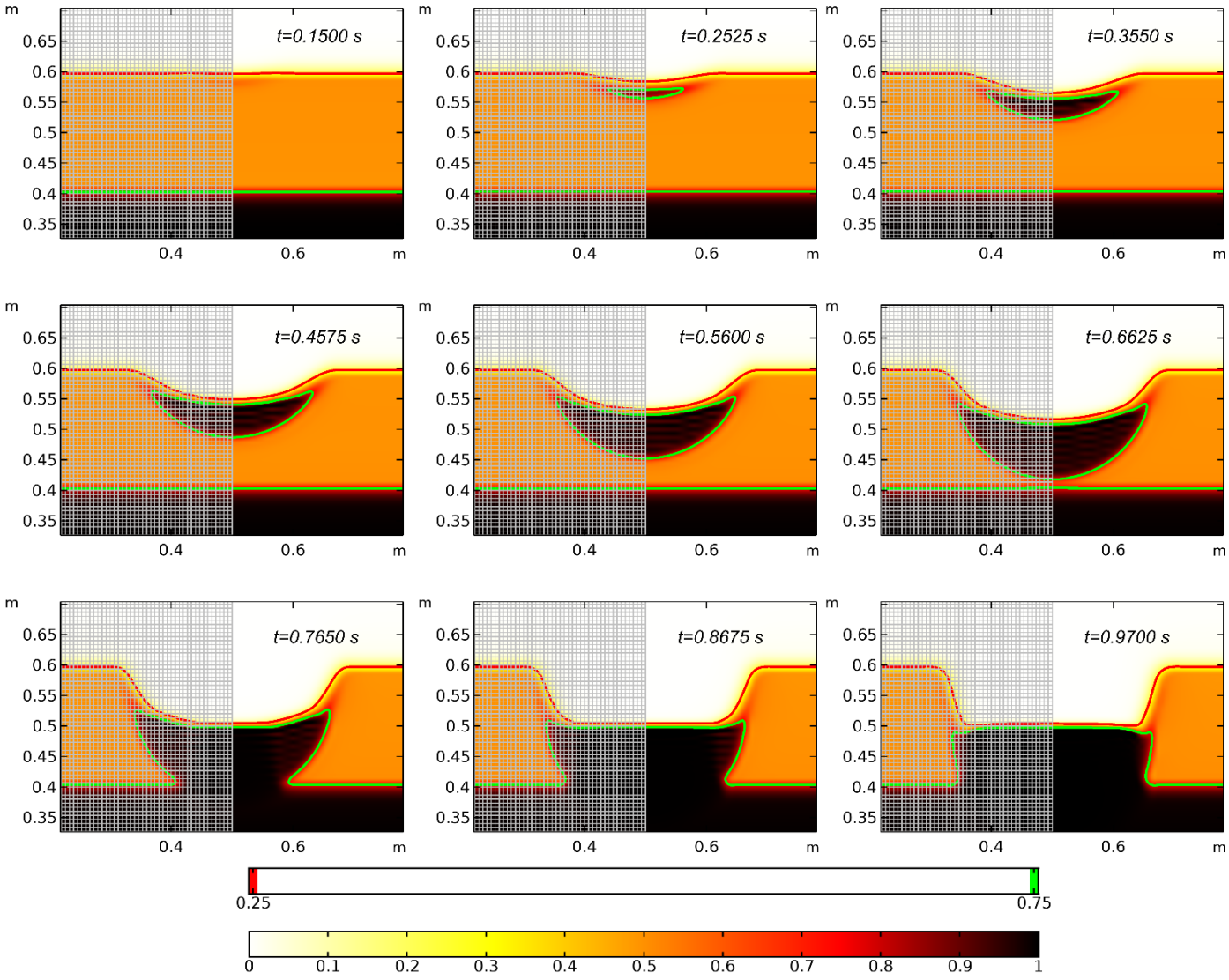

Figure 37. Densification of an intermediate level, case IV, showing the development over time, using 100×100 linear elements.

3.5.5 Discussion

The conservative nature of the formulation, which is based on equation (26), is confirmed by assessing the variation in total mass over a specified time period. The total mass is determined by calculating the integral of the conservative level set variable throughout the whole domain. Across all case studies, the discrepancies observed have a relative error of less than 10^{-5} and can be attributed to the FEM approximation approach and numerical truncation errors.

This model extends Olsson and Kreiss' CLS methodology [9] for a smooth interface transition between two “stable levels” or “phases” to three phases, such as void, powder, and consolidated or fully dense material. This enables for more efficient modeling of processes where the conservative level set variable may be directly related to the (effective) density value and mass conservation without adding significant computing cost that would be associated with an increase in degrees of freedom. The established technique offers these benefits, although several issues need more discussion.

Determining the switching function β is crucial for the approach and involves proper identification of the interface type. The anti-diffusion term is applied based on the value of β. Since the transition shape of the interface converges to the anti-diffusion term, any incorrect identification of the interface can self-amplify by pushing the transition towards an incorrect local gradient and shape, reinforcing previous mistakes. For the same reason, the approach demands that the gradients remain close to the anti-diffusion functions f_{VC} and f_{VPC}, respectively, and that the transitions be near the proper form from the start. The method is robust enough to allow sharp initial interfaces and converge to stable shapes. When ϕ is not near the ϕ_P level, an elevated value of β is assigned, and β decreases to zero only when the stable powder zone is detected.

The present switching function description works well and provides robust interfaces, however customization for individual models or meshes may be needed. In this study, $\varepsilon/h = 2\sqrt{2}$ is big enough to provide smooth transitions and accurate gradient magnitude measurement. Lower values and order elements might cause irregular transition shapes and impair gradient precision, resulting in less accurate interface type classification based on ϕ and its gradient. Additional criteria may be needed to determine the correct value of β and apply the appropriate anti-diffusion term. However, the fourth case showed that linear components with a coarse mesh relative to the transition thickness yield acceptable results at a lower computational cost.

Figure 23 shows the stability and distortion of contours around the triple point, another concern with this model. A beta definition that favors $\beta = 1$ might cause overshoot peaks at the interface, distorting it. However, when the preference is too low, the triple point moves toward the VC and separates it into two powder interfaces. Beta tuning depends on mesh or element type and is delicate. The proposed beta definition is a compromise where linear and quadratic elements arrive to similar solutions and the triple point behaves similarly.

The velocity fields proposed in the previous cases show the capacity for this model to represent the densification of a powder phase and the consequent growth of the consolidated phase. This effect is a consequence of the conservative characteristic of this approach that produces a source or sink term when a divergent (artificial) velocity field is applied, producing a density change, corresponding to the change of the level set variable ϕ at that location. Therefore, care must be taken to apply the correct restrictions, such as applied in the densification case studies III and IV where a restriction is imposed on the velocity field by reducing the velocity to zero when $\phi = 1$. Since these types of relations turn the numerical model in non-linear models, it is preferable to implement the restrictions in a smooth way, both in order to facilitate the numerical solver, as to avoid the excessively high and strongly localized divergence terms and therefore large source terms, which may distort the transition at the interface and render the method unstable. The restriction should avoid occurrence of unrealistic density at more than 100% of the consolidated density.

In current models, compacting convective velocity fields may represent the gravity field or an initial powder velocity as justification, but each model should have a physics-based velocity field that describes physical behavior as realistically as possible. If the model has such information, it may resolve and apply a fluid dynamic model-based flow velocity field.

Since just one LS equation is employed, the suggested technique solely tracks conservation of one material ingredient. The multi-level approach should not be used with more than one material if mass conservation is sought for each phase. All LS formulations have this constraint, therefore if additional chemicals are involved, a cautious level set equation must be solved for each preserved ingredient. The presented method should only be used when the three stable levels represent three typical density states of the same substance, such as in the homogenized density model for powder bed processes in additive manufacturing, where the intermediate level set value represents the powder phase.

While in this chapter the presented concept and examples are confined to three levels, this model could be expanded to include more stable levels that reflect different states of the same material. The expansion follows the concept from previous sections but requires additional interface types and anti-diffusive gradient functions f in $\nabla\phi - \phi$ space.

The direct relevance of the level set variable as the effective density makes the technique solid and clear, notwithstanding the prior findings of potential faults or sensitivities. Compared to the two-equation level set variable approach, it should be computationally efficient. This alternate model has not been applied for the offered case studies and would require careful coupling term definition between the two level set equations to ensure mass conservation and accurate densification. Although a precise computational advantage cannot be calculated, the proposed method uses half the degrees of freedom, which undoubtedly significantly reduces both the memory usage and the CPU time needed to solve the set of equations, especially when using an implicit solver.

Case studies III and IV show that the proposed HDM methodology can be used to model powder-based additive manufacturing processes like powder bed fusion, where the level set variable tracks the interface evolution of the consolidated part.

4 Modelling of Powder Bed Fusion Processes using the Multi-Density Level Set Method

Following the goal of this thesis, which is *to provide a time efficient model to better understand thermal processes in powder bed fusion process*, two main subtasks were developed in this research. The core of the first subtask, which is about developing a computational technique that can track the evolution of a multi-phase system using a single level set equation was developed in Chapter 3. Some of the capabilities of this approach were already tested and discussed in the same chapter.

In the following, the second subtask is discussed, in which the HMD model is extended and linked to mass conservation, and the thermal model is added. In Section 4.1 a detailed explanation about the model assumptions is given. Next, the mass conservation is discussed in Section 4.2. Finally, the development of a thermal model that works under the HMD framework is addressed in Section 4.3.

4.1 Multiphysics in Powder Bed Processes

As mentioned in the Chapter 2, the main challenges when modeling a PBF process are:

- Evolution of the interfaces.
- Multiphysics problem.
- Different time and space scales.

The first problem was already addressed in Chapter 3. The second aspect is going to be attended in this chapter.

PBF is a multi-physics problem since many different coupled interactions are present during the process. Although many mathematical approximations already exist to fully model all the known interactions in PBF by first principles, it is, in practice, impossible to simulate such a complete model with the current technology. That is why many simplified models have been proposed, and many of them rely on continuous approximations using differential equations. It is somehow possible to split all the interactions and phenomena by their ‘physics’. In Figure 38 the main physical phenomena that are present during PBF are shown. In this thesis the analysis is focused on keeping track of the evolving surfaces and heat transfer.

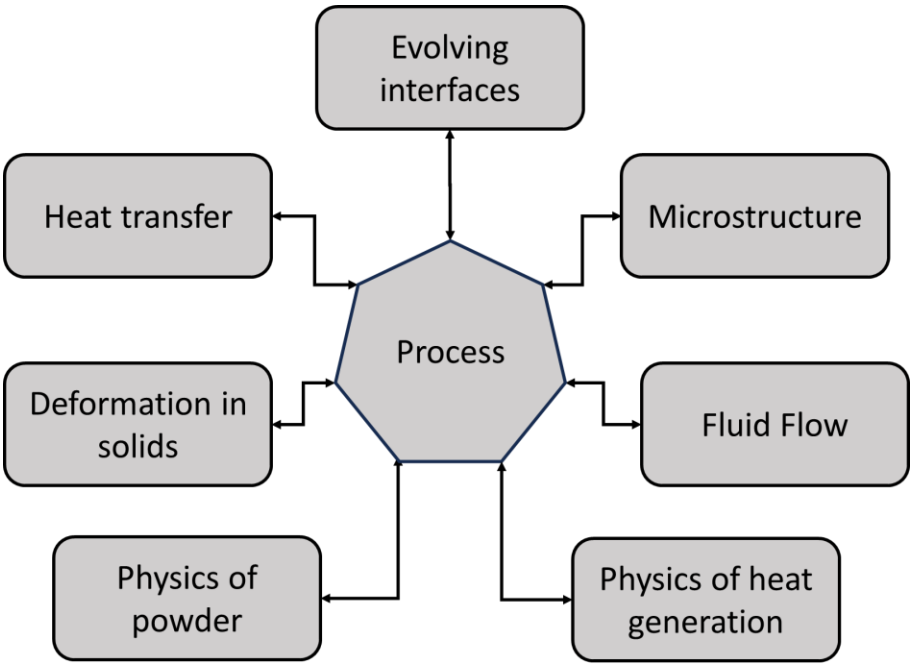

Figure 38. Different phenomena in PBF

To develop a reduced model the following assumptions are considered:

- Since the influence of deformation of the solid on the thermal balance is negligible, the deformation of the solid is not taken into account.
- It is assumed that the microstructure effects are not important in the thermal field, since the energy absorbed/released by solid-state phase transformations are small compared with the heat source energy.
- The flow of the fluid is considered in an implicit way by an imposed flow field that contains the net effect of the global fluid movement, which is a downwards movement that would allow a densification of the melted powder particles.
- The physics interaction between powder particles and heat source is simplified to a volumetric Beer-Lambert heat source model.
- The physics of granular material is simplified to a homogenized multi-density model.

In Figure 39 it is shown a summary of the assumptions considered in the current work

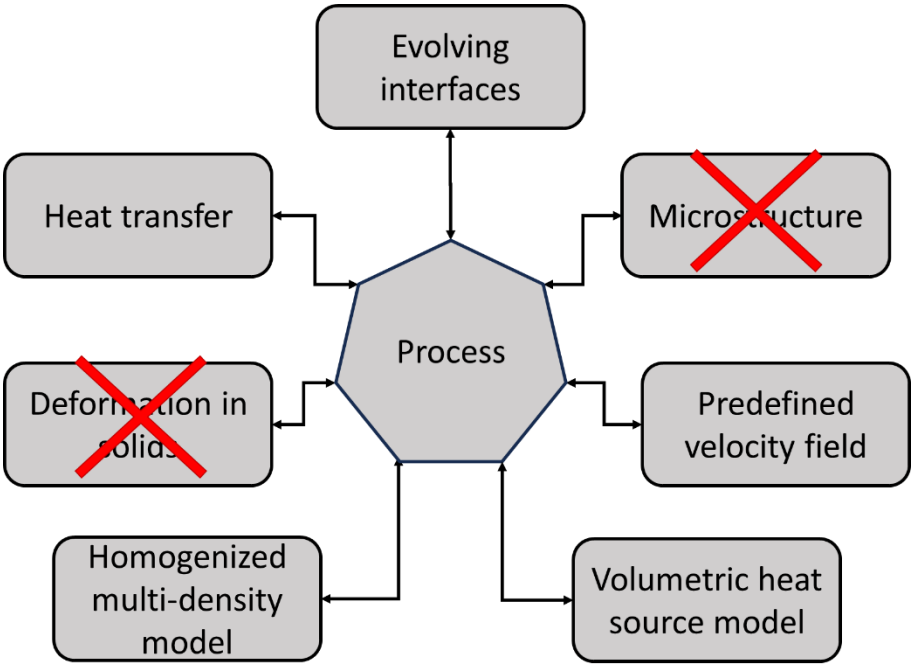

Figure 39. Simplifications in the proposed model.

4.2 Governing Equations

In the realm of physics and engineering, the laws of conservation allow the description and characterization of the systems' behavior. These conservative equations describe that some quantities remain constant throughout time. In this work the conservative equations are given in differential form within an Eulerian framework. Two main physics are considered: mass conservation and energy conservation. Conservation laws must be satisfied, and it is possible to write a general equation of conservation considering the different types of fluxes: fluxes due to diffusion ($\vec{J}$), fluxes due to advection ($\theta\vec{v}$), sources or sinks (g). The fundamental equation of conservation can then be written as:

$$\int \left[\frac{\partial \theta}{\partial t} + \nabla \cdot \left(\vec{J} + \theta\vec{v}\right) - g\right] dV = 0 \tag{31}$$

In the next sections the theoretical foundations of the conservative equations of mass and energy are given.

4.3 Mass Conservation Equation

In this model, the HMD model determines the corresponding material at each location inside the domain, and the conservation of mass is directly linked to the HMD model that defines a phase variable (Level Set) that goes from 0 (void material) to 1 (consolidated material; solid or liquid). However, as it was

mentioned before, this HMD can also represent an intermediate level/material that corresponds to the homogenized powder material. Nonetheless, only one species can be tracked, which can be present in a state of powder or as consolidated material. Although void is another material under this framework, conservation of void is not tracked. So, using (31) and assuming that the integration is performed over an arbitrary domain it is possible to write the mass conservation equation in terms of ρ as follows:

$$\frac{\partial \rho}{\partial t} + \nabla \cdot \left(\vec{J}_{mass} + \rho \vec{v}\right) = \dot{s}_{mass} \tag{32}$$

Where ρ is the effective density of the material, $\vec{J}_{mass}$ is the mass flux produced by diffusion, and $\vec{v}$ is the velocity field, and $\dot{s}_{mass}$ is a volumetric mass source.

From (26) and replacing the definition of the normal already mentioned in Section 3.4 while multiplying by the conserved quantity ρ_C

$$\rho_C \left(\frac{\partial \phi}{\partial t} + \nabla \cdot \left(-\gamma \left(\varepsilon - \frac{\beta f_{VC}}{\|\nabla \phi\|} - \frac{(1-\beta) f_{VPC}}{\|\nabla \phi\|} \right) \nabla \phi + \vec{v} \phi \right) \right) = 0 \tag{33}$$

Defining $\vec{J}_{mass}$, that accounts for the diffusive and anti-diffusive mass fluxes.

$$\vec{J}_{mass} = -\rho_C \, \gamma \left(\varepsilon - \frac{\beta f_{VC}}{\|\nabla \phi\|} - \frac{(1-\beta) f_{VPC}}{\|\nabla \phi\|} \right) \nabla \phi \tag{34}$$

Defining a density as function of the level set as $\rho_m(\phi) = \rho_C \phi$, where ρ_C is the density of the consolidated material.

Then, the mass conservation equation in terms of the level set variable can be written as equation (35), where $\dot{s}_{mass}$ accounts for the source terms of mass rate

$$\rho_C \frac{\partial \phi}{\partial t} + \nabla \cdot \left(\vec{J}_{mass} + \rho_C \phi \vec{v}\right) = \dot{s}_{mass} \tag{35}$$

After one quick comparison it is possible to verify that equation (26) becomes the mass conservation equation.

The term $\dot{s}_{mass}$ is added to account for the powder addition. This term allows for addition of extra material that is not present at the beginning, which will be used to describe the deposition of the new powder layers on the previous layers of the powder bed.

4.4 Energy Conservation

Like mass, energy must also be conserved under the level set formulation. Considering (31), the energy conservation law can be stated as

$$\frac{\partial}{\partial t}\left(\frac{1}{2}\rho v^2 + \rho u\right) + \nabla \cdot \left(\vec{q} + \left(\frac{1}{2}\rho v^2 + \rho u\right)\vec{v}\right) - \dot{s}_{ext,heat} = 0 \tag{36}$$

For the energy equation it is important to identify the most important contributions to the system. The kinetic energy $\frac{1}{2}\rho v^2$ is very small to the external energy $\dot{s}_{ext,heat}$, so it can be neglected. The internal energy, u, can then be substituted by $u = h - pv$, where the pv term can also be neglected, since pressure difference is not considered. Thus, energy conservation can be replaced by an enthalpy conservation as follows:

$$\frac{\partial}{\partial t}(\rho h) + \nabla \cdot \left(\vec{J}_{heat} + \rho h\vec{v}\right) = \dot{s}_{ext,heat} \tag{37}$$

Here $\vec{J}_{heat}$ accounts for the diffusive fluxes, the first contribution is diffusion of energy by conduction mechanism, which is defined by Fourier law $\vec{q}_{cond} = -k\nabla T$. Under the well-known heat transfer model, conduction is the only mechanism by which energy is diffused. However, under this framework, another diffusive flux is also present. This heat flux comes from the diffusion of mass in the mass conservation law in (35). So, this heat flux due to mass diffusion can be written as $\vec{q}_{mass} = h\vec{J}_{mass}$. The proposed equation for conservation of energy can be stated as

$$\frac{\partial}{\partial t}(\rho h) + \nabla \cdot \left(-k\nabla T + h\vec{J}_{mass} + \rho h\vec{v}\right) = \dot{s}_{ext,heat} \tag{38}$$

where $\dot{s}_{heat}$ accounts for the volumetric heat source that will be explained in the following sections.

Although expression (38) can be implemented, it is rewritten obtaining the following expression:

$$\rho\frac{\partial h}{\partial t}+\nabla\cdot(-k\nabla T)+\nabla h\cdot\left(\rho\vec{v}+\vec{J}_{mass}\right)+h\left(\frac{\partial \rho}{\partial t}+\nabla\cdot\left(\rho\vec{v}\ +\vec{J}_{mass}\right)\right)=\dot{s}_{ext,heat} \tag{39}$$

Where the last term in left hand side in (39) is the left-hand side in (32). Thus, the following equation that already involves the mass conservation equation can be written as

$$\rho\frac{\partial h}{\partial t}+\nabla\cdot(-k\nabla T)+\nabla h\cdot\left(\rho\vec{v}+\vec{J}_{mass}\right)+h\dot{s}_{mass}=\dot{s}_{ext,heat} \tag{40}$$

One important remark is that the variable h represents the total enthalpy (energy) in the process. Total enthalpy can then be decomposed as $h=h_s+\Delta H$. In which h_s is the sensible enthalpy and ΔH is the latent heat that can be calculated as: $\Delta H=L_m H_s(T-T_m)$, being L_m the latent heat of fusion. H_s is the smoothed Heaviside function defined in Chapter 3, and T_m is the temperature of fusion. Another important term to be considered is the temperature in the conduction term that can be written in terms of enthalpy by the following definition: $\mathrm{d}h=C_p\mathrm{d}T$. Thus, rearranging (40) and replacing the aforementioned definitions it is possible to get:

$$\rho\frac{\partial h}{\partial t}+\nabla\cdot\left(-\frac{k}{C_p}\nabla h\right)=\dot{s}_{ext,heat}-\nabla h\cdot\left(\rho\vec{v}+\vec{J}_{mass}\right)-h\dot{s}_{mass} \tag{41}$$

The final consideration is about the last term on the right-hand side of the equation (41), which cancels the energy in the phase/level transformation when a layer of powder is added to the system at the current enthalpy. This term preserves the total energy when adding a layer of powder at the current enthalpy. Thus, to account energy added by an external source e.g., powder at room temperature, an extra term needs to be added. The enthalpy/energy of powder at room temperature can be written as: $h_{powder}\dot{s}_{mass}$. Then the final expression is implemented in Comsol Multphysics®.

$$\rho\frac{\partial h}{\partial t}+\nabla\cdot\left(-\frac{k}{C_p}\nabla h\right)=\dot{s}_{ext,heat}-\nabla h\cdot\left(\rho\vec{v}+\vec{J}_{mass}\right)+(h_{powder}-h)\dot{s}_{mass} \tag{42}$$

Equations (35) and (42) were solved over rectangular domains that represent a cross section of a prismatic domain

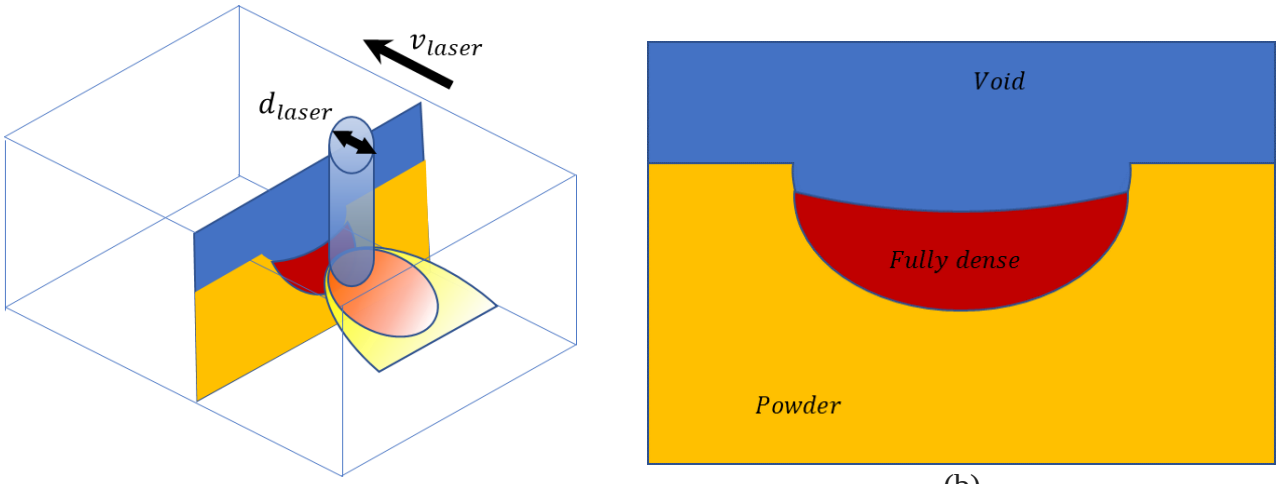

Figure 40. Cross section on which the conservation equations are solved, (a) 3-D domain, (b) 2-D cross-section domain.

4.5 Boundary Conditions

In addition to the domain equations (35) and (42) boundary conditions are necessary to solve the system equations. However, the surfaces in the presented model continuously evolve, making the surface an unknown, see Figure 41. The HMD model that has been introduced in Chapter 3, captures the evolving surface inside the domain, which means that the surfaces are embedded inside the domain, at varying position. This requires that the boundary conditions over the interface surfaces are transformed from boundary conditions into volumetric sources/sinks within the domain. This applies to both mass and energy boundary conditions. Therefore, the $\dot{s}_{mass}$ and $\dot{s}_{heat}$ source terms contain the boundary conditions of the free surface problem.

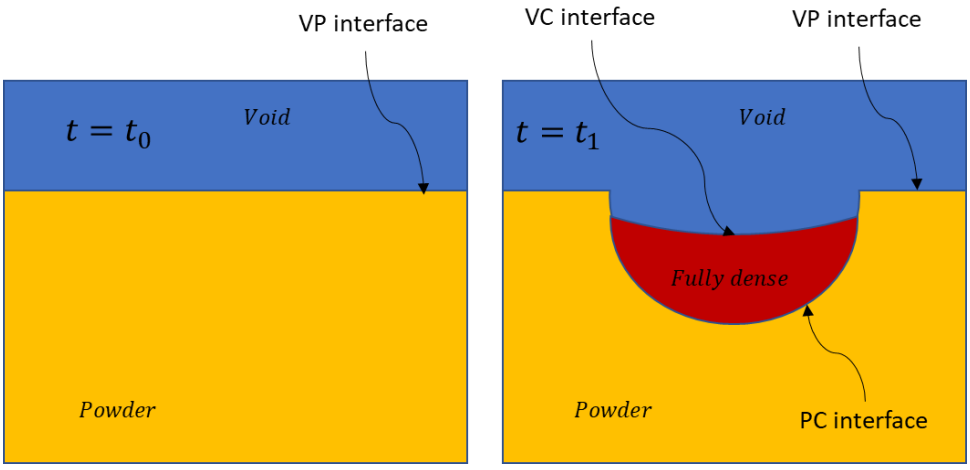

Figure 41. Sketch for the expected interfaces in the HMD.

4.5.1 Transformation of Boundary Conditions to Sources for Mass Conservation Equation

The evolving melt pool and all the interfaces around it need boundary conditions, since there is mass crossing these boundaries VC and PC. However, boundary conditions need to be applied over an existing boundary, and as can be seen in Figure 41a, no melt pool appears, while in Figure 41b there is a melt pool. To set these boundary conditions over an evolving or non-existing interface in sharp interfaces methods and even for capturing methods such as traditional Level Set becomes a big challenge, that is usually solved with cumbersome restrictions to prevent overlaps between the two-level set (at least) variables. In addition to the mass transfer between boundaries and the phase/level transformation once powder becomes consolidated material. However, for the HMD method applying boundary conditions for mass conservation is not a problem, since the actual boundary conditions are already embedded in the model. The term that accounts for this mass transfer through boundaries is $\vec{J}_{mass}$ that is responsible to adjust the fluxes according to the diffusive and anti-diffusive terms.

Another important boundary condition that is present is when extra powder is added to the system. This happens when a new layer of powder is added, see Figure 42. Figure 42a and Figure 42b show an intermediate and final stage in the process of powder addition. Here, external material is added to the system and the VP moves upwards. The term that accounts for this material addition is the $\dot{s}_{mass}$ term, that is implemented as a source term.

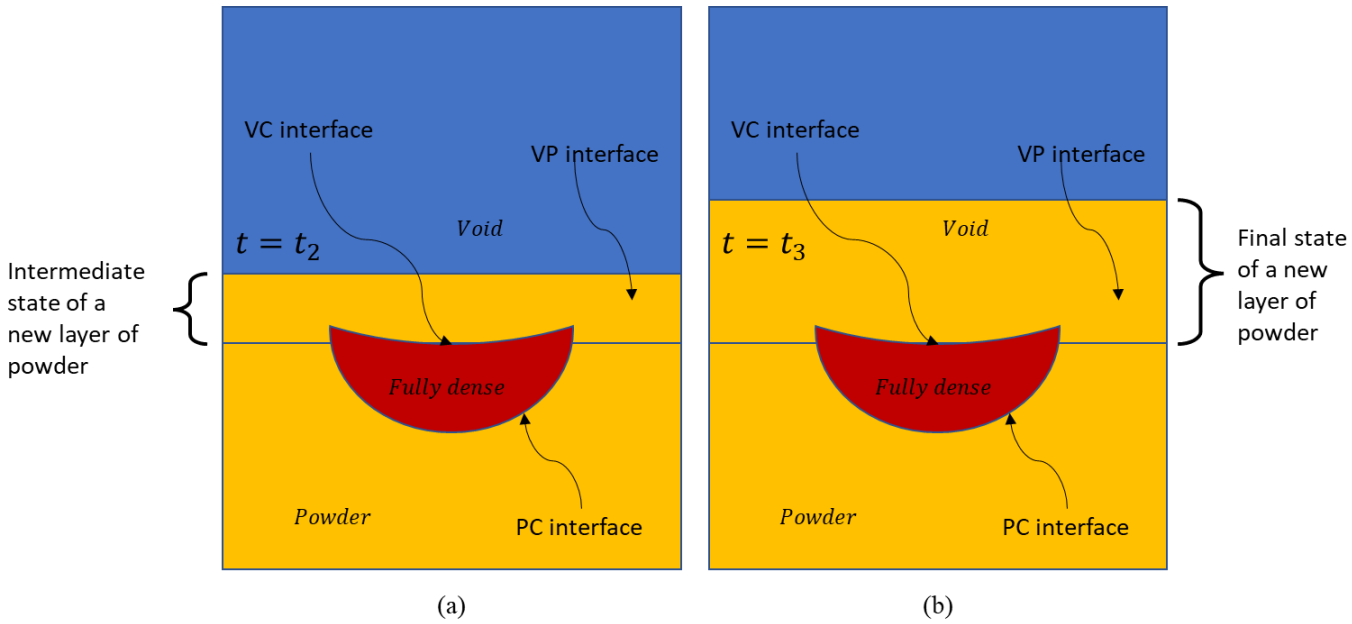

Figure 42. Sketch of the deposition of a new layer of powder

The $\dot{s}_{mass}$ term creates material at a constant rate over certain region. Expression (43) shows how can this term be approximated.

$$\dot{s}_{mass} = c_{layer}(\phi_P - \phi) \cdot H_s(z - z_L, \varepsilon) \tag{43}$$

where ϕ_P is the relative density of powder, c_{layer} is a coefficient that defines how fast the powder layer is delivered, and H_s is the smooth Heaviside function, where z is the vertical coordinate and z_L is the top of new powder layer and ε is the transition zone.. In Figure 43, the evolution of powder layer creation is plot. Here, it is possible to appreciate how a new layer is applied on top of a previous powder layer that in turn is positioned over the base material.

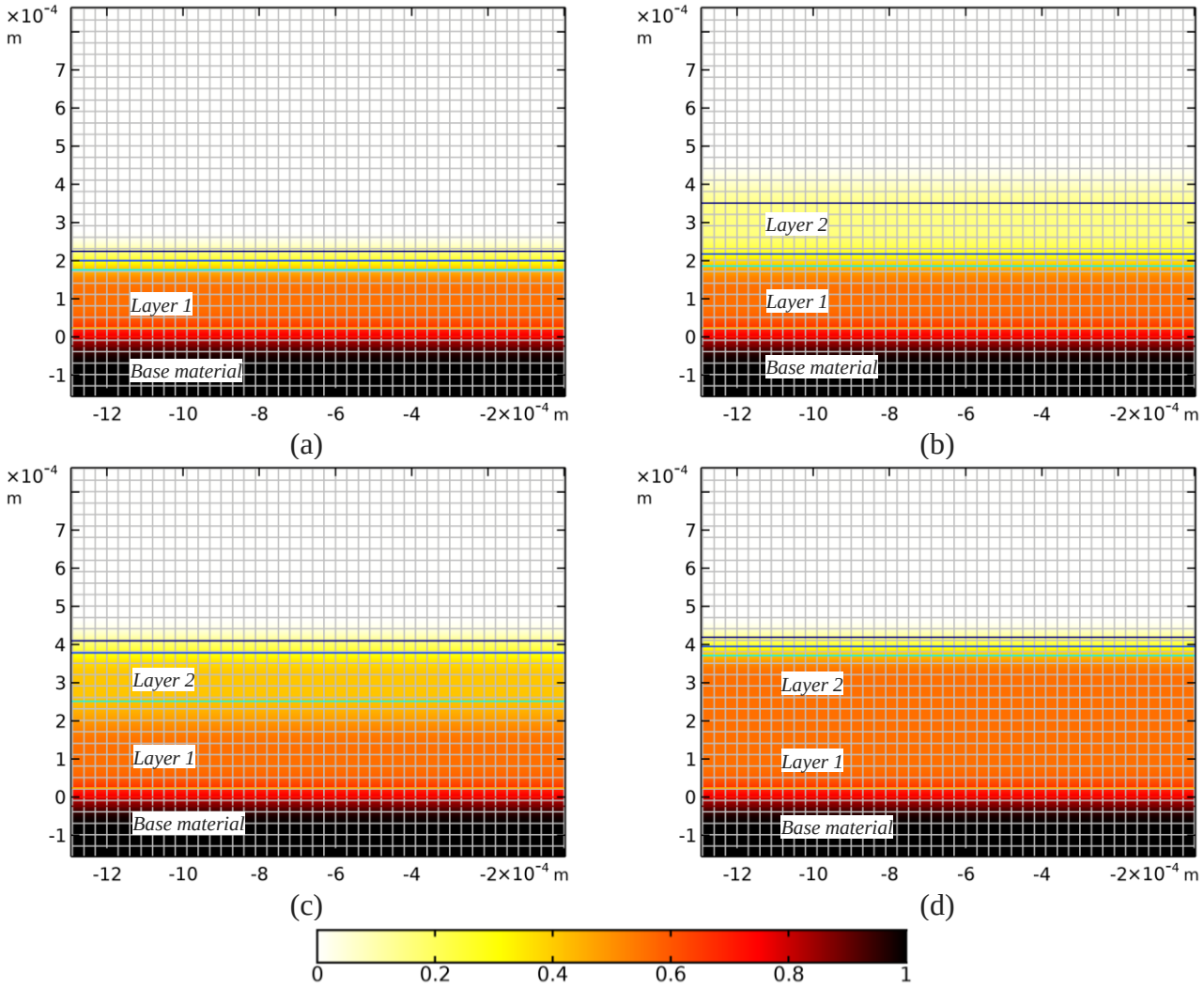

Figure 43. Addition of a layer of powder, (a) initial state, from (b) to (d) evolution to final state.

4.5.2 Mass Conservation Equation

In addition to the physical boundary conditions that became sources within the level set formulation, boundary conditions are still needed to completely define the level set problem. To fully define the boundary conditions in the level set problem, a rectangular domain is chosen (although any other shape can be used) for all the simulation cases. Under this rectangular domain a zero flux of mass is imposed over the boundaries as can be seen in Figure 44b. It is important to mention that mass conservation (level set) is not solved over the whole domain but only where interface is evolving. Since in many real case scenarios, fusion of the material only occurs in a small region compared to the full domain, only in a small domain the mass conservation is solved. In Figure 44a a typical domain that is simulated is shown and only at the small indicated region the mass conservation is solved (Equation (35)).

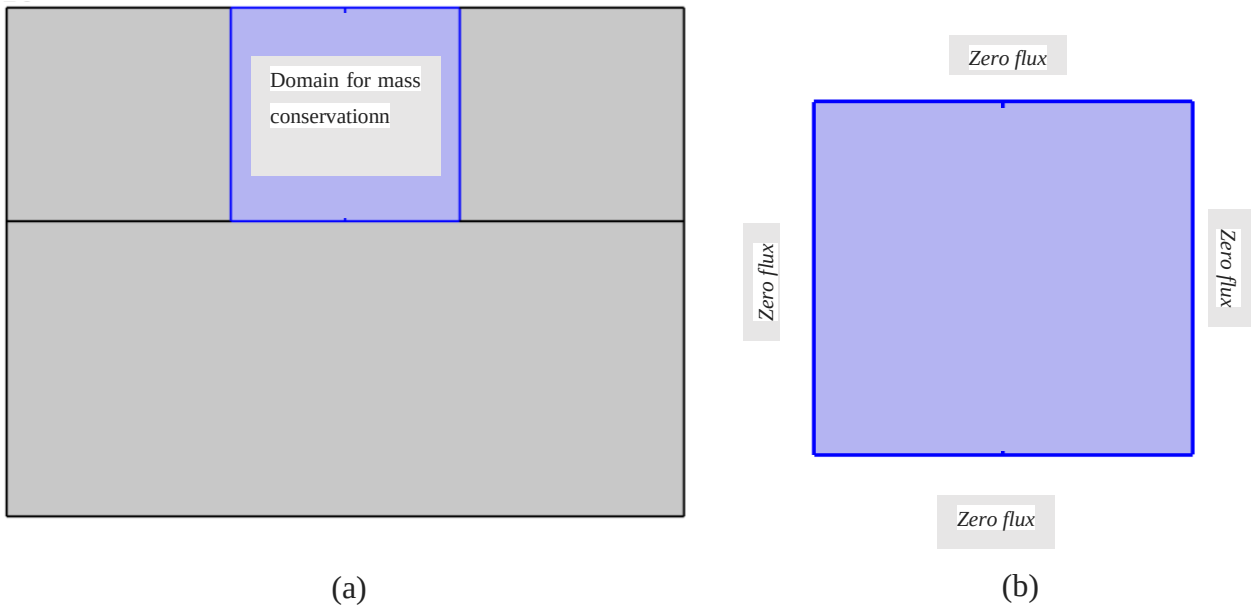

Figure 44. PBF domain: (a) Level set domain in blue (domain for heat transfer is in gray), and (b) boundary conditions for the mass conservation equation.

4.5.3 Transformation of Boundary Conditions for Energy Conservation Equation

For the boundary conditions for the heat transfer physics also some transformations are required. First of all, only two types of inputs/outputs of energy are considered. One is the heat source addition by the laser beam or electron beam, which both are assumed to have similar distributions. The other type is the heat loss by convection and radiation. The first tends to be more important in the cooling stage while the second tends to be more important during heating. A sketch in which the heat input as well as the heat output (heat losses) is shown in Figure 45. Although, a Gaussian distribution is shown, the methodology applies

to any other type of distribution. At the VP, where the heat input/output is applied, energy conservation must be accomplished. In Equation (44) it is shown the energy balance of the free boundary.

$$\vec{q}_{ext,heat} \cdot \vec{n} = (\vec{q}_{in} - \vec{q}_{out}) \cdot \vec{n} = -\frac{k}{C_p} \nabla h \cdot \vec{n} \tag{44}$$

Where $\vec{q}_{in}$ is the external heat added by the energy beam, and $\vec{q}_{out}$ is the external heat removed by convection, $h_{conv}(T_\infty - T)$, and radiation $h_{rad}(T_\infty^4 - T^4)$. To transform these boundary conditions to the smooth interface, the definition of normal can be applied $\vec{n} = \frac{\nabla \phi}{\|\nabla \phi\|}$. With this definition it is possible to define a heat source that follows the moving interface whose position is continuously calculated during the simulation. The length in which the heat is distributed is: $1/\|\nabla \phi\|$, then the volumetric heat source is $\dot{s}_{ext,heat} = (\vec{q}_{ext,heat} \cdot \vec{n})\|\nabla \phi\|$. The boundary condition is then transformed into a heat source that can then be written as it is shown in Equation (45).

$$\dot{s}_{ext,heat} = \left(\vec{q}_{ext,heat} \cdot \vec{n}\right)\|\nabla \phi\| = (\vec{q}_{in} \cdot \vec{n})\|\nabla \phi\| + h_{conv}(T_\infty - T)\|\nabla \phi\| + h_{rad}(T_\infty^4 - T^4)\|\nabla \phi\| \tag{45}$$

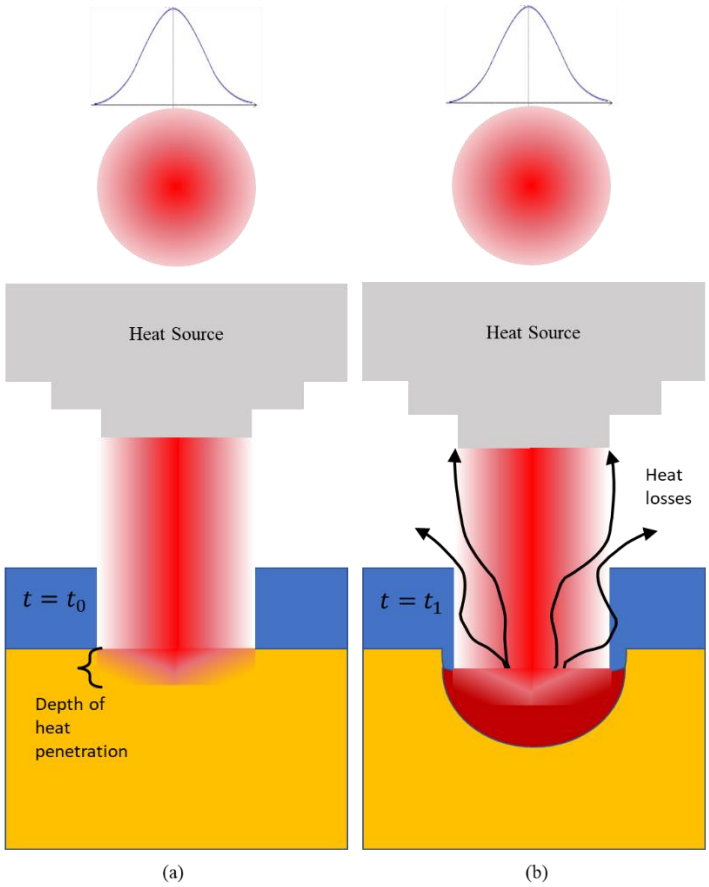

Figure 45. Sketch for the heat source when heating the powder.

Previous implementations of this method shown that this method only works fine when the transition zone goes from 0 to 1, which is only the case when the beam interact with a VC interface. But when the interaction is with a powder interface, usually a VP interface, the level set goes from 0 to the intermediate relative density powder value $\phi_P \approx 0.6$. In that case, the added energy is not going to be the 100% of what is desired, instead only a part of it will be added, which corresponds to the same percentage of powder density ($\phi_P \approx 0.6 = 60\%$) of the total energy. This is an important issue to be considered. Although the solution for the heat losses outside the LS domain can easily be compensated by simply dividing by ϕ_P. This is not the case for the domain where LS is solved, either for heat losses or the energy added by the beam. The overall energy would result in less than specified. The most important consequence would be that the melt front could never start because of the lack of energy. Although, division by ϕ_P, as it is proposed by heat losses outside the LS domain, might help at the initiation of the consolidated material, once the melt pool is initiated an extra energy would be added. Thus, a correction factor that depends on ϕ is required. Nonetheless, a more suitable definition that avoids that correction factor and while improving the control of penetration depth is developed and is fully explained in the next section.

4.5.3.1 Heat Source (Beer-Lambert Law)

In the previous section a methodology to develop a volumetric external heat source was addressed. However, at the beginning the heat is applied over a void-powder interface that would lead to a lower energy application that desired. Although it is possible to fix this issue, another model is proposed and implemented.

The volumetric heat source is a better option since the penetration depth can be controlled, something impossible in the previous heat source model. In the proposed heat source model, the heat source is determined by the Beer-Lambert law, that describes the intensity decay of an energy beam when passing through an absorbing medium. This method has been widely implemented and it was already commented in Chapter 2, however, in such cases the interface was fixed at a known position and represented as a discrete transition, in which case an explicit solution to the Beer-Lambert equation is possible. In the proposed model the interface is varying continuously and described by the continuous level set variable. So, the Beer-Lambert equation needs to be calculated at every time step of the simulation along with the energy and mass conservation equations. In order to set the Beer-Lambert equation, a multiplicative decomposition of the source term $\dot{s}_{in}$ is defined in Equation (46). Where P_0 is the magnitude of the total

absorbed beam power. $I_{\vec{r}}(\vec{r},t)$ is the radial Gaussian distribution over the cross section of the beam (see equation (9)), and $I_z(z,t)$ is the unit variable to be solved and is the local intensity fraction along the heat source axis (denoted here as the z-axis), whose direction in this work is considered to be perpendicular to the powder bed, although it could be set in different orientations. This multiplicative decomposition allows the problem to reduce to the solution of the intensity fraction as it is shown in (47), in which α can be considered as the absorption coefficient, and as such describes the opacity of the material, and is considered to depend on ϕ. The value of α is inversely proportional to the penetration depth.

$$\dot{s}_{in} = P_0 I_{\vec{r}}(\vec{r},t) I_z(z,t) \tag{46}$$

$$\frac{dI_z(z,t)}{dz} = -\alpha(\phi) I_z(z,t) \tag{47}$$

where $\alpha(\phi)$ then depends on the interface location and varies at a every time step. The proposed function for $\alpha(\phi)$ is shown in (48), in which S is the penetration depth. This relation allows the use of the same ϕ-field assigning a zero opacity to the void region while a maximum opacity at consolidated region. Some results about the penetration depth of this function are shown in Figure 46. In this figure, the scaled heat source $\dot{s}_{in}/P_0$ is plot for several values of $S = \{\varepsilon/4, \varepsilon/2, \varepsilon, 2\varepsilon\}$.

$$\alpha(\phi) = \frac{\phi}{S} \tag{48}$$

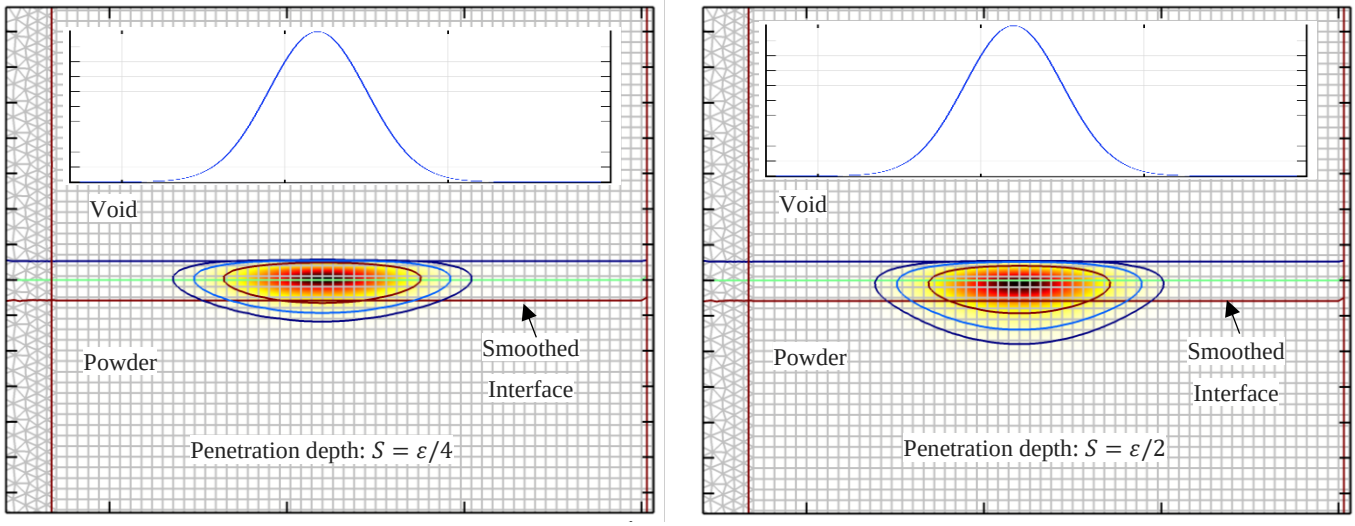

(a) (b)

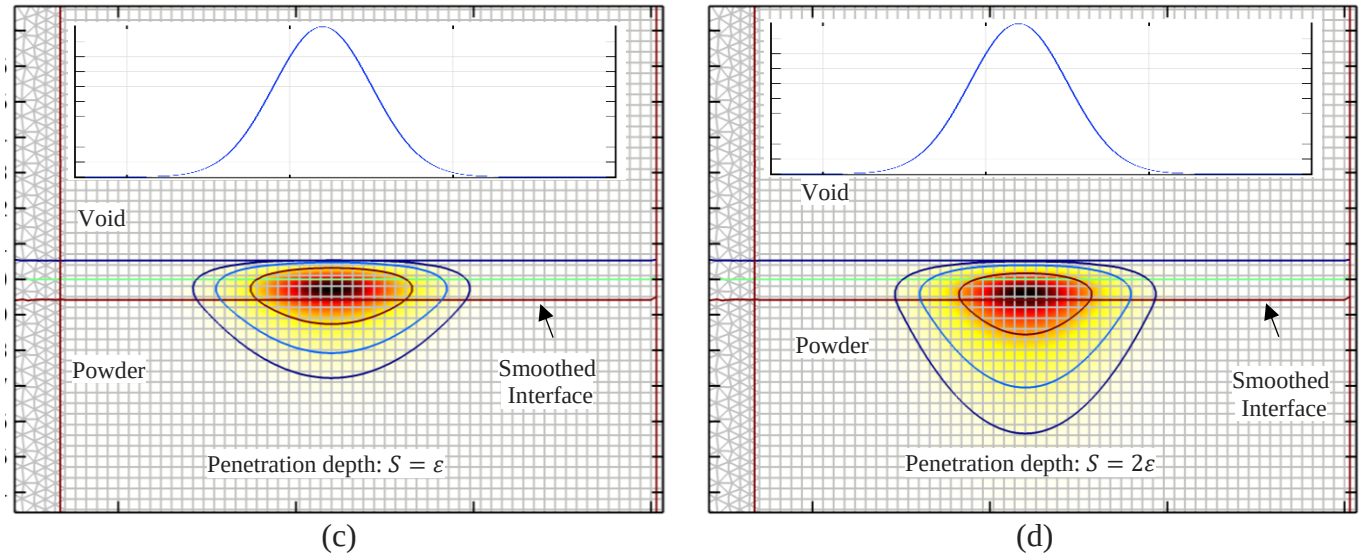

Figure 46. Scaled heat source $\dot{s}_{in}/P_0$. The contours show the intensity value at 50%, 63% and 85% respectively.

A plot along the beam axis is plot in Figure 47. Although in a physical process the penetration depth can be determined by experimentation, as well as with a ray tracing simulation. In this thesis, the criteria to determine the penetration depth was the smoothness of α-field, since the real penetration depth could in some cases be too small, which can result in a lack of convergence. For the following sections the chosen penetration depth was set as: $S = \varepsilon$.

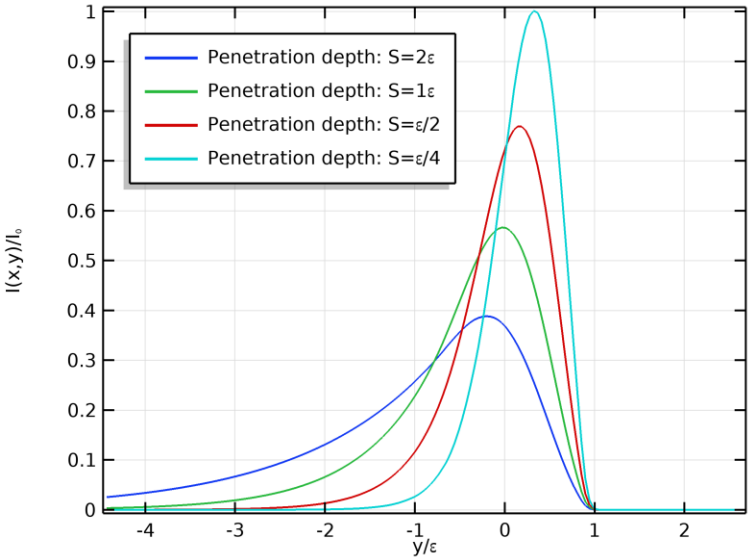

Figure 47. Heat distribution for several penetration depths factors.

4.5.4 Energy Boundary Equations

In addition to the physical boundary conditions at the interface boundary that were transformed into heat sources under the level set framework, boundary conditions are still needed at the limits of the computational domain. As mentioned before in the mass conservation equation, the domains that are used in the present work, are rectangular. Unless another boundary condition is specified, free convection is set over all the boundaries. Different to the mass conservation equation, the energy equation (42) is resolved in all the domains, such as indicated in Figure 48.

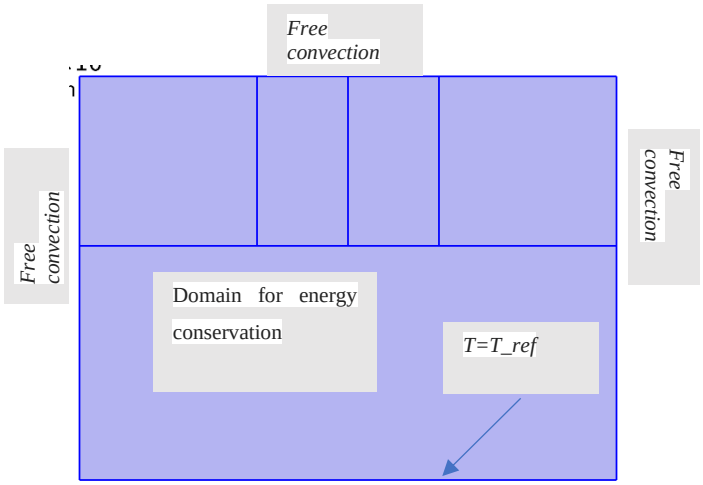

Figure 48. Domain and boundary conditions for specific enthalpy.

4.6 Velocity field

Different models are used to approach the PBF processes from different perspectives according to the experimental data. Sometimes the velocity field is an unknown that is solved by implementing some type of Navier-Stokes model. However, when solving the fluid flow in addition to the free surface and temperature, very time-consuming models are produced. These models are usually focused on the powder scale, in which the interaction between the heat source and powder particles melting is the main interest. In order to simplify such expensive flow models, a simplification is proposed in which the velocity field is determined without actually solving the Navier-Stokes equation. This approach uses the same idea of the imposed velocity field mentioned in Chapter 3; however, in this case the velocity field is not completely imposed but now a dependency on temperature is assigned. The proposed velocity tries to represent the desired downwards movement of the material, allowing its densification. Thus, a velocity with a predefined direction and magnitude is specified, but the region in which this velocity is applied is

unknown. This region is determined by the temperature field (or enthalpy). The criterium to determine whether a location is going to move or not, is defined by the melting temperature defined as:

$$T_m = \frac{T_L + T_S}{2} \tag{49}$$

being T_L is the liquidus temperature and T_S is the solidus temperature of the alloy. Then, following the idea of Equation (30), the velocity field for the PBF model is:

$$\vec{v}(\phi, \vec{x}, t) = v_{down} \begin{bmatrix} 0 \\ -\left(1 - 1.04 H_s(\phi - 0.967, 0.05)\right) \end{bmatrix} \cdot H_s\left(T - T_m, g \cdot \frac{T_L - T_S}{2}\right) \tag{50}$$

Where H_s is the smooth Heaviside function and g is a multiplier of the temperature range in which fusion takes place. The value of this parameter that is used in these simulations is explained in section 4.7.2. The velocity constant v_{down} is the upper limit of the magnitude of the velocity field and is approximated by the velocity of the scanning during the heating process. A good way to approach this value is by $v_{down} = c_{down} v_{laser}$, being $c_{down} = 2$ for the presented cases. This value guarantees that the melted material fully moved when the beam already passed.

4.7 Material properties

Thermal properties, such as density (ρ), specific heat (C_p), and conductivity (k), as well as the velocity field ($\vec{v}$) determine the energy equation behavior. However, as it was mentioned before, in this level set model the surrounding atmosphere is also considered as part of the model, to avoid a zero-mass matrix which can cause instability and sensitivity in the solver. Therefore, surrounding gas properties can be added in the case of SLM. For the EBM artificial values can be added just to avoid an ill-conditioned matrix. To approximate the values of material properties at the interface, a linear mixture rule as function of the LS function ϕ is used.

The density is then simply approached by a single linear relation as:

$$\rho(\phi) = \rho_C \phi + (1 - \phi)\rho_V \tag{51}$$

For the specific heat a linear relation is also proposed but, in this case, a weighting function is also coupled. Basically, this definition is based on the application of the linear mixture rule to the heat capacity rather

than the specific heat capacity. This allows a linear mixture rule over the stored energy rather than just specific heat. This C_p relation is written in Equation (52), in which $C_{p,V}$ stands for the specific heat in the void and $C_{p,C}$ is the specific heat in the consolidated material:

$$C_p(\phi) = \frac{\rho_C C_{p,C}\phi + (1-\phi)\rho_V C_{p,V}}{\rho(\phi)} \tag{52}$$

A plot for the $C_p(\phi)$ function is shown in Figure 49.

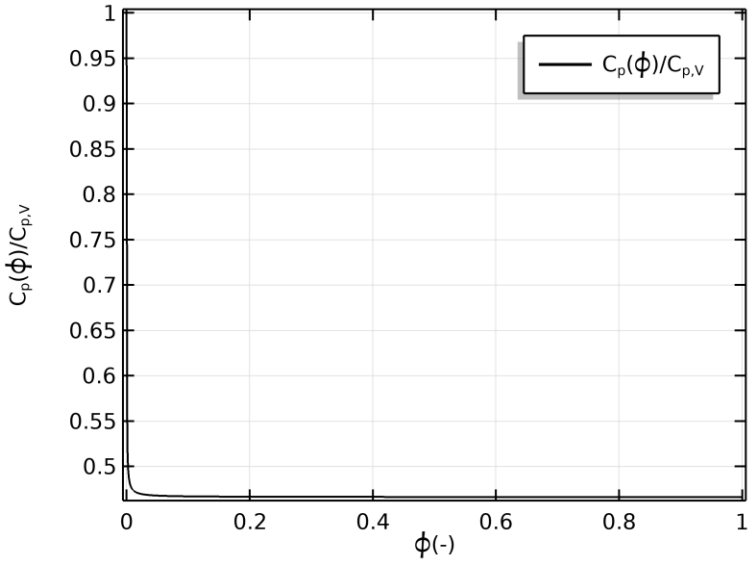

Figure 49. Effective scaled $C_p(\phi)$.

Although a single linear relation seems appropriate for all different interfaces both density and heat capacity it is not the case for conductivity, because of the dissimilar magnitudes between the conductivity in air, powder and consolidated material that would produce incorrect interpolated values. To avoid an incorrect interpolation function in thermal conductivity, two functions are developed. The first conductivity k_{VPC} is a double linear relation that is applicable to the powder zone and the VP and PC interfaces. In (53) the k_{VPC} relation is shown. A second conductivity k_{VC} is applied to the VC interface. This relation is a single linear relation between the properties of the void and the consolidated material. The k_{VC} relation is shown in equation (54). A scaled plot for the two conductivities is shown in Figure 50.

$$k_{VPC}(\phi) = \begin{cases} \dfrac{\phi - \phi_V}{\phi_P - \phi_V} k_P + \dfrac{\phi_P - \phi}{\phi_P - \phi_V} k_V & \phi_V \leq \phi < \phi_P \\ \dfrac{\phi - \phi_P}{\phi_C - \phi_P} k_C + \dfrac{\phi_C - \phi}{\phi_C - \phi_P} k_P & \phi_P \leq \phi \leq \phi_C \end{cases} \tag{53}$$

$$k_{VC}(\phi) = k_C \phi + (1 - \phi) k_V \tag{54}$$

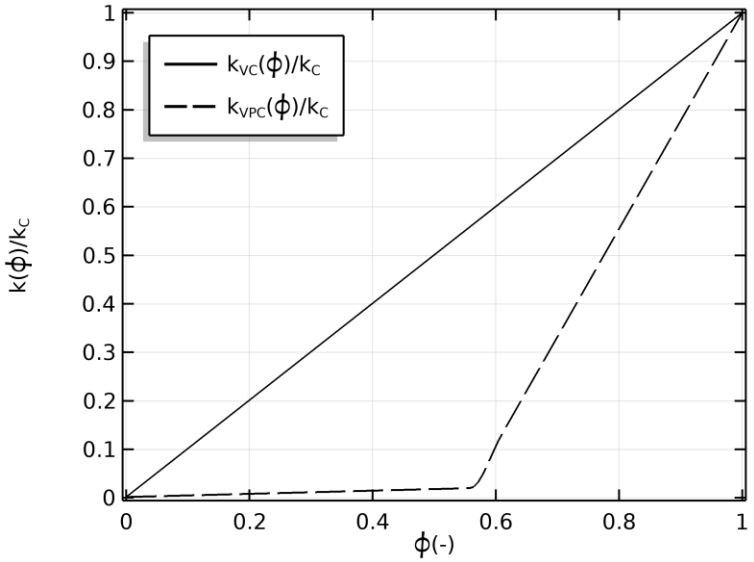

Figure 50. Scaled conductivity k_{VC} and k_{VPC} for the VC and VPC interfaces respectively.

This approximation demands to have the conductivity data of powder and the surrounding gas, however, if no experimental value for powder is available, it was found that an approximation of around 1% to 5% of the bulk conductivity can be used instead. Similarly, a 10% of powder conductivity is a suitable value for void, as it was previously stated from Chapter 2.

Material properties are not only a function of the phase function ϕ, but also are temperature functions. Therefore, a variation of material properties as function of temperature is added. To do that, the thermal effect written in Table 1 is coupled to the relations from (51) to (54). This way material properties can represent both phase and temperature variations.

4.7.1 Sensible Heat, Latent Heat and Related Topics

The heat capacity that is used along this thesis is the apparent heat capacity, which already includes the latent heat distributed over a temperature range. Ideally, alloys have a well-defined range in which latent heat is released/absorbed. However, for numerical purposes, this range is usually too small to be suitable

for simulations, since such small temperature range would require a fine mesh. If a small temperature range is used with an insufficiently refined mesh, numerical instabilities and lack of convergence might occur, due to the abrupt transitions in the solution and the properties. In Figure 51 the sensible (a), latent (b), and (c) apparent specific heat are shown, where the abrupt spike related to the latent heat can be appreciated. Although it is possible to implement this specific heat behavior, in practice is not feasible, and an increase of the temperature interval is needed, such that the latent heat can be incorporated over a larger temperature range, which lowers the peak value of the spike.

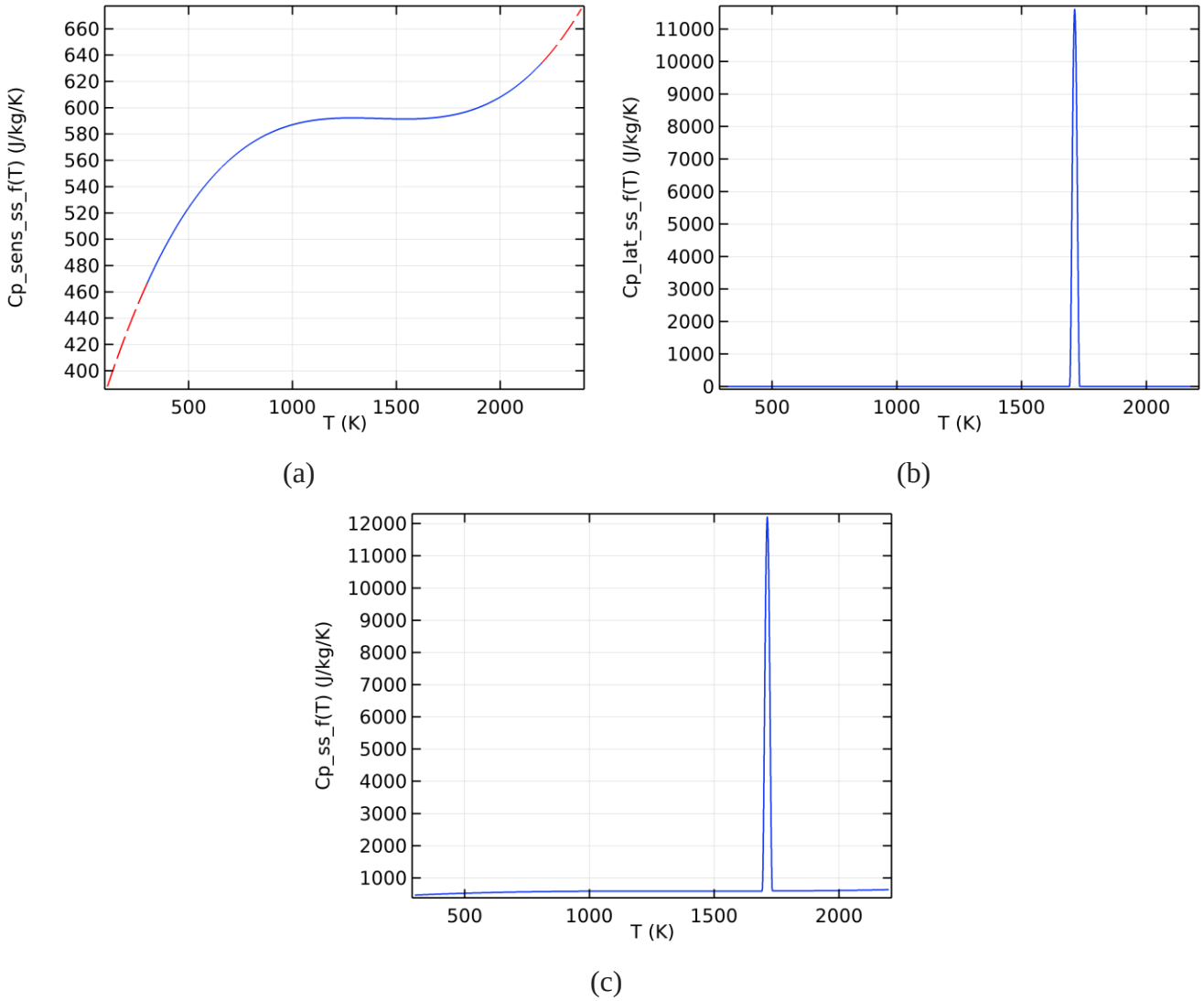

Figure 51. Specific heat (a) sensible (J/(kg · K)), *(b) latent* (J/(kg · K)), *and (c) apparent or total* (J/(kg · K)).

In order to fully appreciate this problem, a test case using the enthalpy method that shows the effect of a narrow melting region as well as a solution to that problem is addressed in the following paragraph. To

do that, enthalpy functions are created knowing the $C_p(T)$ relations and using the thermodynamic definitions between specific heat and enthalpy: $\mathrm{d}h = C_p \mathrm{d}T$, and then $\int_{h_{ref}}^{h} \mathrm{d}h = \int_{T_{ref}}^{T} C_p \mathrm{d}T$, where $T_{ref} = 300$ K and h_{ref} is the enthalpy at T_{ref}. The enthalpy functions are plotted in Figure 52: (a) sensible, (b) latent, and (c) apparent (total) enthalpies. In (c) it is possible to appreciate the abrupt change in the enthalpy when increasing just a few degrees in the temperature.

The common solution to this problem is to widen the temperature range. A quick estimation can be carried out by getting the ratio between the slopes of the sensible enthalpy and the latent enthalpy in Figure 52c. So, the goal is to determine the increase the transition region by a factor g the temperature range, such that the melt range is modelled as: $g(T_L - T_s)$. Comparing the enthalpy slopes of sensible enthalpy and latent enthalpy shown in Figure 52c, the approximate ratio can be estimated as: $g \approx (0.3/40)/(0.8/1700) \approx 16$. $g = 16$ would guarantee a similar behavior than the one that would be obtained in a location that does not reach melting. However, the main goal is to keep this temperature range as narrow as possible.

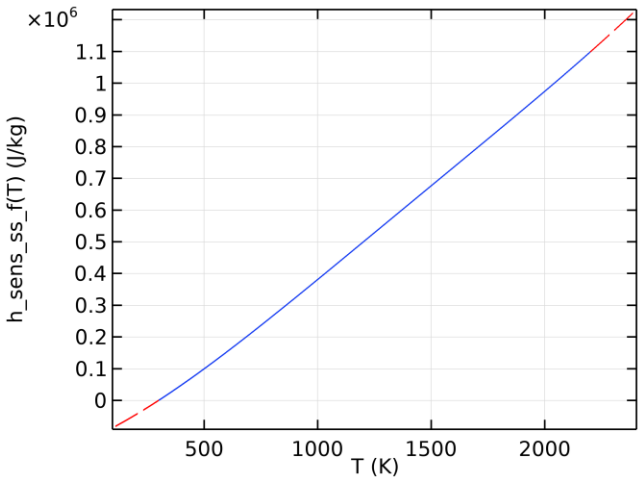

(a)

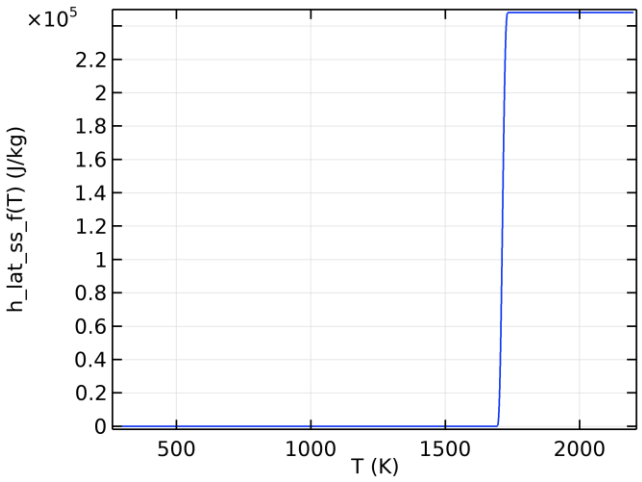

(b)

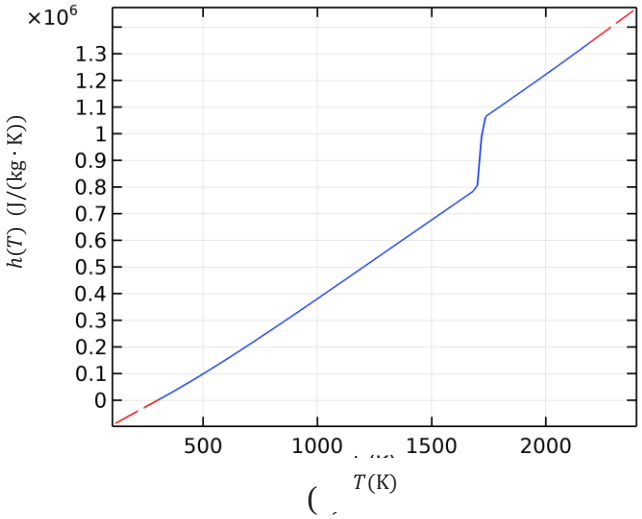

Figure 52. Different enthalpies using a temperature range, $T_L - T_S$, equal to the material properties (a) Sensible enthalpy (b) latent enthalpy (c) apparent enthalpy ($h=h_s + \Delta H$).

To verify the performance of the model under different temperature ranges, a parametric study was carried out using the data shown in Table 5 and Table 6. A series of values is tested and plot in Figure 53 using: $g = \{1, 2, 4, 8, 16\}$.

Table 5 Level set parameters for the test case.

Domain	$\Omega = \{(x, y) \mid -13.5 \times 10^{-4}\ \text{m} \leq x \leq 0;\ -5 \times 10^{-4}\ \text{m} \leq y \leq 20 \times 10^{-4}\ \text{m}\}$
Element type	Rectangular
Element order	Quadratic
Element size (e_z)	3×10^{-5} m
Diffusion coefficient	$\varepsilon = 2\sqrt{2}\, e_z = 8.49 \times 10^{-5}$ m
Reinitialization factor	$\gamma = 1$ m/s

Table 6 Process parameters for the test case.

Parameter	Value
Power (W)	110
Beam radius (m)	0.3
Speed (mm/s)	80
Relative powder density (-)	0.56
Energy efficiency (-)	52%

It is possible to verify that the real temperature range $g = 1$ produces a non-suitable enthalpy field with large local spikes in the effective heat capacity. The apparent heat capacity, gets better and better as g

increases, being $g = \{8, 16\}$ the best results. For the upcoming simulation cases $g = 8$ is chosen, since it keeps an acceptably narrow transition, with a width that is comparable to the transition width of the level set values in the interfaces, which guarantees a sufficiently smooth enthalpy field.

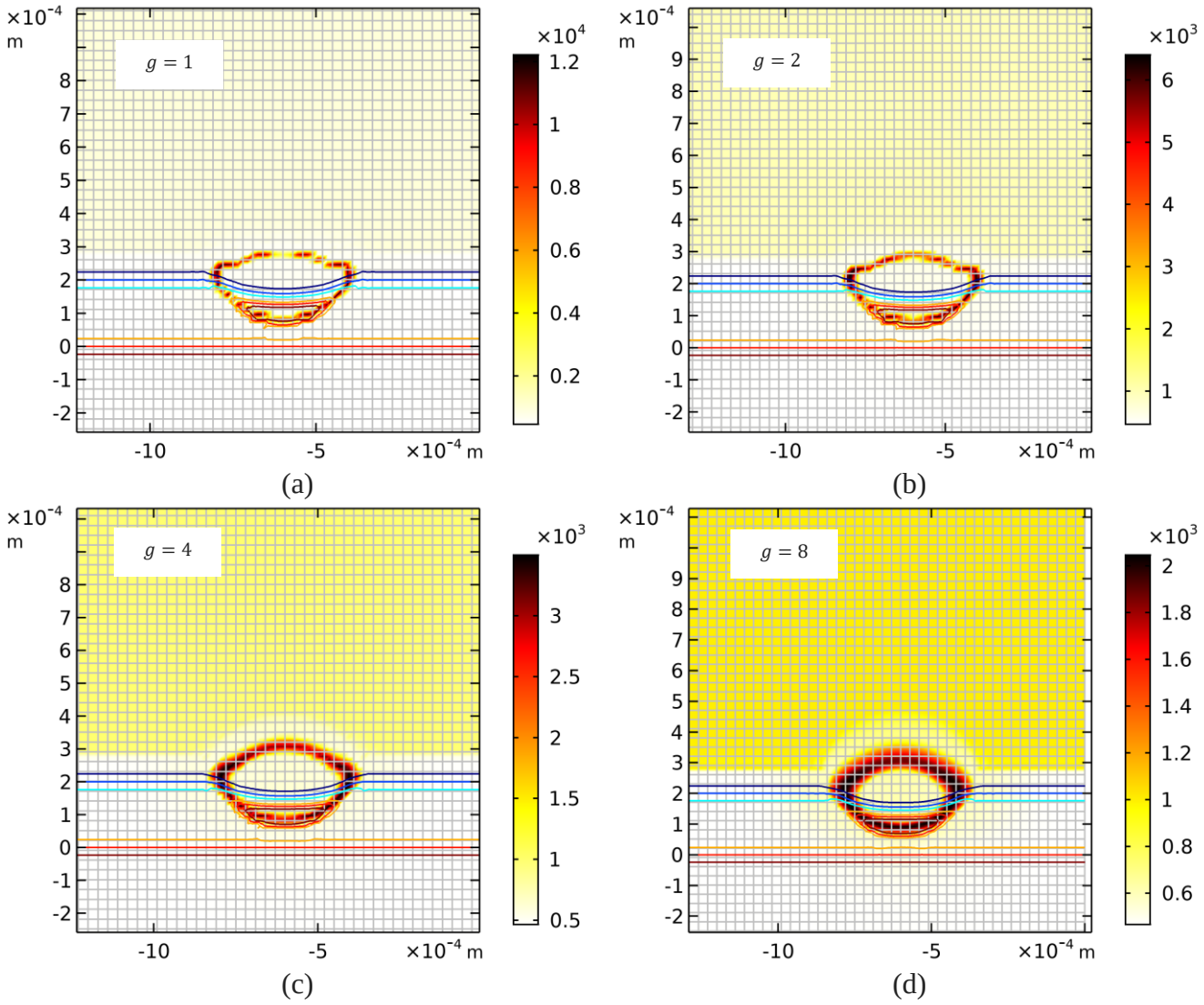

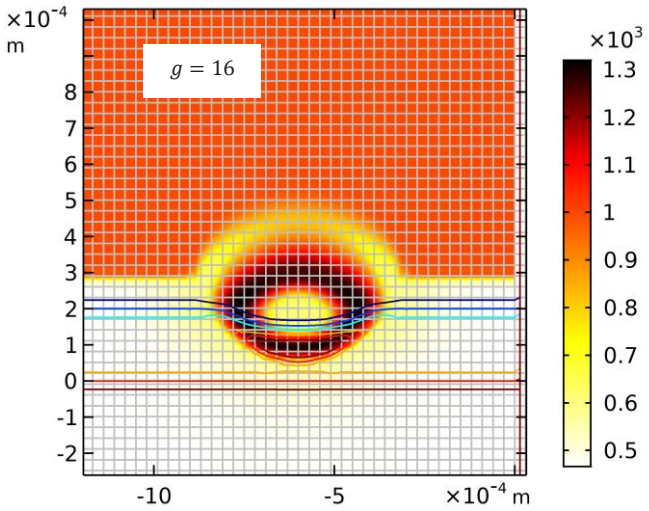

(e)

Figure 53. Apparent specific heat $(\mathrm{J}/(\mathrm{kg}\cdot\mathrm{K}))$ *for different* $\Delta T = g(T_L - T_S)$.

4.8 Verification of the energy governing equation

The validation of the model is tested by some energetic considerations when implementing Equations (35) and (42). The numerical specifications and values used in the model are provided in Table 5 and Table 6, and uses the material properties listed in Table 1 for SS316. Boundary conditions for the solved variables, level set and specific enthalpy, are the same as those indicated in Figure 44. In order to test the Beer-Lambert heat source and the energy conservation during the process, neither convection nor radiation are considered in this study.

The first proof consists in verifying that the input energy is the same as the one captured in the model by the specific enthalpy. To do that some time-space integrals are performed. The first integral evaluates the energy delivered by the Beer-Lambert equation that can be calculated using an integral over the time domain, t, and the space domain (in this case an area: A): $\iint q_{in}\mathrm{d}t\mathrm{d}A$. The second integral is the total current energy present in the domain (enthalpy). This energy is calculated with a single domain integral: $\iint \rho h\mathrm{d}A$. This is performed over each time step during the simulation time and plot in Figure 55. Both curves agree which means that the energy added is exactly the same as the energy present in the solution.

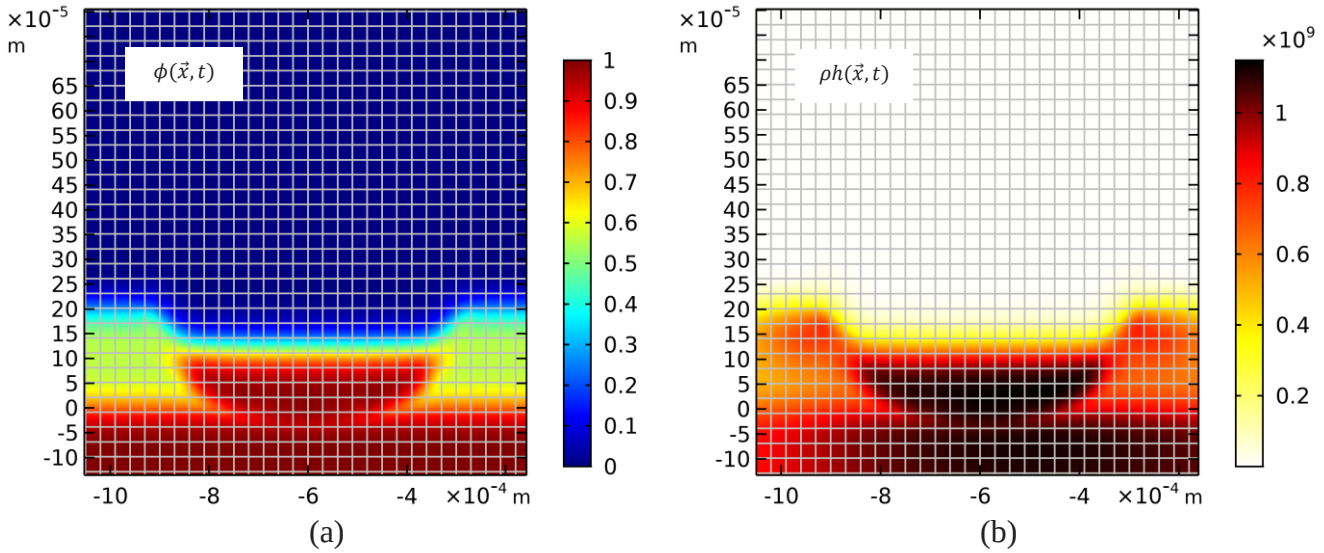

Figure 54. Final state after finishing one track (a) $\phi(\vec{x},t)$ and, (b) specific enthalpy ρh (J/kg).

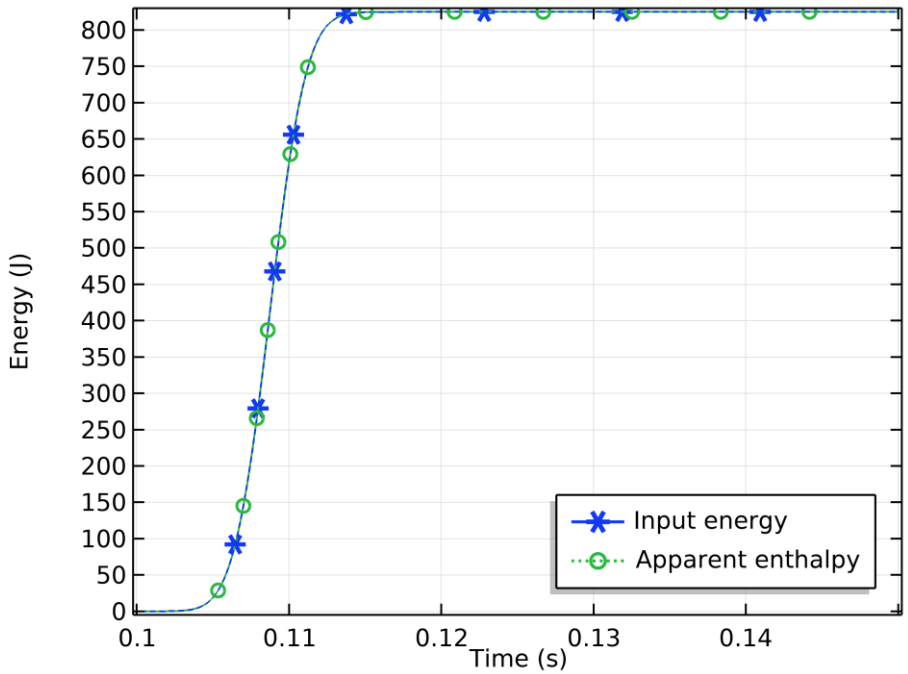

Figure 55. Energy verification in the model: (a) Added energy and (b) measured energy (solved variable: enthalpy).

A second proof was performed in order to verify the correctness of the material addition and its energetic considerations in the model. To validate the energy conservation during the powder deposition phase, a second layer of powder is added to the domain using Equation (43). The results after the application of a second layer of powder and a second track are shown in Figure 54. Again, two integrals are compared to verify the energy conservation. The first integral is over the last term in Equation (42). This source term

represents the heat added by mass addition, it is to say, a layer of powder. The term that quantifies for the creation of new powder layers is $h_{mass} = (h_{powder} - h)\dot{s}_{mass}$. Then, the time-space integral is taken over this term $\iint h_{mass} \mathrm{d}t\mathrm{d}A$. This term is added to the input energy to produce the total input energy. The other integral stays the same $\iint \rho h \mathrm{d}A$. The two integrals are plotted in Figure 57where the energy conservation can be verified. In Figure 58 the percentage error is show, and it shows that the relative error is less than 0.5% which is considered acceptable.

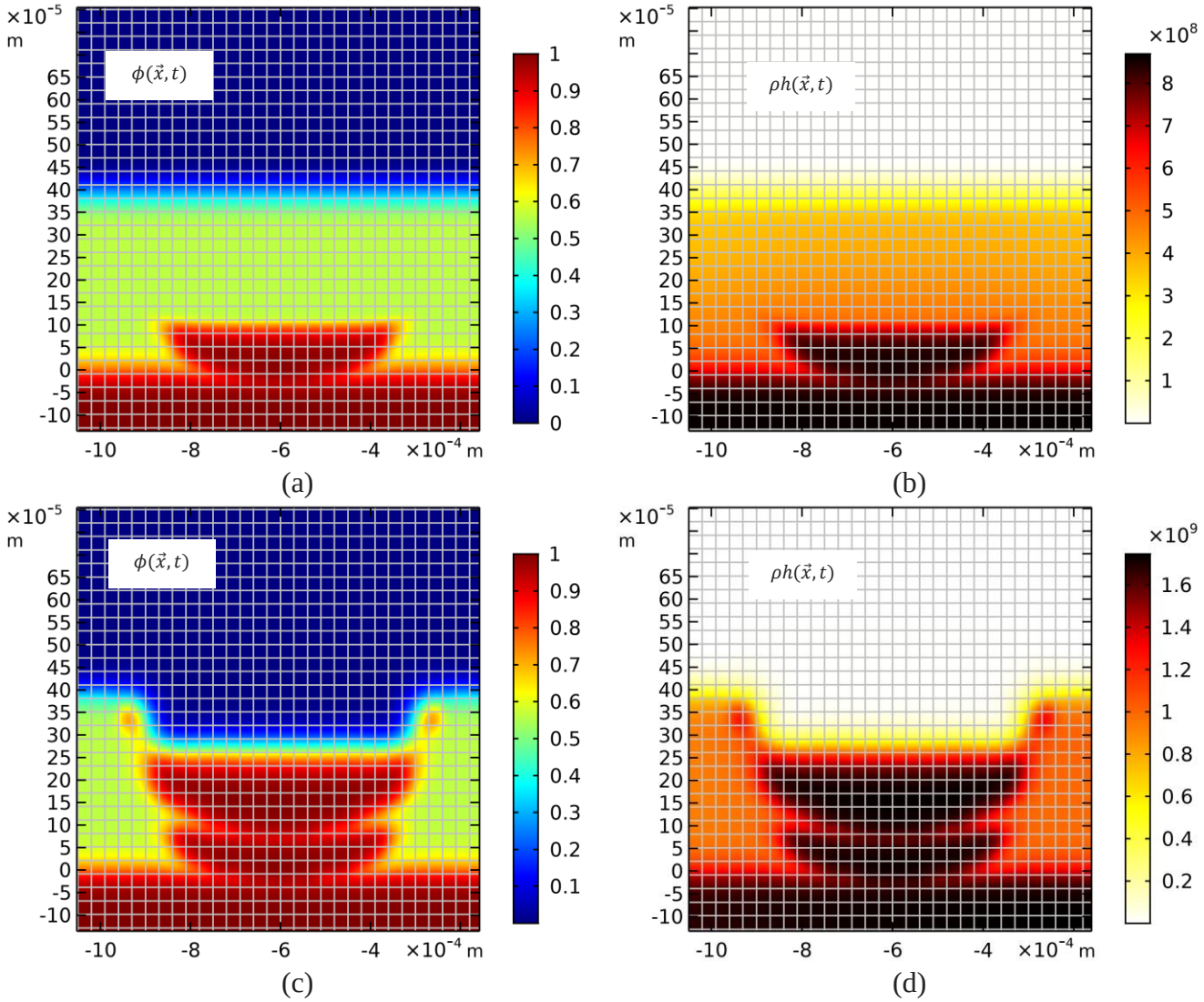

Figure 56. Final state after the application of a second layer of powder (a) $\phi(\vec{x}, t)$ [−], and specific enthalpy (b) $\rho h(\vec{x}, t)$ (J/kg). Final state after the second track (c) $\phi(\vec{x}, t)$ and, (d) $\rho h(\vec{x}, t)$.

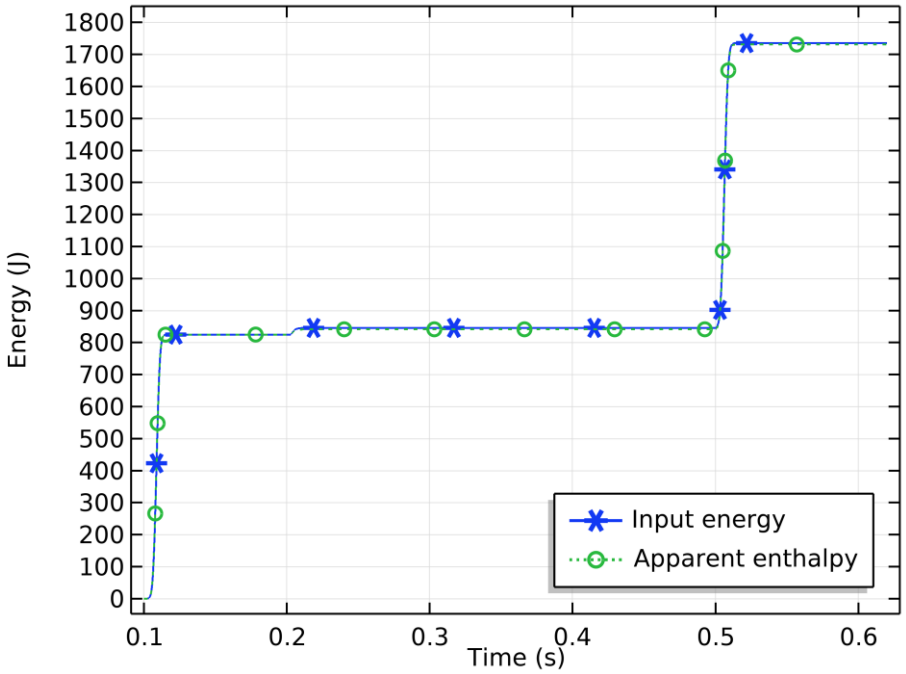

Figure 57. Energy analysis for input energy vs the measured apparent specific enthalpy.

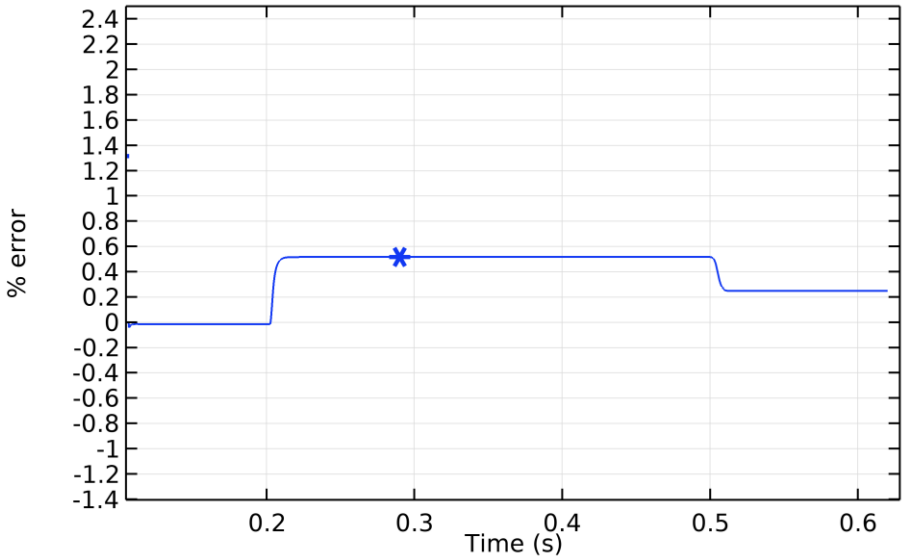

Figure 58. Percentual error in the analysis of energy vs the measured apparent specific enthalpy.

5 Application and Validation of the Simulation Model

In order to test the PBF model developed in the previous chapter, a set of case scenarios from literature are simulated. These case scenarios are approached by 2-D models; however, this can also be performed using a 3-D approach. The first case comes from the article written by Foroozmehr et al., [66], here the authors presented both experimental results and simulation results. The second case scenario comes from the article written by Mukherjee et al., [30]. In this article, the authors describe the development of a model that includes 3-D fluid flow simulation. These two articles show morphological results of the melted powder layers, both experimental and computational, which is the main interest of the current work. Two materials are considered in this comparison.

5.1 Case 1: Foroozmher

In order to test the proposed model, a comparison with experimental results found in the literature is carried out. The melt pool's morphology is the object of comparison. In the chosen case study, tracks of 15 mm length are used to create a hatch of 15 mm x 15 mm in a relatively thick powder layer of 1mm thickness. The morphology of two tracks is presented and compared with experimental results. The tracks are built using an SLM machine in an argon atmosphere using the data shown in Table 7. The experimental scanned powder region is a prism of 15 mm x 15 mm x 5 mm. According to the reference article, experimental results show that after the fourth track there are no significant changes in the size of melted zone.

In order to reduce the computational time, 2-D simulations of only 5 tracks are carried out in this case study. The computational domains are shown in Figure 59, in which the boundary conditions for each of the three solved fields are also included.

Table 7 experimental parameters by Foroozmehr et al. [66].

Material and process parameters	**Values**
Laser power (W)	110
Beam radius (mm)	0.3
Layer thickness (mm)	1
Scan speed (mm/s)	80, 100, 150
Track length (mm)	15

Material	SS 316L
Energy efficiency	52%

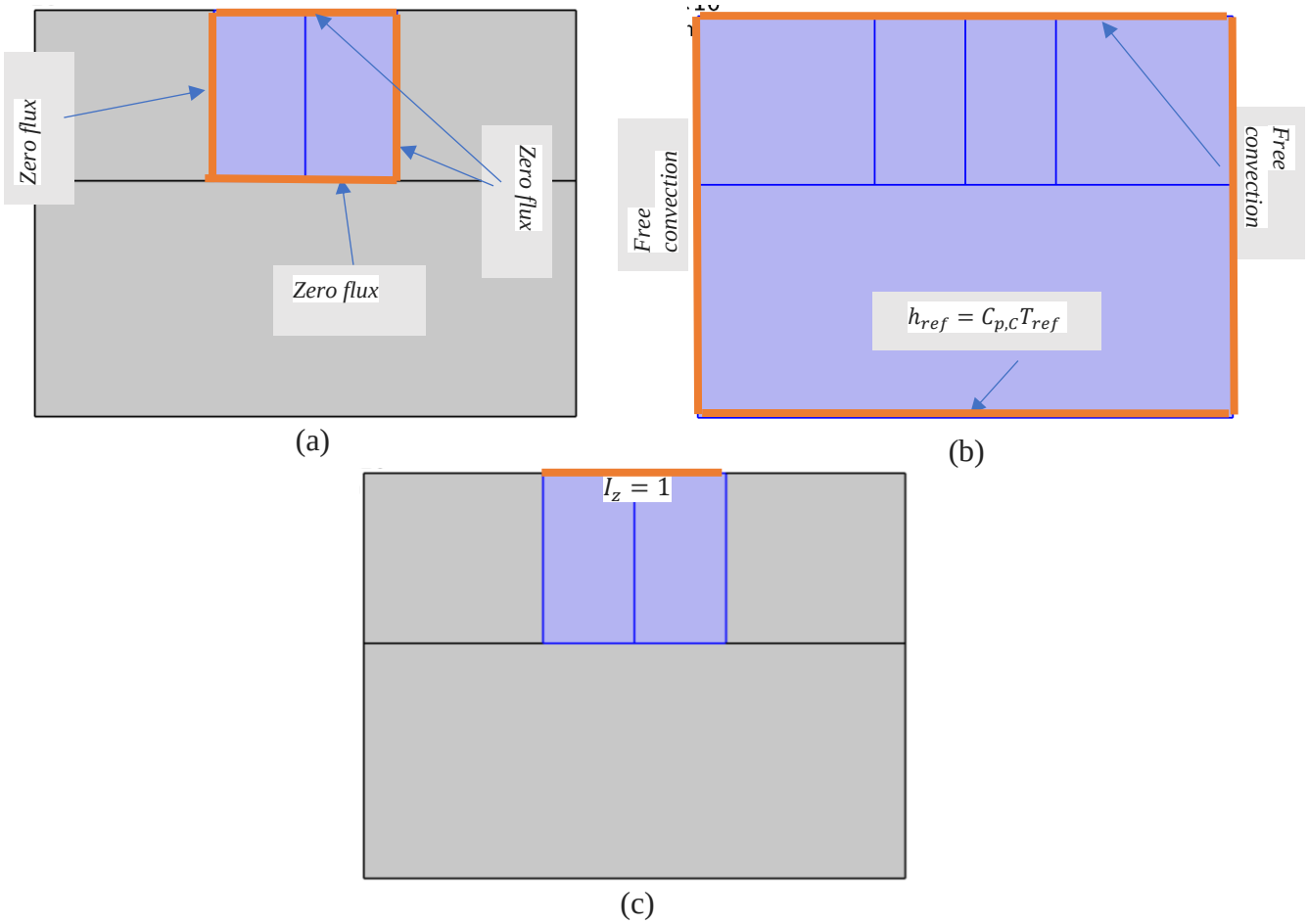

Figure 59. Boundary conditions for: (a) ϕ-field, (b) h-field, and I_z-field.

The domain is meshed using two different types of meshes. One is a structured mesh in which level set equation (35), specific enthalpy equation (42), and Beer-Lambert equation (47) are solved iteratively in segregated solver steps. The second mesh is an unstructured mesh in which only the specific enthalpy field equation (42) is solved. The structured mesh consists of 9240 quadrilateral second order Lagrange elements, whilst the unstructured mesh is composed of 4935 triangular second order Lagrange elements. In Figure 60 the two meshes are shown.

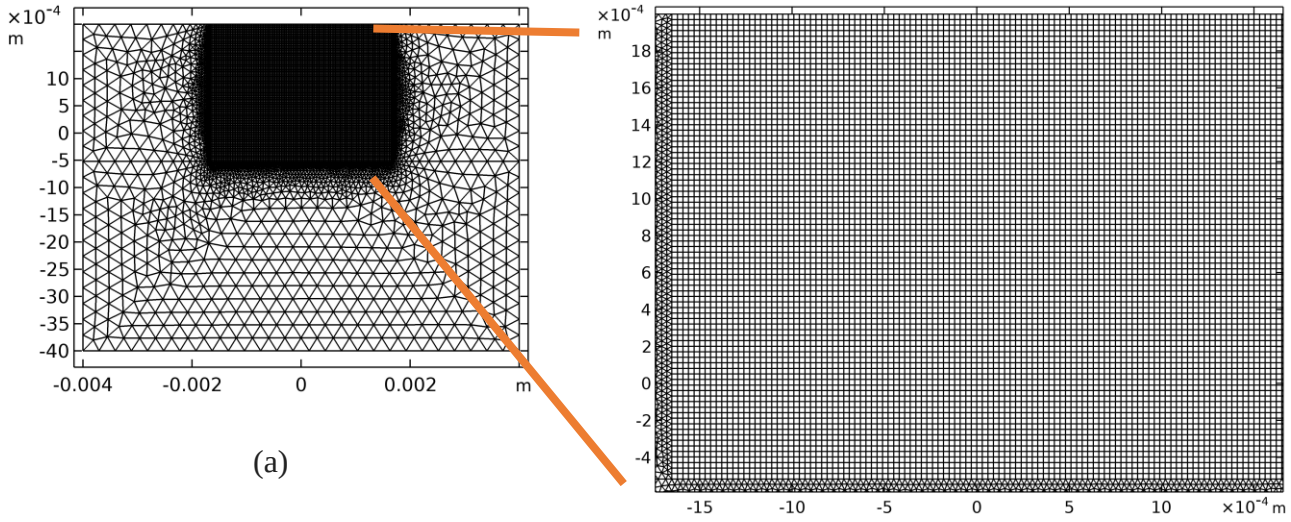

Figure 60. Domain mesh. (a) Free mesh with max. element size 2.96 10^{-4} m *and min. element size 3* 10^{-5} m*, (b) regular mesh 3* 10^{-5} m.

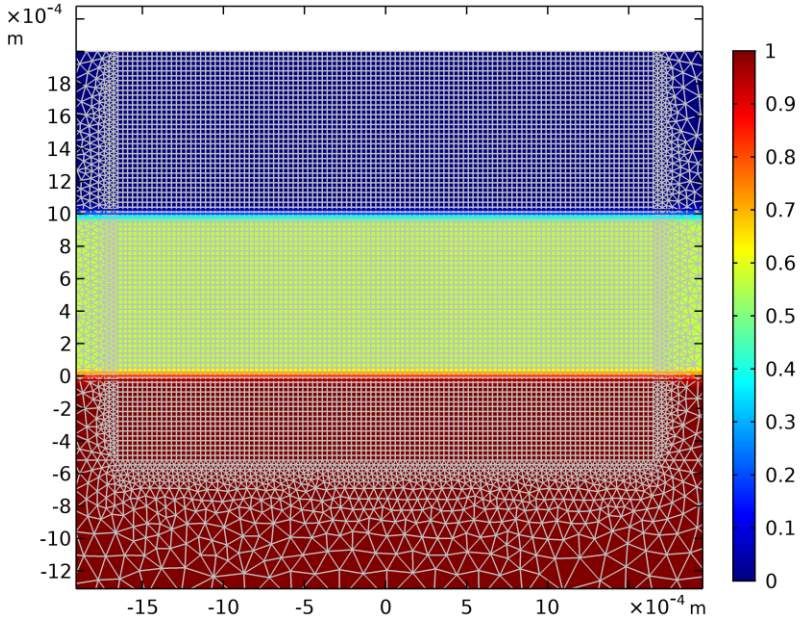

Figure 61. Initial condition for the ϕ-field.

Although both the structured mesh domain and the non-structured mesh domain are colored in the image, the field is only solved in the structured mesh region and constant values are assigned all over the non-structured mesh. In this figure, the 1 mm powder layer is shown in yellow ($\phi = 0.56$), while the blue colored area represents the surrounding gas $\phi = 0$. A base plate of SSL316L has a red color according to $\phi = 1$. A smooth transition of 2ε between all interfaces is set. Initial conditions for the ϕ-field is shown in Figure 61. The initial condition for the specific enthalpy field is just the specific enthalpy at the room temperature $T_{ref} = 293$ K. The initial condition for the Beer-Lambert field is $I_z = 0$ over the domain.

5.1.1 Results

This case study consists of an analysis of five tracks. The study is repeated for three different speeds: 80 mm/s, 100 mm/s, and 150 mm/s. In Figure 62 a sequence of images of the evolving interface is presented. In this image the three different types of interfaces can be observed. At the beginning only two types of interfaces appear (with three phases/levels). In the image it is possible to notice that the method is capable of initiating the melt pool as well as to keep the evolution of the three coexisting phases. The effect of densification is also noticeable.

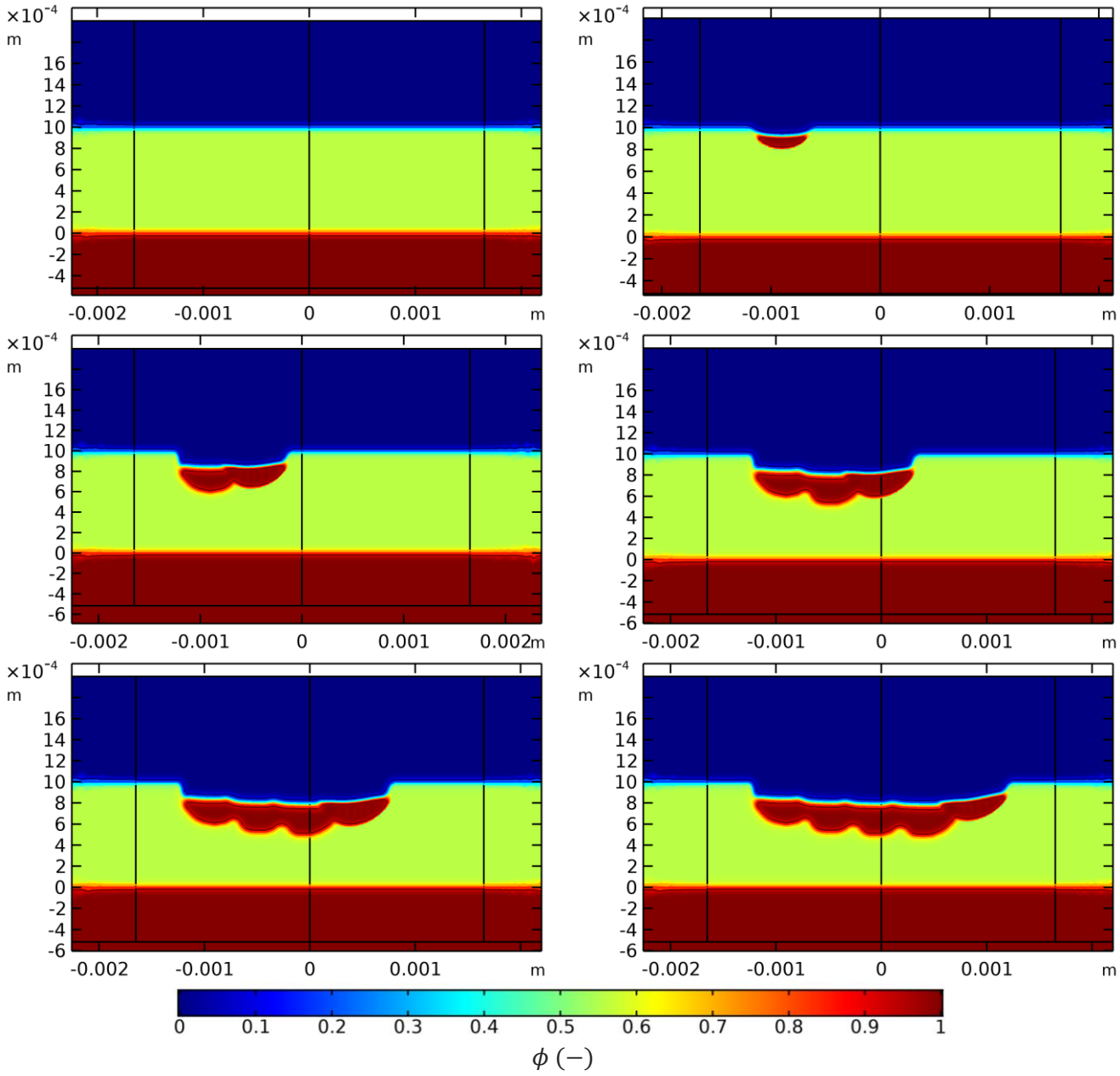

Figure 62. Cross-section. Evolution of ϕ-field for 5 tracks.

After some heat is applied, a melt front appears in the powder region, on top of the powder layer. The melted zone keeps growing until the heat source ceases and the heat in the melt pool is not enough to sustain further fusion, and will start to cool down and solidify. This process is repeated until the five tracks are scanned. It is worth to mention that the reference case study is performed over a thick powder layer, therefore, there is no interaction with the consolidated substrate. As a result, powder acts as good insulator due to the low thermal conductivity, which is around 5% of the bulk material. This produces some increase in the penetration depth of subsequent track, due to the heat accumulation in the patch. Figure 63 shows the temperature field corresponding to the level set shown in Figure 62.

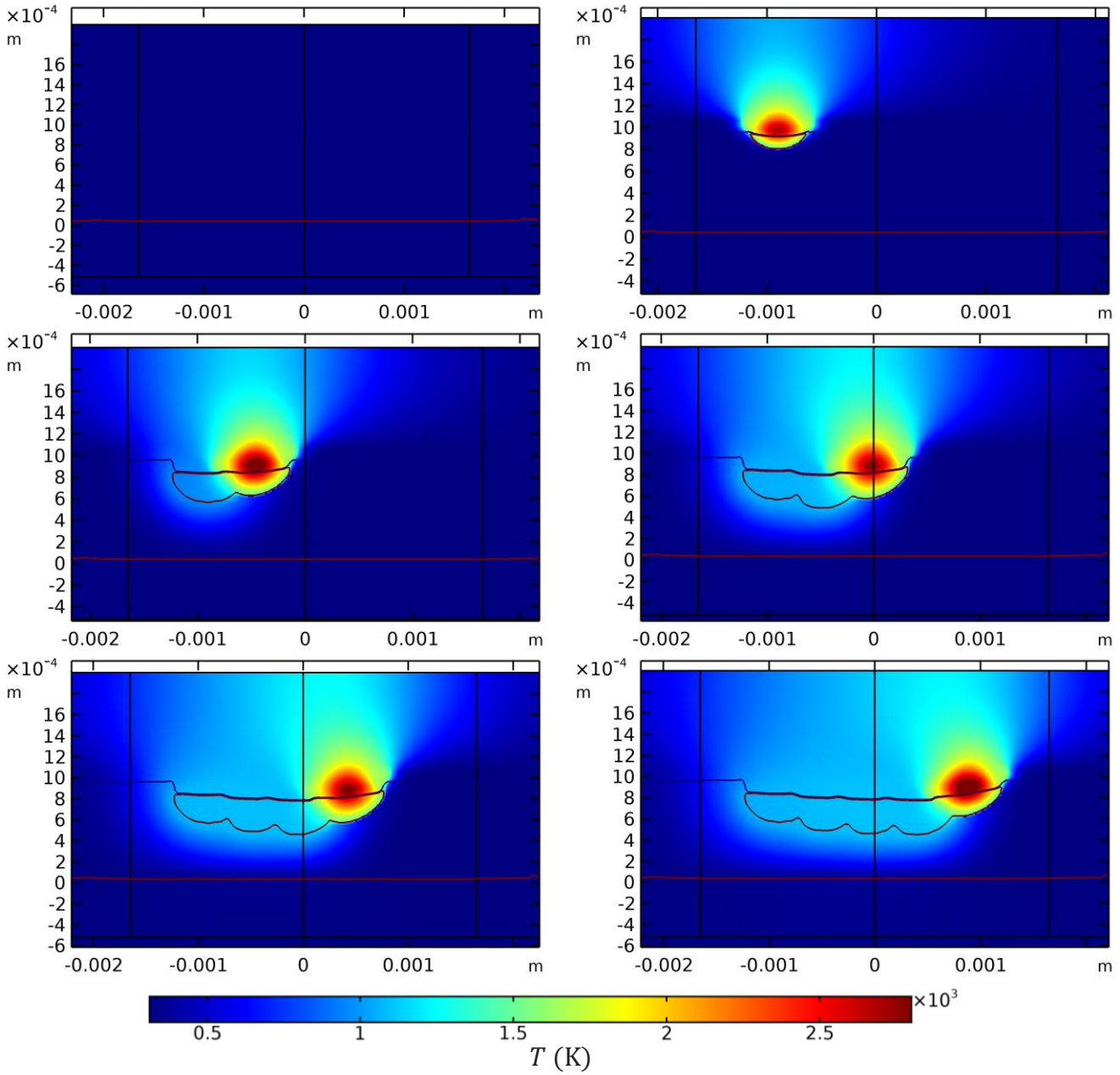

Figure 63. Cross-section Foroozmehr case study. Evolution of temperature field for 5 tracks.

In Figure 63 the peak temperatures are shown to occur in the void as well as at the top interface of the melt pool due to the low heat capacity of the gas, requiring only a small amount of energy to reach high temperatures. In addition to the low heat capacity the heat source delivers a relatively high energy intensity in this zone, due to the typical Beer-Lambert absorption that shows it main decay and energy conversion near the incident boundary. However, temperature in the consolidated material is realistic.

Figure 64 shows the formation of the cross-section of the 5 tracks at the end of the process after cooling down. This image is the result of a boolean filter applied with the solidus temperature. This image shows the areas where phase transformation from liquid to solid took place. Opposed to the level set observed in Figure 62, this image has no smooth transitions. The morphologies of the three cases are very much alike since a concave melt front appears near to the previous track and a convex shape appear next to the powder. This behavior is consistent in all the cases. In the reference case (Foroozmehr et al. [66]) it is reported that no significant change in the height of the melted zone is noticed.

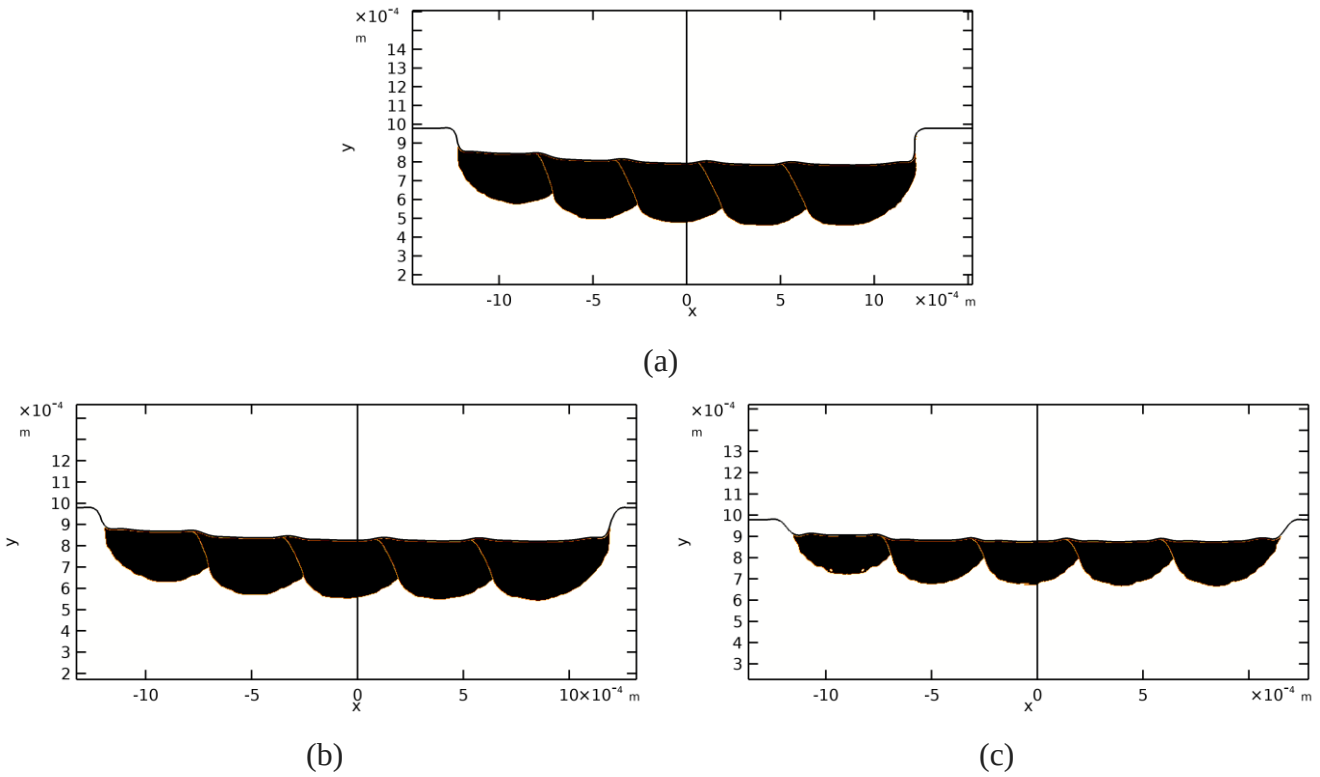

Figure 64. Melted zone for (a) v *=80* mm/s, *(b) 100* mm/s *and (c) 150* mm/s.

The first comparison is the melt pool morphology of the v_L=80 mm/s case. The experimental results shown an average height of the melted zone of 355 µm, whereas the average heigh of the melted zone in the simulations is 308 µm. In Figure 65 a comparison is shown between the simulation results of the proposed model and the experimental results by Foroozmehr et al. [66]

The average depth for v_L =100 mm/s and v_L =150 mm/s is 260 µm and 202 µm respectively. A comparative figure between the simulation and experimental results is depicted in Figure 66a. In Figure 66b the relative error is shown, in which a maximum error of 13% between experiments and simulation

can be appreciated. Something interesting to note is the change in the sign of the error that will be furthered discussed.

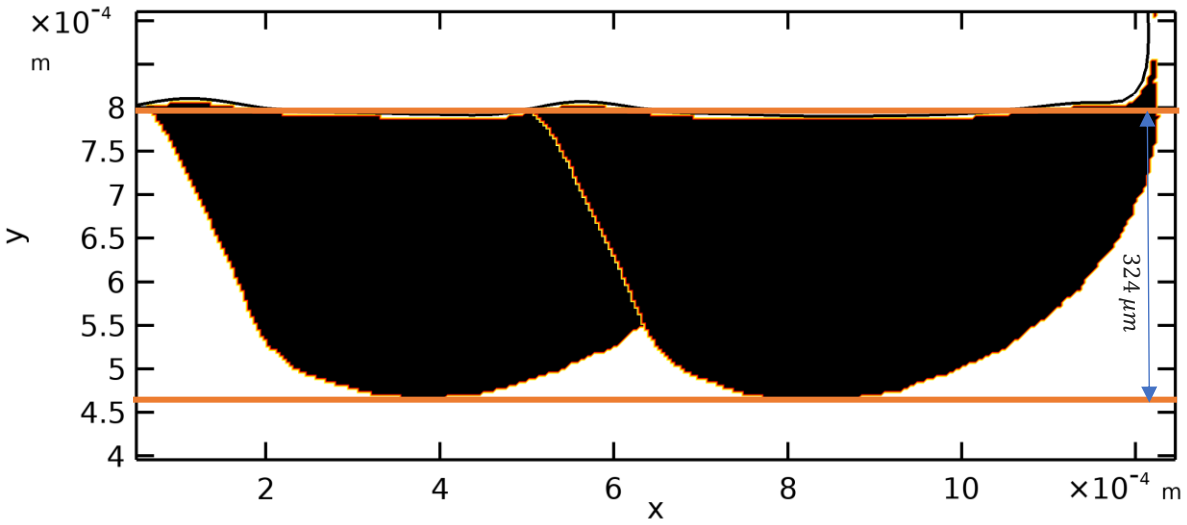

(a)

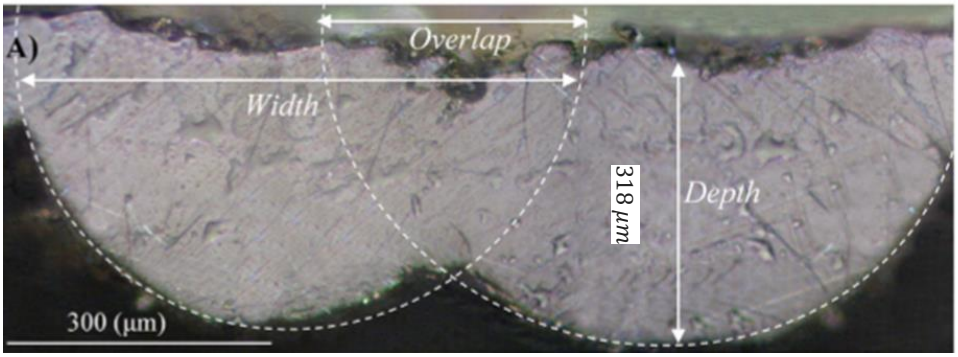

(b)

Figure 65. Cross-section morphology of two tracks, (a)This work, (b) Foroozmehr et al. [66].

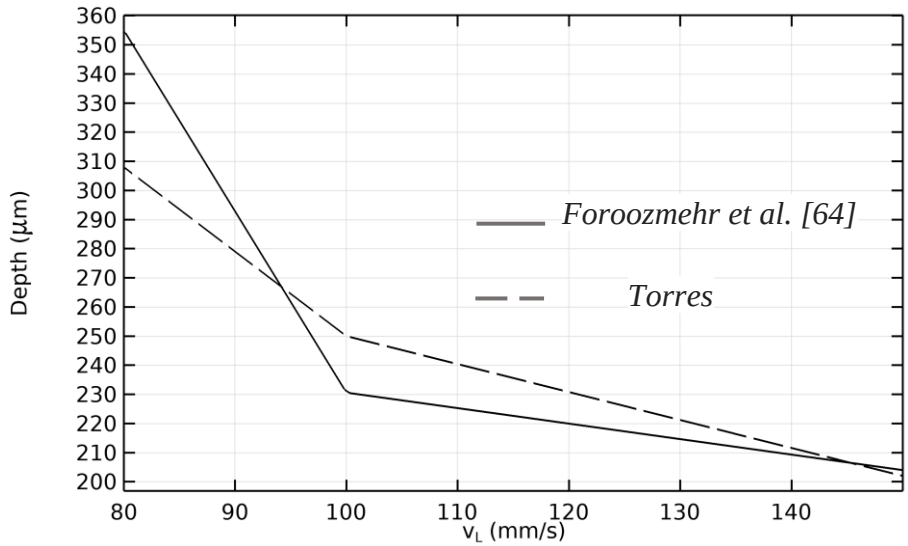

(a)

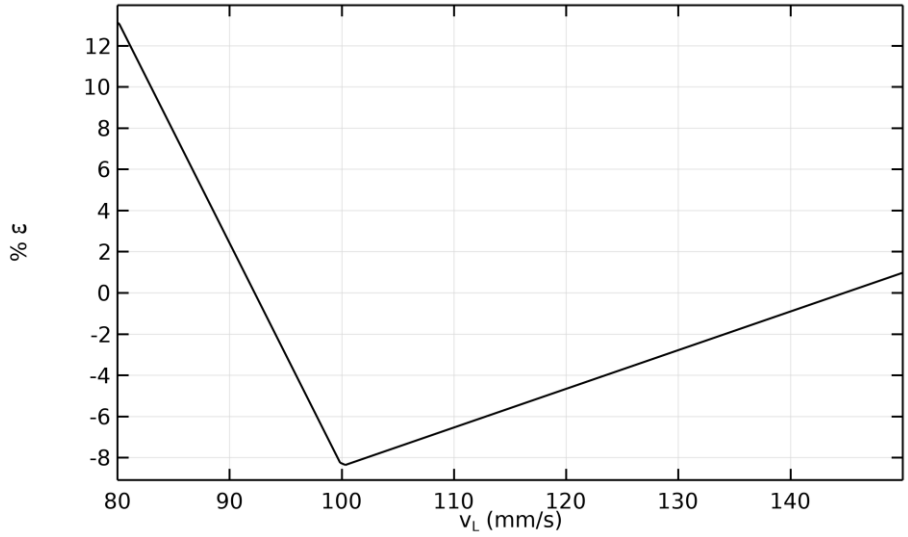

(b)

Figure 66. Comparison between experimental (Foroozmehr et al. [66]) and simulation results (this thesis), (a) melted zone depth. Continuous line and (b) relative percentual error.

5.1.2 Discussion

The results showed good agreement with experiments, in particular at high speeds, see Figure 66. This result is attributed to the heat transfer by conduction and convection present in the melt pool of the physical experiment. In the model proposed in Chapter 4, no fluid flow is incorporated in the strict sense, since no Navier-Stokes equation is solved, instead a velocity field is implemented that depends on temperature and only serves to capture the densification of the powder. However, this velocity field exists only when material is not consolidated, because when material is consolidated the criterion is to stop the movement

to prevent an over densification that could produce $\phi > 1$. As a result, only a 'limited' movement is generated inside the melt pool when the melt front advances. Basically, when the level set reaches a value near full densification conduction becomes the main heat transfer mechanism. The simulation results show that the average height of the melt pool was slightly less than expected, but only at the lowest speed. Since at 100 mm/s the model predicts a larger melt zone. This might be due the changes in the primary heat transfer mechanism when energy is too high, passing from conductive mode to keyhole mode. In the keyhole mode, the heat transfer to the melt front at the bottom of the melt pool increases significantly, since the top surface is pushed downwards to close in on the bottom surface. Currently, this effect is not incorporated in the model, which can explain that the current model underpredicts the melt pool penetration depth when the keyhole mode starts.

5.2 Case 2: Mukherjee

A second case scenario is developed to compare with a case study reported by Mukherjee et al., [30], in which a thermal-fluid flow model is solved by a computational model and compared with experimental results. The main interest to compare with this computational case is because their results include the morphology of the melt pool. It is worth to mention that the author tested and compared their model with several experimental results showing good agreement.

Some of the assumptions of the reference model are:

1. Thermo-fluid processes, such as the Marangoni effect and fluid movement in the melt pool are included.
2. Material vaporization is not considered, even though high temperatures can occur. Based on references, the authors claim that vaporization did not have an impact on the temperature distributions.
3. The focus of the reference study was on the effect of packing structure and particle diameter on temperature distributions, neglecting the influence of hatch distance and considering only the average powder diameter when calculating the effective thermal conductivity of the powder phase.

The reference case study consists of the stacking of 5 hatch layers (one on top of the other) composed of 5 tracks each. In Table 8, the study parameters are shown. Two subcases using two different materials (SS316 and Ti6Al4V) are carried out.

Table 8 Material and process parameter for the Mukherjee et al., [30], case scenario.

Material and process parameters	Values
Laser power (W)	60
Beam radius (mm)	0.05
Layer thickness (mm)	0.03
Scan speed (mm/s)	1000
Track length (mm)	20
Material	SS 316, Ti6Al4V
Pack efficiency	0.5

Similar to the previous case study, a structured mesh is used where the level set equation, the Beer-Lambert equation and the energy equation are solved. In the outer domain an unstructured mesh is used and only the energy equation is solved. In Figure 67 the meshed domain is depicted.

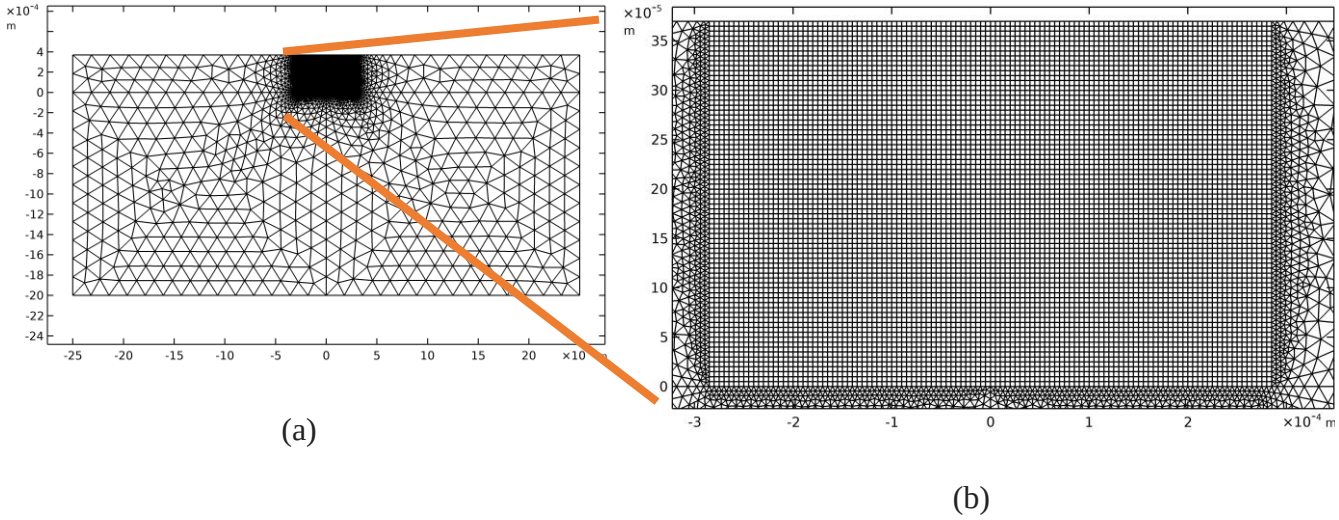

(a)

(b)

Figure 67. Domain mesh. (a) Free mesh with max. element size 1.85 10^{-4} m *and min. element size 5* 10^{-6} m*, (b) regular mesh 5* 10^{-6} m.

The initial conditions are also similar to those implemented in the previous case study except for the initial condition in the ϕ-field, which needs to be adapted to the size of powder layer as well as the transition zone, however, is the same relative size of 2ε. This initial condition is depicted in Figure 68. The system of 3 partial differential equations is solved by an iterative segregated solver.

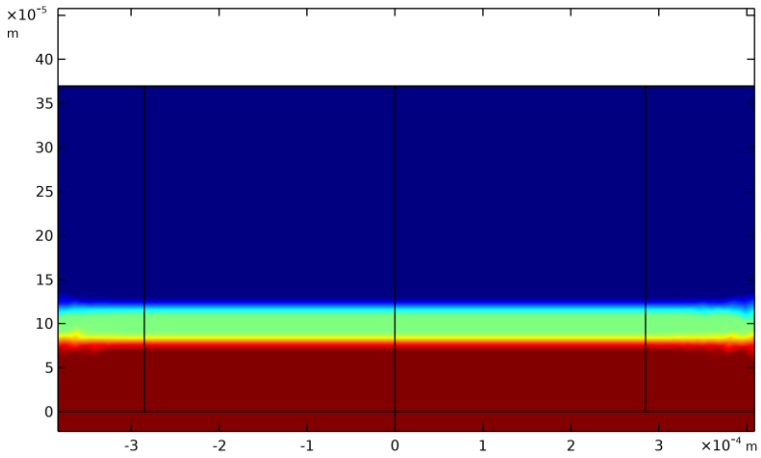

Figure 68. Initial condition for theϕ-field.

5.2.1 Results for SS316

A set of results for the material SS316 is presented and then a comparison with the reference case is addressed. In Figure 69 a sequence of images of the evolution of the scanning is presented. The ϕ-field is depicted for the 5 hatches and 5 tracks. The behavior is very much alike to the Foorozmehr case, however an important difference can be notice in the thickness of the powder layer which is much thinner. In this case study bounding with the substrate exists. In fact, a full bonding of the first layer can be appreciated. However, this occurs only after the second powder layer is applied, and because of the densification of the powder, the thickness of the powder layer on top of the previous tracks increases in comparison with the actual powder layer thickness by a factor related to the homogenized density in the powder region. In this case, $\phi = 0.50$ is used, which means a volumetric reduction of 50% when fully densified. As a result, after the first powder of layer is applied, the following tracks are 50% thicker than the first track. In the same sequence it is possible to visualize zones where no full density is reached. Meaning that lack of fusion is present. It is demonstrated that the method can identify zones where no melting occurs due to an insufficient energy. In Figure 70 the temperature field associated to Figure 69 is presented. Again, a high temperature in the void is observed. In this case a higher temperature is observed in the consolidated material. A different behavior is observed from the tracks that are next to the powder zone from the ones far to the powder. The low conductivity in the powder region enhances penetration in that zone, whereas for the middle tracks heat moves faster to the previous tracks without the powder wall effect, which results in a drainage of energy away from the melt pool.

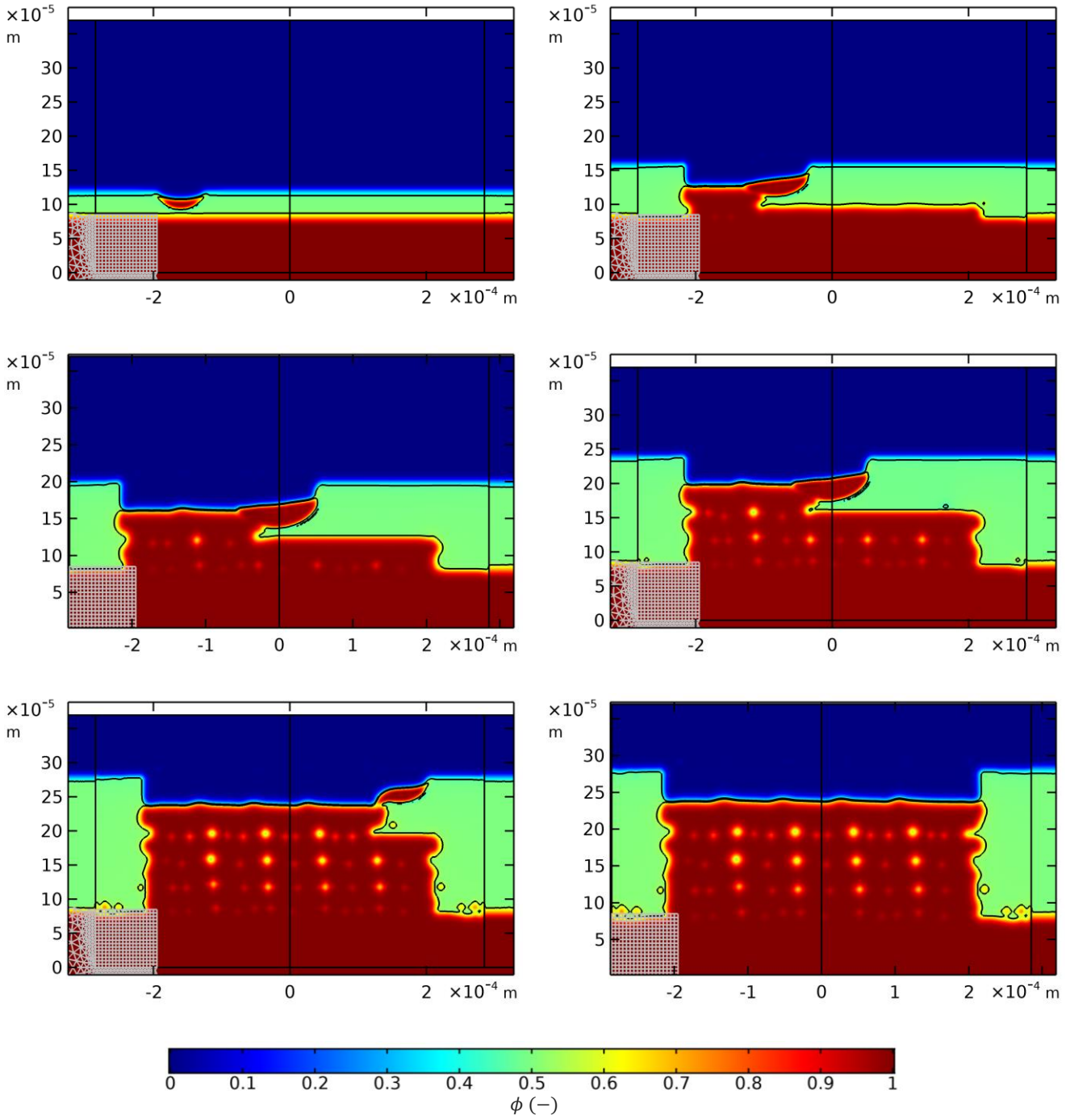

Figure 69. ϕ-field evolution for 5 hatches and 5 tracks.

In Figure 71 a comparison with the reference case is presented, herein the result of applying a solidus temperature filter is applied producing sharp transitions identifying the melted zones. In this image a lack of fusion can be observed and in some parts no bonding with the previous layers takes place. Only the first track shows a good bonding with the substrate, but because of the densification after the first track, the subsequent powder layers become thicker, requiring more energy to fuse the larger amount of raw

material. This lack of bonding can also be appreciated in the reference case. One important difference can be noticed in the shape of the melted zones in both cases. While the melted zone in the reference case is quite uniform, different morphology appears in the results of the proposed model. A uniformity of the melted zone might be a bit unrealistic, however, this is also a consequence of the assumptions in the reference case in which no densification effect is considered, and a uniform layer of powder/consolidated material is implemented, leaving aside the effect of the increase in the powder layers due to the densification.

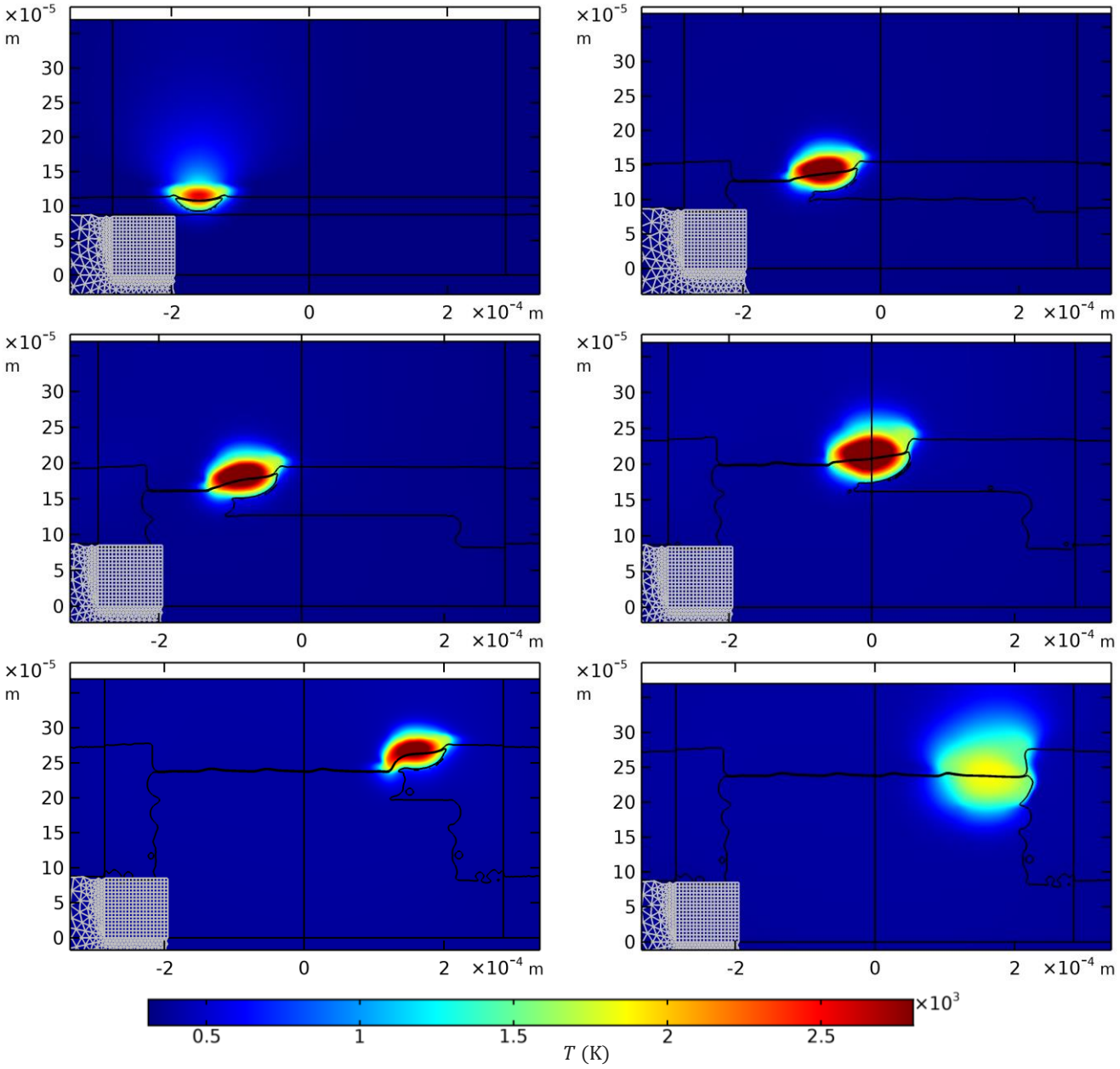

Figure 70. Temperature evolution for the 5 hatches and 5 tracks test.

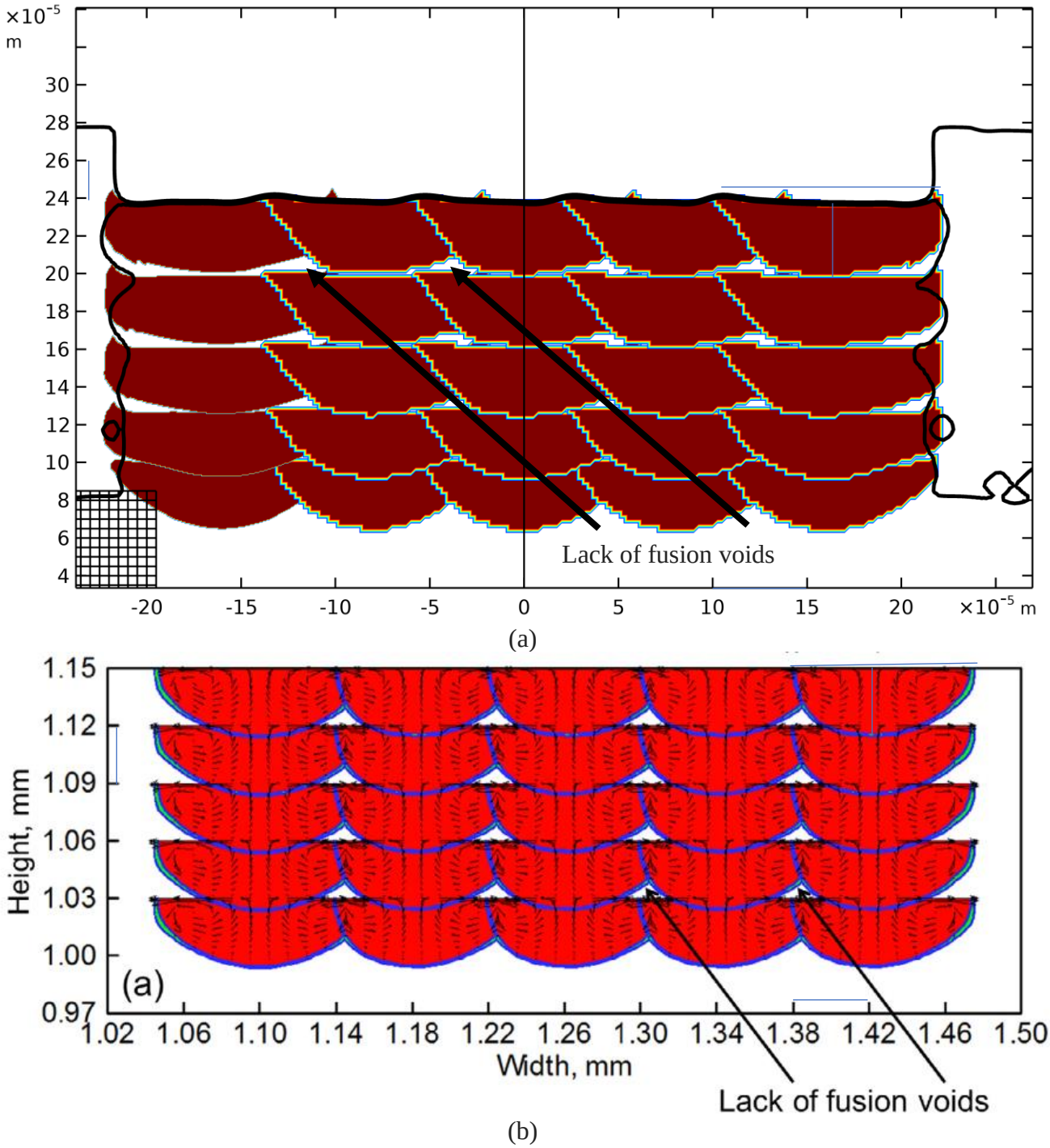

Figure 71. Lack of fusion voids for SS316. Comparison of the cross-section of the melted zone (a) this research and (b) Mukherjee et al. [30].

A comparative table is presented in Table 9 and Table 10. This comparison is made with the melt pool dimensions height and width. Herein a negative error can be noticed, being larger in the width prediction.

Table 9 Comparative table for the heigh of the melted zone. SS316.

SS316	Height (mm)	%ε
Mukherjee et al.	0.04355	-6.67
Torres	0.04645	

Table 10 Comparative table for the width of the melted one. SS316.

SS316	Width (mm)	%ε
Mukherjee et al.	0.11258	-15.92
Torres	0.13050	

5.2.2 Results for Ti6Al4V

A second material, Ti6Al4V, is tested with the same parameters as mentioned previously. In Figure 72a the result of the solidus temperature filter is presented. It is possible to identify a better densification than in the previous case. Similarly to the SS316 the morphology of the tracks changes according to the location. Although a higher penetration is observed in the first layer, the upcoming layers also reach a good densification. This is because of the different material properties of each alloy, especially the density which is almost a half of the SS316, leading to a lower heat capacity, requiring less energy to produce fusion even though the Ti6Al4V has a higher melting point.

The regularity of the melt pool in the reference case Figure 72b is also observed. No difference between the first track and subsequent tracks is noticed, and almost a symmetry with the vertical axis can be appreciated. Opposed to Figure 72a in which several melt pool shapes are found. This can be explained with the convection flow present in the reference case that fades the differences in the conductivity at different locations.

In Table 11 and Table 12 a comparison between the results reported in the reference case and the proposed model is presented. The melt pool dimensions are compared and similar magnitudes of relative errors as obtained for SS316 are obtained. The proposed model overestimates the melt pool dimensions compared to the reference.

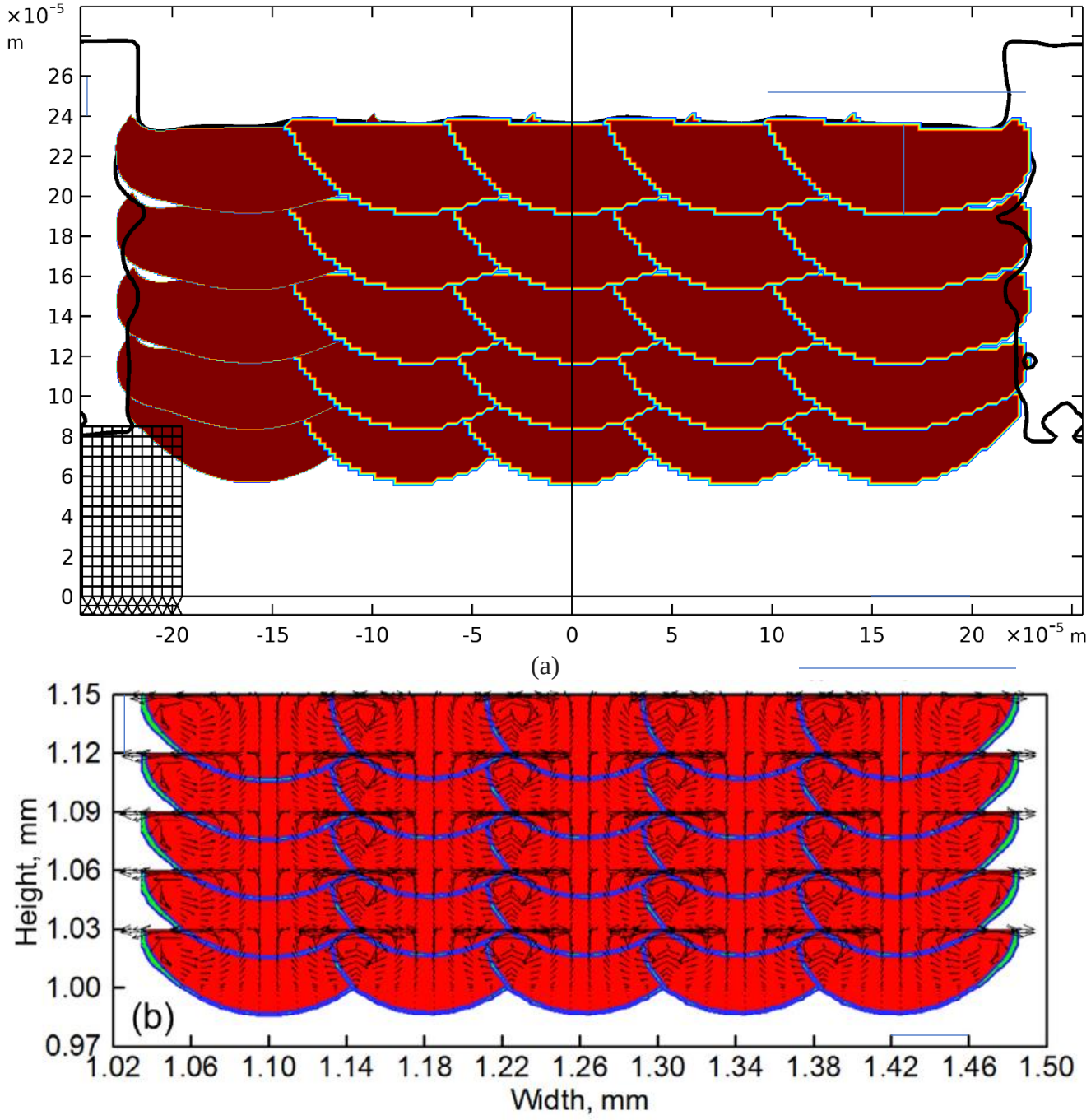

Figure 72. Lack of fusion voids for Ti6Al4V. Comparison of the cross-section of the melted zone (a) this research and (b) Mukherjee et al. [30].

Table 11 Comparative table for the heigh of the melted zone. Ti6Al4V.

Ti6Al4V	Height (mm)	%ε
Mukherjee et al.	0.03548	-5.79
Torres	0.03754	

Table 12 Comparative table for the width of the melted zone. Ti6Al4V.

Ti6Al4V	Width (mm)	%ε
Mukherjee et al.	0.10065	-16.56
Torres	0.11732	

5.2.3 Discussion

Although the size of the melted zone is about the same, the morphologies in the reference and the proposed model deviate. It seems that the convective flow, which is shown to exist of two counter rotating vortices, regularized the shape of the melted material. Since no 'free' flow is included in the proposed model, the shape of the melted zone is considerably more affected by its surroundings producing different morphologies. Nonetheless, a good agreement with the melt pool dimensions is found, having around 16% relative error in both materials. Opposed to expected, this error is negative which means that the predicted melt pool is larger than the reference case, overpredicting the size. This effect also coincides with the Foroozmehr case, in which also overprediction of the dimension was obtained when the velocity is 100 mm/s.

5.3 Discussion

The presented cases showed good agreement when compared with experimental results and more complex models. However, only few cases were tested and more simulations needs to be run in order to identify the limits of the 2-D model. It is worth to mention that all the presented case studies showed no important signs of the keyhole effect. This mode brings with it a melt pool behavior that entraps more heat and what is more, the heat is quickly taken to the bottom of the melt pool passing from a circular to an elliptical shape. If the keyhole effect increases an elliptical shape appear but, in this case, the longer axis is the vertical one. If the keyhole effect increases even more the shape of the melt pool develops into shapes in which the penetration of heat is extremely high. So far, the presented model is not capable of describing such behavior.

All the simulation cases presented in the current chapter were carried out using quadratic Lagrange elements, however, as it was proven in Chapter 3, linear elements showed good performance when having similar DOF. Although the domain in which the level set equation was solved used a structured mesh, the

method has no problem when working with unstructured meshes as it was previously shown in Chapter 3. Therefore, it expected that this model is also suitable for working with adaptive meshes reducing the computational time.

Another important aspect is the computational time. In Table 13 the computational time is presented for each case. To improve the comparison between the two cases, a time per track is calculated and presented. It is possible to verify that the computational time per track is very similar for all the cases, since the number of DOFs is also quite similar. This congruence among the different scales is due to the definition of the beam diameter and the element size which is 10.

Table 13 Computational time per track for the different case studies and element types

		DOF	***Time per track [min]***
Case Foroozmehr	$v_L = 80$ mm/s	121740 quadratic elements	21.2
	$v_L = 100$ mm/s	121740 quadratic elements	20.8
	$v_L = 150$ mm/s	121740 quadratic elements	20.1
Case Mukherjee	SS316L	117701 quadratic elements	18.85
	Ti6Al4V	117701 quadratic elements	19.42

6 Conclusions

In this thesis a new model concept is proposed to deal with the evolving surfaces in AM processes and successfully applied to some PBF cases. This model uses a homogenized density model that allows to deal with powder material as homogeneous mixture of powder and gas or void. Within this framework three materials states can be distinguished: void, powder, and consolidated material. This model is of particular interest, since it can effectively deal with the three different types of free interfaces using one conservative level set equation that ranges from $\phi = 0$ to $\phi = 1$, but recognizes a third stable level at an arbitrary intermediate level between 0 and 1.

6.1 Main conclusions

Some conclusions about the Homogenized Density Level Set model are addressed as follows:

- The presented model reduces to the original CLS when only two stable levels are present.
- The densification and merging are handled naturally.
- The aforementioned coefficients included in the switching function β were tested for a variety of cases showing a suitable performance. Nonetheless, it was found that β is affected by the element type, order of the element, as well as by the initial conditions.
- Even though three stable levels are managed, only one single substance is conserved: the same substance is present as powder and as a fully dense material. Conservation of the surrounding gas or void is ignored.
- This model, just like other level set models, suffers from a rounding-off effect at the edges.
- The rounding-off effect depends on the element size. This imposes a limitation to the melt pool radius and the element size. The presented case studies showed that around 10 elements for the melt pool diameter produced suitable results.

Some conclusions about the mass conservation equation:

- There is a direct relation between level set equation and the mass conservation equation, characteristic that guarantees the mass conservation implicitly through the conservative formulation of the level set equation.

- Within this framework, the level set variable ϕ is directly interpreted as a relative density function or phase fraction.
- It was proven that mass is preserved under this formulation.
- The experimental effect of powder densification is naturally managed by this model.
- Mass conservation is only guaranteed for the powder and consolidated material. The conservation of the void is not guaranteed. However, in this work, there is no sense in the conservation of void, since the void phase is only added as a way to make room for adding extra material and for representing a void when powder is consolidated.

Some conclusions about the energy conservation equation:

- A full energy conservation equation was derived to work within this homogenized density model that includes the incorporation of the boundary conditions at the interface in the form of a volumetric heat source, which was proven to work correctly.
- The apparent enthalpy model guarantees the energy conservation, opposed to temperature models in which energy conservation is not guaranteed in case of strong coefficient variations, in particular, the spike in the apparent C_p value related to the latent heat of fusion.
- The Beer-Lambert heat source model is capable to work along with evolving interfaces. The characteristic to naturally determine the interface makes this heat source model an excellent approach when the interface position is not known a priori, although it requires the solution of an additional equation.
- The increase in the solidus to liquidus transition range lead to smoother and faster solution process while maintaining the accuracy.

Some conclusions about the case studies:

- Even though the model is reduced to a 2-D analysis, a good correlation was found with experimental models as well with more detailed computational models.
- The net heat transfer by the convection mechanism in the melt pool, which is determined by the proposed temperature dependent velocity field, is shown to be sufficient to predict the melt pool dimensions in most of the cases. However, the error increased as the melt pool increased. That demonstrates that the size of the melt pool might be a limit of this model, especially for the cases in which a keyhole is formed.

- Although only results of 2-D models are presented, the model is described in a general way, and it can be implemented similarly in 3-D, observing that such a 3-D model would require significantly more computation resources.

6.2 General conclusions

- A Homogenized Density Model to track evolving interfaces was derived in this thesis. The model was developed for a general transient 3-D case. Chapters 3 and 4.
- A 2-D reduced order model based on the 3-D model was developed and tested with experimental and computational results in Chapter 5. This reduced order model showed good agreement with the experiments and also with more complex computational models. Nonetheless, the 2-D case is limited to the number of scanning patterns that can be used in the 3-D case.
- The main advantage of Homogenized Density model is its capability to keep track of three different interfaces avoiding the need of using 2 or 3 standard LS equations. Its use can help to lower the number of DOF during the simulation when having more than two components.
- Although structured meshes were used, the model can perfectly work on irregular meshes. However, as it is derived in this work, the transition zone depends on the element size, therefore, if the element grows, the transition size also grows, If a constant transition is set instead, the number of elements across the transition might not be enough to correctly represent the transition and convergency problems might appear. Therefore, care is recommended if a constant transition is set over an irregular mesh.

6.3 Future work

The obtained results of the proposed model is a step into the direction of a more complete multiphysics model of additive manufacturing processes, which can assist in the development and the implementation of improvements of these processes. Some research lines that can be addressed in future work are identified in the next paragraphs:

- Although the model was developed for 3-D only 2-D results have been tested. However, it is expected that the 3-D results may improve the agreement with reported cases in literature, since currently the fluxes in the longitudinal track direction are ignored, which is known to have some influence in the results in comparison with the 2-D model results.

- Alternative scanning strategies and heating patterns can be tested to produce different hatches in order identify improved scanning techniques.
- So far, only thermal aspects have been considered. However, an important interest in the prediction of the temperature fields, is by its usage as input for a mechanical analysis and a microstructural analysis which incorporates the prediction of the non-equilibrium solid state transformations. This would allow the prediction of the residual stresses and deformations, and the microstructures in the components.

References

[1] E. L. Papazoglou, N. E. Karkalos, and A. P. Markopoulos, “A comprehensive study on thermal modeling of SLM process under conduction mode using FEM,” *Int. J. Adv. Manuf. Technol.*, vol. 111, no. 9–10, pp. 2939–2955, Dec. 2020, doi: 10.1007/s00170-020-06294-7.

[2] G. Kasperovich and J. Hausmann, “Improvement of fatigue resistance and ductility of TiAl6V4 processed by selective laser melting,” *J. Mater. Process. Technol.*, vol. 220, pp. 202–214, Jun. 2015, doi: 10.1016/j.jmatprotec.2015.01.025.

[3] T. DebRoy *et al.*, “Additive manufacturing of metallic components – Process, structure and properties,” *Prog. Mater. Sci.*, vol. 92, pp. 112–224, Mar. 2018, doi: 10.1016/j.pmatsci.2017.10.001.

[4] M. Taghizadeh and Z. H. Zhu, “A comprehensive review on metal laser additive manufacturing in space: Modeling and perspectives,” *Acta Astronaut.*, vol. 222, pp. 403–421, Sep. 2024, doi: 10.1016/j.actaastro.2024.06.027.

[5] Y. Mao, H. Chen, and J. Xiong, “Research progress in laser additive manufacturing of aluminum alloys: Microstructure, defect, and properties,” *J. Mater. Res. Technol.*, vol. 30, pp. 695–716, May 2024, doi: 10.1016/j.jmrt.2024.03.099.

[6] B. Soundararajan, D. Sofia, D. Barletta, and M. Poletto, “Review on modeling techniques for powder bed fusion processes based on physical principles,” *Addit. Manuf.*, vol. 47, p. 102336, Nov. 2021, doi: 10.1016/j.addma.2021.102336.

[7] P. C. Collins, D. A. Brice, P. Samimi, I. Ghamarian, and H. L. Fraser, “Microstructural Control of Additively Manufactured Metallic Materials,” *Annu. Rev. Mater. Res.*, vol. 46, no. 1, pp. 63–91, Jul. 2016, doi: 10.1146/annurev-matsci-070115-031816.

[8] W. Yan *et al.*, “Multi-physics modeling of single/multiple-track defect mechanisms in electron beam selective melting,” *Acta Mater.*, vol. 134, pp. 324–333, Aug. 2017, doi: 10.1016/j.actamat.2017.05.061.

[9] E. Olsson and G. Kreiss, “A conservative level set method for two phase flow,” *J. Comput. Phys.*, vol. 210, no. 1, pp. 225–246, Nov. 2005, doi: 10.1016/j.jcp.2005.04.007.

[10] E. Vaglio, G. Totis, A. Lanzutti, L. Fedrizzi, and M. Sortino, “A novel thermo-geometrical model for accurate keyhole porosity prediction in Laser Powder-Bed Fusion,” *Prog. Addit. Manuf.*, vol. 9, no. 2, pp. 247–261, Apr. 2024, doi: 10.1007/s40964-023-00446-3.

[11] L. Wang, Y. Zhang, and W. Yan, “Evaporation Model for Keyhole Dynamics During Additive Manufacturing of Metal,” *Phys. Rev. Appl.*, vol. 14, no. 6, p. 064039, Dec. 2020, doi: 10.1103/PhysRevApplied.14.064039.

[12] S. M. H. Hojjatzadeh *et al.*, “Direct observation of pore formation mechanisms during LPBF additive manufacturing process and high energy density laser welding,” *Int. J. Mach. Tools Manuf.*, vol. 153, p. 103555, Jun. 2020, doi: 10.1016/j.ijmachtools.2020.103555.

[13] E. Soylemez, “Modeling the Melt Pool of the Laser Sintered Ti6Al4V Layers with Goldak’s Double-Ellipsoidal Heat Source,” University of Texas at Austin, 2018.

[14] T. Mukherjee, J. S. Zuback, A. De, and T. DebRoy, “Printability of alloys for additive manufacturing,” *Sci. Rep.*, vol. 6, no. 1, p. 19717, Jan. 2016, doi: 10.1038/srep19717.

[15] B. E. Carroll, T. A. Palmer, and A. M. Beese, “Anisotropic tensile behavior of Ti–6Al–4V components fabricated with directed energy deposition additive manufacturing,” *Acta Mater.*, vol. 87, pp. 309–320, Apr. 2015, doi: 10.1016/j.actamat.2014.12.054.

[16] L.-E. Lindgren, A. Lundbäck, M. Fisk, R. Pederson, and J. Andersson, “Simulation of additive manufacturing using coupled constitutive and microstructure models,” *Addit. Manuf.*, vol. 12, pp. 144–158, Oct. 2016, doi: 10.1016/j.addma.2016.05.005.

[17] H. Zhao, H. Zhang, C. Xu, and X. Yang, “Temperature and stress fields of multi-track laser cladding,” *Trans. Nonferrous Met. Soc. China*, vol. 19, pp. s495–s501, Sep. 2009, doi: 10.1016/S1003-6326(10)60096-9.

[18] M. Markl and C. Körner, “Multiscale Modeling of Powder Bed–Based Additive Manufacturing,” *Annu. Rev. Mater. Res.*, vol. 46, no. 1, pp. 93–123, Jul. 2016, doi: 10.1146/annurev-matsci-070115-032158.

[19] N. D. Dejene, H. G. Lemu, and E. M. Gutema, “Effects of process parameters on the surface characteristics of laser powder bed fusion printed parts: machine learning predictions with random forest and support vector regression,” *Int. J. Adv. Manuf. Technol.*, Jul. 2024, doi: 10.1007/s00170-024-14087-5.

[20] S. Srinivasan, B. Swick, and M. A. Groeber, “Laser Powder Bed Fusion Parameter Selection via Machine-Learning-Augmented Process Modeling,” *JOM*, vol. 72, no. 12, pp. 4393–4403, Dec. 2020, doi: 10.1007/s11837-020-04383-2.

[21] Y. Cao and J. Choi, “Multiscale modeling of solidification during laser cladding process,” *J. Laser Appl.*, vol. 18, no. 3, pp. 245–257, Aug. 2006, doi: 10.2351/1.2227021.

[22] Y. T. Gu and L. C. Zhang, “A Concurrent Multiscale Method Based on the Meshfree Method and Molecular Dynamics Analysis,” *Multiscale Model. Simul.*, vol. 5, no. 4, pp. 1128–1155, Jan. 2006, doi: 10.1137/060654232.

[23] C. Meier, R. W. Penny, Y. Zou, J. S. Gibbs, and A. J. Hart, “Thermophysical Phenomena In Metal Additive Manufacturing By Selective Laser Melting: Fundamentals, Modeling, Simulation, And Experimentation,” *Annu. Rev. Heat Transf.*, vol. 20, no. 1, pp. 241–316, 2017, doi: 10.1615/AnnualRevHeatTransfer.2018019042.

[24] D. Bishara, Y. Xie, W. K. Liu, and S. Li, “A State-of-the-Art Review on Machine Learning-Based Multiscale Modeling, Simulation, Homogenization and Design of Materials,” *Arch. Comput. Methods Eng.*, vol. 30, no. 1, pp. 191–222, Jan. 2023, doi: 10.1007/s11831-022-09795-8.

[25] E. L. Papazoglou, N. E. Karkalos, P. Karmiris-Obratański, and A. P. Markopoulos, “On the Modeling and Simulation of SLM and SLS for Metal and Polymer Powders: A Review,” *Arch. Comput. Methods Eng.*, vol. 29, no. 2, pp. 941–973, Mar. 2022, doi: 10.1007/s11831-021-09601-x.

[26] A. Razavykia, E. Brusa, C. Delprete, and R. Yavari, “An Overview of Additive Manufacturing Technologies—A Review to Technical Synthesis in Numerical Study of Selective Laser Melting,” *Materials*, vol. 13, no. 17, p. 3895, Sep. 2020, doi: 10.3390/ma13173895.

[27] S. Afazov *et al.*, “Metal powder bed fusion process chains: an overview of modelling techniques,” *Prog. Addit. Manuf.*, vol. 7, no. 2, pp. 289–314, Apr. 2022, doi: 10.1007/s40964-021-00230-1.

[28] S. Chowdhury *et al.*, “Laser powder bed fusion: a state-of-the-art review of the technology, materials, properties & defects, and numerical modelling,” *J. Mater. Res. Technol.*, vol. 20, pp. 2109–2172, Sep. 2022, doi: 10.1016/j.jmrt.2022.07.121.

[29] T. Mukherjee, H. L. Wei, A. De, and T. DebRoy, “Heat and fluid flow in additive manufacturing—Part I: Modeling of powder bed fusion,” *Comput. Mater. Sci.*, vol. 150, pp. 304–313, Jul. 2018, doi: 10.1016/j.commatsci.2018.04.022.

[30] T. Mukherjee, H. L. Wei, A. De, and T. DebRoy, “Heat and fluid flow in additive manufacturing – Part II: Powder bed fusion of stainless steel, and titanium, nickel and aluminum base alloys,” *Comput. Mater. Sci.*, vol. 150, pp. 369–380, Jul. 2018, doi: 10.1016/j.commatsci.2018.04.027.

[31] D. Singh, H. A. Friis, E. Jettestuen, and J. O. Helland, “Adaptive mesh refinement in locally conservative level set methods for multiphase fluid displacements in porous media,” *Comput. Geosci.*, vol. 27, no. 5, pp. 707–736, Oct. 2023, doi: 10.1007/s10596-023-10219-0.

[32] M. McMillan, M. Leary, and M. Brandt, “Computationally efficient finite difference method for metal additive manufacturing: A reduced-order DFAM tool applied to SLM,” *Mater. Des.*, vol. 132, pp. 226–243, Oct. 2017, doi: 10.1016/j.matdes.2017.06.058.

[33] A. Torres Cruz, D. F. De Lange, and H. I. Medellín Castillo, “Comparative study of numerical models of the laser forming process,” *J. Laser Appl.*, vol. 27, no. S2, p. S29105, Feb. 2015, doi: 10.2351/1.4907397.

[34] E. T. Chung, Y. Efendiev, T. Leung, and M. Vasilyeva, “Coupling of multiscale and multi-continuum approaches,” *GEM - Int. J. Geomath.*, vol. 8, no. 1, pp. 9–41, Apr. 2017, doi: 10.1007/s13137-017-0093-8.

[35] R. Darabi, E. Azinpour, A. Reis, and J. C. De Sa, “Multi-scale Multi-physics Phase-field coupled Thermo-mechanical approach for modeling of powder bed fusion process,” *Appl. Math. Model.*, vol. 122, pp. 572–597, Oct. 2023, doi: 10.1016/j.apm.2023.06.021.

[36] W. Yan *et al.*, “Modeling process-structure-property relationships for additive manufacturing,” *Front. Mech. Eng.*, vol. 13, no. 4, pp. 482–492, Dec. 2018, doi: 10.1007/s11465-018-0505-y.

[37] M. M. Francois *et al.*, “Modeling of additive manufacturing processes for metals: Challenges and opportunities,” *Curr. Opin. Solid State Mater. Sci.*, vol. 21, no. 4, pp. 198–206, Aug. 2017, doi: 10.1016/j.cossms.2016.12.001.

[38] W. Shyy, *Computational Fluid Dynamics With Moving Boundaries*. CRC Press, 1995.

[39] S. Osher and R. P. Fedkiw, “Level Set Methods: An Overview and Some Recent Results,” *J. Comput. Phys.*, vol. 169, no. 2, pp. 463–502, May 2001, doi: 10.1006/jcph.2000.6636.

[40] S. Osher and J. A. Sethian, “Fronts propagating with curvature-dependent speed: Algorithms based on Hamilton-Jacobi formulations,” *J. Comput. Phys.*, vol. 79, no. 1, pp. 12–49, Nov. 1988, doi: 10.1016/0021-9991(88)90002-2.

[41] M. Sussman, P. Smereka, and S. Osher, “A Level Set Approach for Computing Solutions to Incompressible Two-Phase Flow,” *J. Comput. Phys.*, vol. 114, no. 1, pp. 146–159, Sep. 1994, doi: 10.1006/jcph.1994.1155.

[42] E. Olsson, G. Kreiss, and S. Zahedi, “A conservative level set method for two phase flow II,” *J. Comput. Phys.*, vol. 225, no. 1, pp. 785–807, Jul. 2007, doi: 10.1016/j.jcp.2006.12.027.

[43] R. K. Shukla, C. Pantano, and J. B. Freund, “An interface capturing method for the simulation of multi-phase compressible flows,” *J. Comput. Phys.*, vol. 229, no. 19, pp. 7411–7439, Sep. 2010, doi: 10.1016/j.jcp.2010.06.025.

[44] N. Shervani-Tabar and O. V. Vasilyev, “Stabilized conservative level set method,” *J. Comput. Phys.*, vol. 375, pp. 1033–1044, Dec. 2018, doi: 10.1016/j.jcp.2018.09.020.

[45] O. Desjardins, V. Moureau, and H. Pitsch, “An accurate conservative level set/ghost fluid method for simulating turbulent atomization,” *J. Comput. Phys.*, vol. 227, no. 18, pp. 8395–8416, Sep. 2008, doi: 10.1016/j.jcp.2008.05.027.

[46] L. Zhao, X. Bai, T. Li, and J. J. R. Williams, “Improved conservative level set method,” *Int. J. Numer. Methods Fluids*, vol. 75, no. 8, pp. 575–590, Jul. 2014, doi: 10.1002/fld.3907.

[47] R. Chiodi and O. Desjardins, “A reformulation of the conservative level set reinitialization equation for accurate and robust simulation of complex multiphase flows,” *J. Comput. Phys.*, vol. 343, pp. 186–200, Aug. 2017, doi: 10.1016/j.jcp.2017.04.053.

[48] J.-C. Nave, R. R. Rosales, and B. Seibold, “A gradient-augmented level set method with an optimally local, coherent advection scheme,” *J. Comput. Phys.*, vol. 229, no. 10, pp. 3802–3827, May 2010, doi: 10.1016/j.jcp.2010.01.029.

[49] L. Ville, L. Silva, and T. Coupez, “Convected level set method for the numerical simulation of fluid buckling,” *Int. J. Numer. Methods Fluids*, vol. 66, no. 3, pp. 324–344, May 2011, doi: 10.1002/fld.2259.

[50] J.-L. Guermond, M. Q. De Luna, and T. Thompson, “An conservative anti-diffusion technique for the level set method,” *J. Comput. Appl. Math.*, vol. 321, pp. 448–468, Sep. 2017, doi: 10.1016/j.cam.2017.02.016.

[51] M. Quezada De Luna, D. Kuzmin, and C. E. Kees, “A monolithic conservative level set method with built-in redistancing,” *J. Comput. Phys.*, vol. 379, pp. 262–278, Feb. 2019, doi: 10.1016/j.jcp.2018.11.044.

[52] Y. Sun and C. Beckermann, “Sharp interface tracking using the phase-field equation,” *J. Comput. Phys.*, vol. 220, no. 2, pp. 626–653, Jan. 2007, doi: 10.1016/j.jcp.2006.05.025.

[53] P.-H. Chiu and Y.-T. Lin, “A conservative phase field method for solving incompressible two-phase flows,” *J. Comput. Phys.*, vol. 230, no. 1, pp. 185–204, Jan. 2011, doi: 10.1016/j.jcp.2010.09.021.

[54] H. A. Akhlaghi Amiri and A. A. Hamouda, “Evaluation of level set and phase field methods in modeling two phase flow with viscosity contrast through dual-permeability porous medium,” *Int. J. Multiph. Flow*, vol. 52, pp. 22–34, Jun. 2013, doi: 10.1016/j.ijmultiphaseflow.2012.12.006.

[55] H. Hua, J. Shin, and J. Kim, “Level Set, Phase-Field, and Immersed Boundary Methods for Two-Phase Fluid Flows,” *J. Fluids Eng.*, vol. 136, no. 2, p. 021301, Feb. 2014, doi: 10.1115/1.4025658.

[56] T. Wacławczyk, “On a relation between the volume of fluid, level-set and phase field interface models,” *Int. J. Multiph. Flow*, vol. 97, pp. 60–77, Dec. 2017, doi: 10.1016/j.ijmultiphaseflow.2017.08.003.

[57] B. Merriman, J. K. Bence, and S. J. Osher, “Motion of Multiple Junctions: A Level Set Approach,” *J. Comput. Phys.*, vol. 112, no. 2, pp. 334–363, Jun. 1994, doi: 10.1006/jcph.1994.1105.

[58] H.-K. Zhao, T. Chan, B. Merriman, and S. Osher, “A Variational Level Set Approach to Multiphase Motion,” *J. Comput. Phys.*, vol. 127, no. 1, pp. 179–195, Aug. 1996, doi: 10.1006/jcph.1996.0167.

[59] S. J. Ruuth, “A Diffusion-Generated Approach to Multiphase Motion,” *J. Comput. Phys.*, vol. 145, no. 1, pp. 166–192, Sep. 1998, doi: 10.1006/jcph.1998.6028.

[60] H. Hallberg, “A modified level set approach to 2D modeling of dynamic recrystallization,” *Model. Simul. Mater. Sci. Eng.*, vol. 21, no. 8, p. 085012, Dec. 2013, doi: 10.1088/0965-0393/21/8/085012.

[61] J. Mao, L. Zhao, X. Liu, J. Cheng, and E. Avital, “A three-phases model for the simulation of landslide-generated waves using the improved conservative level set method,” *Comput. Fluids*, vol. 159, pp. 243–253, Dec. 2017, doi: 10.1016/j.compfluid.2017.10.007.

[62] M. H. Farshidianfar, A. Khajepour, and A. P. Gerlich, “Effect of real-time cooling rate on microstructure in Laser Additive Manufacturing,” *J. Mater. Process. Technol.*, vol. 231, pp. 468–478, May 2016, doi: 10.1016/j.jmatprotec.2016.01.017.

[63] T. Mukherjee, W. Zhang, and T. DebRoy, “An improved prediction of residual stresses and distortion in additive manufacturing,” *Comput. Mater. Sci.*, vol. 126, pp. 360–372, Jan. 2017, doi: 10.1016/j.commatsci.2016.10.003.

[64] A. A. Amin *et al.*, “Physics guided heat source for quantitative prediction of IN718 laser additive manufacturing processes,” *Npj Comput. Mater.*, vol. 10, no. 1, p. 37, Feb. 2024, doi: 10.1038/s41524-024-01198-6.

[65] S. Morville *et al.*, “2D longitudinal modeling of heat transfer and fluid flow during multilayered direct laser metal deposition process,” *J. Laser Appl.*, vol. 24, no. 3, p. 032008, Aug. 2012, doi: 10.2351/1.4726445.

[66] A. Foroozmehr, M. Badrossamay, E. Foroozmehr, and S. Golabi, “Finite Element Simulation of Selective Laser Melting process considering Optical Penetration Depth of laser in powder bed,” *Mater. Des.*, vol. 89, pp. 255–263, Jan. 2016, doi: 10.1016/j.matdes.2015.10.002.

[67] W. Yan, J. Smith, W. Ge, F. Lin, and W. K. Liu, “Multiscale modeling of electron beam and substrate interaction: a new heat source model,” *Comput. Mech.*, vol. 56, no. 2, pp. 265–276, Aug. 2015, doi: 10.1007/s00466-015-1170-1.

[68] A. K. Mishra, A. Aggarwal, A. Kumar, and N. Sinha, “Identification of a suitable volumetric heat source for modelling of selective laser melting of Ti6Al4V powder using numerical and experimental validation approach,” *Int. J. Adv. Manuf. Technol.*, vol. 99, no. 9–12, pp. 2257–2270, Dec. 2018, doi: 10.1007/s00170-018-2631-4.

[69] J. Goldak, A. Chakravarti, and M. Bibby, “A new finite element model for welding heat sources,” *Metall. Trans. B*, vol. 15, no. 2, pp. 299–305, Jun. 1984, doi: 10.1007/BF02667333.

[70] C. Bruna-Rosso, A. G. Demir, and B. Previtali, “Selective laser melting finite element modeling: Validation with high-speed imaging and lack of fusion defects prediction,” *Mater. Des.*, vol. 156, pp. 143–153, Oct. 2018, doi: 10.1016/j.matdes.2018.06.037.

[71] D. A. De Moraes and A. Czekanski, “Parametric Thermal FE Analysis on the Laser Power Input and Powder Effective Thermal Conductivity during Selective Laser Melting of SS304L,” *J. Manuf. Mater. Process.*, vol. 2, no. 3, p. 47, Jul. 2018, doi: 10.3390/jmmp2030047.

[72] N. Wakao and S. Kagei, *Heat and Mass Transfer in Packed Beds*. Taylor & Francis, 1982.

[73] S. Sumin Sih and J. W. Barlow, “The Prediction of the Emissivity and Thermal Conductivity of Powder Beds,” *Part. Sci. Technol.*, vol. 22, no. 3, pp. 291–304, Jul. 2004, doi: 10.1080/02726350490501682a.

[74] A. V. Gusarov and I. Smurov, “Modeling the interaction of laser radiation with powder bed at selective laser melting,” *Phys. Procedia*, vol. 5, pp. 381–394, 2010, doi: 10.1016/j.phpro.2010.08.065.

[75] A. Torres Cruz, D. F. De Lange, and W. Van Paepegem, “Efficient single variable Level Set method for capturing moving interfaces in powder densification processes,” *Comput. Methods Appl. Mech. Eng.*, vol. 428, p. 117086, Aug. 2024, doi: 10.1016/j.cma.2024.117086.

[76] S. T. Zalesak, “Fully multidimensional flux-corrected transport algorithms for fluids,” *J. Comput. Phys.*, vol. 31, no. 3, pp. 335–362, Jun. 1979, doi: 10.1016/0021-9991(79)90051-2.